From the holdings of the Department of Special Collections , Princeton University Library, Princeton, NJ

These documents are either in the public domain, or can only be used for educational and research purposes (Fair use) as per U.S. Copyright law (text below). By accessing this file, all users agree that their use falls in the public domain or within fair use as defined by the copyrightlaw. We do not charge any permission or usage fees for the publication of images of material inour collections, including those provided by Princeton University Library, via our website, catalog, or directly from staff.For more information regarding copyright, credit, and citation please review the information onthe Copyright, Credit and Citation Guidelines page of our website.
https://library.princeton.edu/special-collections/policies/copyright-credit-and-citation-guidelines. If you have any questions, including how to order higher-quality images from the collection, contact Special Collections Public Services via our Ask Us! Form. https://library.princeton.edu/special-collections/ask-us

---

Doctoral Dissertations, 2011-2026 Astrophysical Sciences

2025

Cosmic Ray Electrons in the Multiphase Interstellar Medium

Linzer, Nora

Princeton, NJ : Princeton University

---

http://arks.princeton.edu/ark:/88435/dsp01j9602410z

U.S. Copyright law: The copyright law of the United States (Title 17, §108, United States Code) governs the making of photocopies or other reproductions of copyrighted material. Under certain conditions specified in the law, libraries and archives are authorized to furnish a photocopy or other reproduction. One of these specified conditions is that the photocopy or reproduction is not to be used for any purpose other than private study, scholarship, or research. If a user makes a request for, or later uses, a photocopy or reproduction for purposes in excess of fair use that user may be liable for copyright infringement. This institution reserves the right to refuse to accept a copying order if, in its judgment, fulfillment of the order would involve a violation of copyright law. https://www.copyright.gov/title17/title17.pdf

Cosmic Ray Electrons in the Multiphase Interstellar Medium

Nora B. Linzer

A Dissertation
Presented to the Faculty
of Princeton University
in Candidacy for the Degree
of Doctor of Philosophy

Recommended for Acceptance
by the Department of
Astrophysical Sciences
Advisers: Eve C. Ostriker and Eliot Quataert

September 2025

© Copyright by Nora B. Linzer, 2025.

All rights reserved.

Abstract

Cosmic rays (CRs) make up a significant pressure component of the interstellar medium (ISM), on the order of the thermal, turbulent, and magnetic pressures. Therefore, these particles can substantially impact galactic dynamics. Direct observations show that protons make up the majority of the CR population and that there are significantly fewer CR electrons (CREs), so the physical impact of CREs is negligible. Beyond the solar neighborhood, however, CRs cannot be directly measured, and we must rely on indirect probes, primarily radio synchrotron emission produced by the interaction of CREs with local magnetic fields. It is therefore of great importance to understand the evolution of CREs in realistic simulations of the ISM to interpret indirect measurements of the CR population.

In this work, we present a scheme for modeling the transport and spectral evolution of CREs in the magnetized, multiphase ISM which we use to post-process TIGRESS simulations of multiple galactic environments. In Chapter 2, we lay out our two-moment transport method which includes advection, streaming, and diffusion, as well as various energetic loss mechanisms. We post-process TIGRESS models representative of solar neighborhood conditions and find the simulated CRE spectrum to be consistent with direct observations. In Chapter 3, we produce synthetic synchrotron emission which we use to test common observational methods including the extraction of the CRE spectrum from radio observations, as well as the estimation of magnetic field strength through the equipartition assumption. In Chapter 4, we apply our CR modeling scheme to TIGRESS simulations representative of inner galaxy conditions to understand how CRE transport may differ as a function of environment. Finally, we present opportunities for future analysis in Chapter 5.

Acknowledgements

This thesis represents much more than the past three years of work or even the five years I spent at Princeton. It is the culmination of the support I have received from the advisers, teachers, friends, and family I have been so lucky to have in my life. Here I get the chance to thank them.

First, a thank you to my thesis advisers, Eve Ostriker and Eliot Quataert. Eve has been an incredible mentor to me, and I truly appreciate the amount of time and detailed thought she put into every aspect of our work together. I have learned so much through her drive to understand our results at a deeper level. Eliot not only advised my thesis work and a semester project but also gave me the topic of my undergraduate thesis when he visited Caltech. I am so grateful for his focus on the big picture, and his ability to get to the core of any problem quickly.

This work would not have been possible without Lucia Armillotta. Lucia has been there every step of the way to answer my questions and give advice, whether I was trying to figure out the basics of cosmic ray physics, debugging code, or looking for the best restaurants in Florence. I am extremely fortunate to have worked with her on this dissertation.

I would like to thank Anatoly Spitkovsky and Alex Amon for joining my committee and reading my thesis. Their insightful questions improved this work. Additionally, a thank you to Bruce Draine and Jo Dunkley who provided great feedback on this project.

Along with Eve, Jeong-Gyu Kim and Chang-Goo Kim were fantastic advisers for my final rotation. I am thankful for their support through late-night, worldwide zoom calls and their responses to my frequent slack messages over the course of the semester-turned-three-year project.

A big thank you to Jenny Greene and Andy Goulding for advising me on my first semester project, and my one and only foray into observational astrophysics. This was my first experience in grad school in the fall of 2020, and both Jenny and Andy were incredibly supportive despite the complicated circumstances of the pandemic. They went above and

beyond by meeting outside (while masked and socially distanced) to work through the varied obstacles on this project, from fixing a reduction pipeline to saving my life from a laptop battery that was about to explode.

This department would not run without the amazing work of all of the staff. I would like to thank Susan Duncan, Greg Motta, Stephanie Reif, Jillian Hoffman, Mindy Lipman, and Mami Akiyama for their support of the graduate students. My time in the department would not have been the same without Polly Strauss. I am so thankful for her joyful presence and her steadfast encouragement.

Before arriving at Princeton, I was lucky to have the opportunity to work with advisers who taught me so much about how to be a scientist. I would like to thank Jim Fuller, Charles Steinhardt, Kate Scholberg, Tim Eifler, Claude-André Faucher-Giguère, John Marko, and Rebecca Giuntoli for their mentorship throughout my varied research experiences. Their influence helped me succeed here at Princeton.

Looking back, I could have followed many different paths ending up in totally different fields. There are two people who put me firmly on the road to astrophysics, and for that I am incredibly grateful. My high school physics teacher, Mark Vondracek, is the best teacher I have had in my 20+ years of classes. He inspired my love of physics and made it an easy choice of what to study in college. Vicky Kalogera has always been a mentor to me. Although I didn't realize it at the time, she steered me towards astrophysics, and I will always be grateful for her support and encouragement.

My time in this department would not have been the same without my fellow graduate students. Although there are a million reasons to be thankful for every one of them, from the many laughs in the grad lounge to the advice when work was tough, there are a few things that I will always treasure. I am thankful to Amy for sharing a love of Northwestern basketball. Camryn for leading Shaunak, Ronan, Charlotte, Sarah, and me through a DnD adventure. Abby and Lena for always being ready for lunch. Philippe for always being ready to talk about F1. Jared and Jake for much-needed vent sessions. And last but certainly not

least, I am so thankful for the Ro's: Rob, Rodrigo, and Roohi. I am grateful to Rob for his friendship and for sharing this journey over the past five years. Rodrigo has always been there when I needed it, giving support in the form of croissants or conversation. I have been following Roohi, through her advice and in physical location, since we met at Caltech, and I am grateful for her presence as a mentor, an officemate, a roommate, and a lifelong friend.

Thank you to my Princeton roommates, Adri, Gillian, and Ilana, for the late-night chats, trips to Trader Joe's, and delicious results of stress baking. Handing out thousands of pieces of candy on Halloween together will be one of my favorite memories of Princeton. Despite being quarantined in our individual grad college rooms, Katy, Christina, and I were somehow able to connect. I am thankful for their friendship over the past five years, and that they are always ready to play Catan.

To the friends I made at Caltech, I would not have made it here without you. Thank you to Miranda, Kaylor, Sophia, Maria, Adri, Erik, Kenny, Dennis, and Bethany for all the great times together, whether it was spent yelling at whiteboards, going out for Thai food, or getting way too into Risk. Maggie, I am so grateful for being your "randomly" assigned roommate on day one at Caltech, and your unwavering friendship since then. I hope our crossword streak continues for a long, long time.

Thank you to my family (in the broadest definition of that term) who have always been there for me from our travels together to drum circles at Thanksgiving. In my time here at Princeton, I am especially grateful for my cousin Anya who gave me many opportunities to escape to New York. Most of all, I am thankful to my parents. They have supported me through every single step of this journey, answering every time I call. I am so lucky to have them.

In memory of my Nana Sandy, who led an extraordinary life

Relation to Published Work

Chapter 1, Chapter 2, and parts of Chapter 3 are adapted from Linzer et al. (2025) which I wrote in collaboration with Lucia Armillotta, Eve Ostriker, and Eliot Quataert. I produced all of the figures in Chapter 2 relating to CR protons, but I include some results that are presented in more detail in Armillotta et al. (2025) on which I am the third author. Both of these works have been accepted for publication in The Astrophysical Journal. The discussion of the equipartition estimate of magnetic fields in Chapter 3 is based on work written in collaboration with Lucia Armillotta, Eve Ostriker, and Eliot Quataert, which is in preparation to be submitted. In Chapter 4, I describe ongoing work in which I reproduce many of the results presented in Chapter 2 and Chapter 3 in a different galactic environment.

I have presented this work at the International Astronomical Union General Assembly (August 2024) and at Cosmic Rays 3: The Salt of the Star Formation Recipe (October 2024).

Contents

Abstract 3

Acknowledgements 4

Relation to Published Work 8

List of Figures 13

1 Introduction **16**

1.1 Modern Astronomical Observations 17

1.2 Numerical Models 19

1.3 CR Transport in TIGRESS 20

1.4 Outline of the Thesis 22

2 The Cosmic Ray Transport Model **23**

2.1 Introduction 23

2.2 Methods 24

2.2.1 TIGRESS Simulation 24

2.2.2 CR Transport Equations 25

2.2.3 CR Proton and Electron Momentum Spectra 30

2.2.4 CR Energy Injection 33

2.2.5 Scattering Coefficient 35

2.2.6 Ionization Fraction 39

2.2.7 Energetic Losses 41

2.2.8 CR Spectrum . . . 42
2.3 Results . . . 43
2.3.1 CR Distribution . . . 43
2.3.2 Choice of Perpendicular Scattering Coefficient . . . 45
2.3.3 Energy Losses . . . 48
2.3.4 CR Spectrum . . . 54
2.4 Discussion . . . 59
2.5 Summary . . . 63
2.A Effects of MHD Relaxation . . . 64
2.B Proton Losses . . . 64
2.B.1 Pion Production . . . 64
2.B.2 Ionization . . . 66
2.B.3 Coulomb . . . 67
2.B.4 Energetic Loss Profiles . . . 67
2.C Electron Losses . . . 69
2.C.1 Synchrotron . . . 69
2.C.2 Inverse Compton . . . 69
2.C.3 Bremsstrahlung . . . 71
2.C.4 Ionization and Coulomb . . . 72
2.D Proton Spectrum . . . 73

3 Synchrotron Emission and the Estimation of Magnetic Fields 77
3.1 Introduction . . . 77
3.2 Methods . . . 80
3.2.1 TIGRESS Models . . . 80
3.2.2 Synthetic Synchrotron Emission . . . 80
3.2.3 Equipartition Estimate . . . 82
3.3 Results . . . 84

3.3.1 Mock Synchrotron Maps . . . 84
3.3.2 Extracting the CRE Spectral Slope . . . 85
3.3.3 Traditional Equipartition Estimate . . . 89
3.3.4 Alternative Estimates of Magnetic Field Strength . . . 96
3.3.5 Polarization . . . 102
3.4 Discussion . . . 105
3.4.1 Modeling Radio Emission . . . 105
3.4.2 Equipartition at Different Scales . . . 106
3.4.3 Accuracy of Alternative Estimates . . . 106
3.5 Conclusions . . . 108

4 Inner Galaxy Model 110

4.1 Introduction . . . 110
4.2 Methods . . . 111
4.3 Results . . . 112
4.3.1 CR Distribution . . . 112
4.3.2 CR Transport . . . 115
4.3.3 CR Spectrum . . . 120
4.3.4 Synchrotron Emission and Equipartition Estimate . . . 122
4.4 Discussion . . . 129
4.4.1 Comparison to Observations . . . 129
4.4.2 Comparison to Other Models . . . 130
4.5 Summary . . . 131
4.A Inner Galaxy Radiation Field . . . 132
4.B Low $\Sigma_{\rm SFR}$ Snapshots . . . 134
4.B.1 Energetic Losses . . . 134
4.B.2 Spectrum . . . 134

5 Conclusions and Future Work **139**

Bibliography **142**

List of Figures

2.1 Vertical and horizontal slices of MHD and CR variables in the R8 model . . . 44

2.2 Scattering coefficient and estimated CR mean free path as a function of gas temperature . . . 46

2.3 Vertical slices of the CRE energy distribution comparing different choices of the perpendicular scattering coefficient . . . 47

2.4 Vertical profiles of the CRE spectrum in each CRE energy bin and for two choices of the perpendicular scattering coefficient . . . 49

2.5 Vertical profiles of the CRE energetic loss rates at different CRE energies . . 50

2.6 Vertical profiles of the CRE loss, transport, and diffusion timescales at different CRE energies . . . 53

2.7 Injected and midplane CRE spectra in the R8 model compared to direct observations from AMS-02 . . . 55

2.8 Injected and midplane CRE spectral slope compared to estimations from direct observations and modeling . . . 58

2.9 Comparison of the midplane power-law slope of the simulated CRE spectra for three choices of injection spectrum . . . 60

2.10 Comparisons of the CRE vertical profile and spectrum before and after live MHD relaxation . . . 65

2.11 Vertical profiles of the CR proton energetic loss rates at different CR energies 68

2.12 Vertical profiles of the CR proton loss, transport, and diffusion timescales at different CR energies 74
2.13 Injected and midplane CR proton spectra in the R8 model compared to direct observations with AMS-02 75
2.14 Injected and midplane CR proton spectral slope 76

3.1 Midplane slices and vertically-integrated quantities used to model synchrotron emission 86
3.2 Comparison of the simulated CR power law slope to the value estimated from the mock synchrotron observations for four post-processed snapshots 88
3.3 Snapshot of vertically integrated and mass-averaged quantities in the R8 model relevant to the equipartition estimate of magnetic fields 91
3.4 Comparison of the simulated and estimated magnetic field strength using the equipartition assumption in the R8 model 92
3.5 Snapshot of vertically integrated and mass-averaged quantities in the R8 Arm model relevant to the equipartition estimate of magnetic fields 94
3.6 Comparison of the simulated and estimated magnetic field strength using the equipartition assumption in the R8 Arm model 95
3.7 Comparison of the simulated and estimated magnetic field strength using three different approximations of the CR energy density 98
3.8 Simulation snapshot showing synchrotron emission, magnetic field direction, and estimated magnetic field direction from mock synchrotron polarization measurements 103
3.9 Comparison of the simulated and estimated magnetic field direction using mock synchrotron polarization measurements 104

4.1 Vertical and horizontal slices of MHD and CR variables in the R2 model . . . 113

4.2 Vertical profiles of the CRE energy spectrum in the R2 model for all CRE energies . . . 115
4.3 CR mean free path and scattering coefficient as a function of gas temperature comparing the R8 and R2 models . . . 116
4.4 Vertical profiles of CRE energetic loss rates in the R2 model at different CRE energies . . . 118
4.5 Vertical profiles of CRE loss, transport, and diffusion timescales in the R2 model at different CRE energies . . . 119
4.6 Injected and midplane CR electron and proton spectra in the R2 model . . . 121
4.7 Injected and midplane CR electron and proton spectral slopes in the R2 model 123
4.8 Snapshot of vertically integrated and mass-averaged quantities in the R2 model relevant to the equipartition estimate of magnetic fields . . . 125
4.9 Comparison of the simulated and estimated magnetic field strength using the equipartition assumption with the R2 model . . . 127
4.10 Comparison of the simulated and estimated magnetic field strength in the R2 model for three different approximations of the CR energy density . . . 128
4.11 Vertical profiles of the CRE energetic loss rates in the R2 model for the low-$\Sigma_{\rm SFR}$ snapshots . . . 135
4.12 Vertical profiles of the CRE loss, transport, and diffusion timescales in the R2 model for the low-$\Sigma_{\rm SFR}$ snapshots . . . 136
4.13 Injected and measured CR electron and proton spectra in the R2 model for the low-$\Sigma_{\rm SFR}$ snapshots . . . 137
4.14 Injected and measured CR electron and proton spectral slopes in the R2 model for the low-$\Sigma_{\rm SFR}$ snapshots . . . 138

Chapter 1

Introduction

At the start of the 20th century, scientists knew there was *something* ionizing the air around them. Completely self-contained and shielded detectors, called electroscopes, revealed that the air within them was ionized, even when no external source of radiation was obviously present (for a review, see e.g. Rossi, 1964). Many theorized that the Earth itself was the source of the ionizing radiation, as spontaneous radioactivity and radioactive elements had recently been discovered (e.g. Becquerel, 1896; Curie et al., 1898).

Others, however, argued that the source of ionization must be from beyond our planet (see e.g., review by De Angelis, 2010). The strongest evidence in support of this hypothesis came in 1912, when Victor Hess used a hot air balloon to measure ionization as a function of altitude. He found that the higher he flew, the higher the rate of ionization he measured, even at night or during a solar eclipse (Hess, 1912 translated to English in Hess, 2018). Therefore, he knew that whatever the source of ionization was, it must originate beyond Earth and could not be coming from the Sun. At that time, it was thought that this source was electromagnetic radiation, most likely gamma-rays, leading to the name of "cosmic rays" (CRs) (Friedlander, 2012).

Years later, additional observations found that the ionization rate depended not only on altitude, but also on latitude, indicating that the CRs were interacting with Earth's mag-

netic field (e.g. Clay, 1927; Compton, 1936). This could only be possible if CRs were not electromagnetic radiation but instead were charged particles. Additional measurements revealed that these particles had extremely high energies, from 10^9 to nearly 10^{12} eV, although current observations find that CRs can reach energies of 10^{20} eV (Compton, 1936; Zweibel, 2013). It was still a question, however, how the CRs could gain so much energy.

Enrico Fermi presented a possible solution to this issue in 1949 when he described a method in which particles were accelerated through interactions with moving, magnetized clouds in the interstellar medium (ISM) (Fermi, 1949). The idea was developed further when multiple groups realized acceleration could also be achieved through interactions with astrophysical shocks (e.g. Axford et al., 1977; Blandford & Ostriker, 1978; Bell, 1978a,b). Observations have confirmed that shocks produced in supernova (SN) explosions are the primary source of CRs (see review by Caprioli, 2023, and references therein).

In the current day, we understand CRs to be high energy, charged particles dominated by protons, with a smaller fraction of electrons, positrons, and heavier nuclei (e.g. Blasi, 2013; Zweibel, 2013; Grenier et al., 2015). Although there are a factor of $\sim 10^9$ fewer CRs by number compared to thermal particles in the ambient ISM, the CR pressure is similar to the thermal, turbulent, and magnetic components (e.g. Ferrière, 2001; Elmegreen & Scalo, 2004; Cox, 2005). This suggests that CRs can fundamentally impact the dynamics of gas in galaxies, perhaps most importantly by contributing to the driving of galactic winds (e.g. Recchia, 2020; Ruszkowski & Pfrommer, 2023). Moreover, CRs can also be an important source of heating and ionization of the dense ISM, which is shielded from far-ultraviolet (FUV) and photoionizing radiation (e.g. Padovani et al., 2020; Gabici, 2022).

1.1 Modern Astronomical Observations

CRs are observed directly in the solar neighborhood using ground-based observatories or space-based detectors such as AMS-02 (Aguilar et al., 2013) or Voyager (Stone et al., 2019).

These measurements show that above ~ 1 GeV, CRs follow a broken power law distribution that extends up to PeV values. Lower energy (MeV-GeV) CRs are also present and are more important to ionization and heating of the ISM (e.g. Draine, 2011), but the spectrum is much more uncertain due to modulation by the Solar wind (e.g. Padovani et al., 2020).

Beyond the local neighborhood, our understanding of CR properties and transport within the ISM depends on indirect probes of their spectral and spatial distribution. For example, hadronic interactions between CR protons and the ambient ISM produce neutral pions which decay and emit gamma radiation. Gamma-ray observations of high-density environments can therefore help to constrain the low energy CR spectrum (e.g. Neronov et al., 2017), and gamma-ray emission from galactic center regions can help to constrain CR transport under starburst conditions (e.g. Crocker et al., 2021). Gamma-ray radiation can also be produced through inverse Compton (IC) or bremsstrahlung interactions of CR leptons (e.g. Zweibel, 2013).

When gamma-ray observations are not possible, radio synchrotron emission can provide insight into the CR population. Synchrotron radiation is produced through the interaction of CR electrons (CREs) with the local magnetic field. Therefore, even though CREs make up a much smaller fraction of the total CR population, about a factor of 100 fewer in number compared to protons (e.g. Zweibel, 2013), they are important probes of the CR distribution in both the Milky Way and in extragalactic sources. Synchrotron observations are also commonly employed to obtain estimates of magnetic field strengths, under the assumption of equipartition between the CR and magnetic energy density (e.g. Beck & Krause, 2005). This assumption is not necessarily valid in all galaxies, but still provides one of the only ways to estimate the magnitude of the magnetic field in extragalactic sources.

Inferring the distribution of CRs from synchrotron emission depends on accurately understanding the relative spectra of CR electrons and protons. This is not straightforward, since the CRE population has both a much lower amplitude compared to that of the protons, and also a different spectral shape. The distribution of CR protons above GeV energies is

well approximated by a single power law (e.g. Padovani et al., 2021). Electrons, however, are subject to significant energetic losses including ionization, bremsstrahlung, synchrotron and IC (e.g. Schlickeiser, 2002). These losses each have a different scaling with energy, thereby producing energy dependent steepening of the CRE spectrum (e.g. Evoli et al., 2020a).

1.2 Numerical Models

Many code packages have been developed to solve for the propagation and spectral evolution of multiple CR species in static models of the Galaxy including GALPROP (Strong & Moskalenko, 1998; Moskalenko & Strong, 1998), USINE (Maurin et al., 2001; Putze et al., 2010), DRAGON (Evoli et al., 2008, 2017; Maccione et al., 2011), and PICARD (Kissmann, 2014). The methods adopted in these and similar traditional CR propagation packages are extremely effective in reproducing a wide range of CR observables, including spectra, abundances of different CR species, and non-thermal emission. They rely, however, on simplified prescriptions for the gas properties and CR propagation. In particular, since the underlying gas models are not based on direct MHD simulations, they do not include dynamical transport of CRs based on a realistic turbulent magnetic field, and the scattering coefficients are set as model parameters rather than being computed locally from spatially-varying ISM properties.

Codes such as CREST (Winner et al., 2019, 2020) and CRIPTIC (Krumholz et al., 2022; Sampson et al., 2023) model CR transport by solving the Fokker-Planck equation (with some approximations), but can be applied to outputs from MHD simulations, allowing for a more realistic magnetic field structure. Additionally, models which self-consistently evolve spectrally-resolved CREs and MHD variables in a time-dependent fashion have been used to study many different astrophysical environments across a wide range of scales including galaxy clusters (e.g. Miniati et al., 2001), the CGM and ISM (e.g. Girichidis et al., 2020,

2022, 2024; Ogrodnik et al., 2021), Fermi bubbles (e.g. Yang & Ruszkowski, 2017; Böss et al., 2023), and MHD flows and shocks (e.g. Vaidya et al., 2018).

Several groups have performed spectrally-resolved studies of CRE transport in MHD galaxy simulations, which they use to compare to observations including the directly observed CR spectra as well as radio and gamma-ray emission (e.g. Werhahn et al., 2021a,b; Hopkins et al., 2022a,b). These works are most similar to the results that we will present in this thesis, although they are generally based on larger scale simulations.

1.3 CR Transport in TIGRESS

With numerical models of the ISM that have realistic magnetic field structure (requiring both sheared rotation and turbulence as driven by correlated SNe) and realistic structure of the multiphase gas, it is possible to directly simulate the transport of both CR protons and electrons. By modeling a range of CR energies, it is furthermore possible to investigate the energy dependence of CR transport including the effects of both energy-dependent scattering and losses. Simulations of this kind enable the creation of synthetic synchrotron emission, therefore providing a test of standard CR diagnostic techniques.

Previously, Armillotta et al. (2021, 2022, 2024) investigated the transport of GeV CR protons within the TIGRESS MHD simulations, which model local regions of galactic disks (Kim & Ostriker, 2017; Kim et al., 2020), allowing for a range of environments. Because the original TIGRESS simulations did not include CRs, Armillotta et al. (2021, 2022) calculated the transport of CRs in post-processing using the two-moment algorithm for CR transport (Jiang & Oh, 2018) implemented in the *Athena++* MHD code (Stone et al., 2020). In the original extension of the two-moment scheme described in Armillotta et al. (2021), self-consistent scattering was implemented for a single relativistic fluid, considering either a CR kinetic energy of 1 GeV or 30 MeV.

CR transport is controlled at large scales by the geometry of the magnetic field, which is advected by the thermal gas, and at small scales by energy-dependent scattering (e.g. Zweibel, 2017; Blasi et al., 2012; Evoli et al., 2018). Low and moderate-energy CRs ($\lesssim$ 100 GeV), which resonate only with extremely small-scale perturbations in the magnetic field, are believed to scatter primarily off Alfvén waves excited by the CRs themselves via the resonant streaming instability (the self-confinement scenario, e.g. Kulsrud & Pearce, 1969; Wentzel, 1974). This is in contrast to higher-energy ($\gtrsim$ 100 GeV) CRs, which are believed to be scattered by turbulent fluctuations that originate from other ISM dynamical processes (the extrinsic turbulence scenario e.g. Chandran, 2000; Yan & Lazarian, 2002).

In line with the self-confinement scenario, Armillotta et al. (2021) treat the transport of the CR fluid in terms of advection along with the background thermal gas, streaming at the local Alfvén speed, and diffusion relative to the Alfvén wave frame. The rate of diffusion is determined by a scattering coefficient that depends on local gas properties, rather than using a constant value or a value that scales only with CR energy, as is commonly done in ISM simulations including CRs (see reviews by Hanasz et al., 2021; Ruszkowski & Pfrommer, 2023). Specifically, in this approach the scattering coefficient is determined by the local balance between wave excitation and damping mediated by local gas properties (considering both ion-neutral damping and nonlinear Landau damping, e.g. Kulsrud 2005). Armillotta et al. (2021) found the scattering coefficient to vary significantly between different ISM phases, spanning more than four orders of magnitude. To properly represent transport in a resolved, multiphase ISM, it is therefore critical to include this self-consistent computation of the diffusion rate, as CR transport differs greatly depending on local ISM properties including density, sound speed, and ionization fraction.

1.4 Outline of the Thesis

In Chapter 2 we present our scheme for modeling energy-dependent CR transport of protons and electrons, extending the method developed in Armillotta et al. (2021). We apply this method to TIGRESS simulations of the solar neighborhood and show that our transport scheme produces CR spectra consistent with direct observations at Earth. In Chapter 3 we use these post-processed simulations to produce synthetic maps of synchrotron emission. With these mock observations, we investigate how well we can extract information about the CRE spectrum and magnetic field. We post-process TIGRESS simulations of a high surface-density environment representing inner galaxy conditions in Chapter 4 to investigate how CR transport can vary in different environments. In Chapter 5 we conclude with a summary of our results and a discussion of possible future applications of this work.

Chapter 2

The Cosmic Ray Transport Model

2.1 Introduction

In this chapter, we extend the scheme of Armillotta et al. (2021) to track the propagation of spectrally resolved CR protons and electrons. The new scheme models the transport of multiple CR fluids, each representing CRs of a given species within a given range of momentum, and incorporates energy-dependent injection, scattering, and collisional losses. We use the updated scheme to calculate the transport of $1 - 100$ GeV CR protons and electrons by post-processing the TIGRESS simulation of the solar neighborhood environment. To do so, we make the simplifying approximation that CRs in different momentum bins evolve independently. While the spectral decoupling of bins is a limitation, our model nevertheless enables a study of energy-dependent transport of CREs in physically realistic models of the multiphase ISM at very high spatial resolution, in which the scattering rate is computed within the self-confinement paradigm and dynamical transport (both advection and streaming) are included. Because the underlying TIGRESS ISM model is consistent with solar neighborhood conditions (see Kim & Ostriker, 2017; Gong et al., 2018; Kado-Fong et al., 2020; Kim et al., 2020), and we adopt a CR injection rate based on local constraints, our results can be compared to direct observations of CRs in the solar neighborhood.

The chapter is organized as follows. In Section 2.2, we describe the TIGRESS simulation of the solar neighborhood, summarize the CR transport method used in Armillotta et al. (2021), and describe the updates made to model multi-group CR spectra. In Section 2.3, we present the first results of our multi-group simulations, including the spatial distribution (Section 2.3.1) and energy spectrum (Section 2.3.4) of CREs. We compare our results to other recent models in Section 2.4. A summary is provided in Section 2.5.

2.2 Methods

We model the propagation of CRs within the TIGRESS simulation of the solar neighborhood (see Section 2.2.1) using a two-moment scheme for CR transport, with detailed methods developed in Armillotta et al. (2021, 2024) described in Section 2.2.2. Extension of the CR method to model separate groups of CR protons and electrons from 1-100 GeV, with a defined injection spectrum and energy-dependent scattering driven by the streaming instability, is described in Section 2.2.3 - Section 2.2.5. Section 2.2.6 - Section 2.2.8 describe the methods implemented to model losses and to compute the final CR spectra.

2.2.1 TIGRESS Simulation

The TIGRESS framework (Kim & Ostriker, 2017) is built with the code *Athena* (Stone et al., 2008) in which the ideal MHD equations are solved in a shearing periodic box (Stone & Gardiner, 2010). TIGRESS is designed to model the multiphase ISM by including star formation feedback via time-dependent FUV radiation associated with recent star formation, which heats warm and cold gas via the photoelectric effect on small grains, as well as Type II SN energy inputs, which create the hot medium via strong shocks. TIGRESS includes optically thin cooling, taking a simplified approach with a fitting function for warm/cold gas and tabulated values for hot gas in the original implementation of Kim & Ostriker (2017) for the models employed here (a more sophisticated non-equilibrium formulation was introduced

by Kim et al. 2023b). Gravity is included both as gas self-gravity, which leads to localized collapse and creation of star cluster particles, and an external potential from both a stellar disk and dark matter halo. The simulation accurately evolves magnetic fields, which is necessary for both CR transport and synchrotron emission.

Star formation is modeled through the use of sink particles, which represent unresolved stellar clusters. Based on the age of each particle, and assuming a stellar population with a Kroupa IMF, the rate of SNe and FUV luminosity is taken from STARBURST99 (Leitherer et al., 1999). In the CR post-processing, star cluster particles act as sources of CR injection (see Section 2.2.4).

Kim et al. (2020) and Ostriker & Kim (2022) present results from a range of TIGRESS models covering different galactic conditions, and Armillotta et al. (2022) studied the transport of 1 GeV CR protons in three different environments via post-processing. Here, we apply CR post-processing to the `R8` simulation, which is designed to represent conditions similar to the solar neighborhood. The same MHD model was previously used for the analysis of GeV CRs in Armillotta et al. (2021) and Armillotta et al. (2024). The `R8` model represents a patch of the galactic disk with $L_x = L_y = 1024$ pc and height $L_z = 7168$ pc. The simulation we use has a uniform grid with $\Delta x = 8$ pc. Although there are TIGRESS simulations with higher resolution, the models at a resolution of 8 pc show convergence of both gas and CR properties (Kim & Ostriker, 2017; Armillotta et al., 2021).

For this work, we select eight snapshots from the `R8` simulation between times of $200-550$ Myr. The snapshots were chosen to exclude the initial transient behavior of the TIGRESS simulations and to cover a range of star formation and feedback cycles.

2.2.2 CR Transport Equations

We model CR transport with the two-moment scheme originally developed by Jiang & Oh (2018) within the code *Athena++* (Stone et al., 2020). This method was later adapted for use with the TIGRESS framework by Armillotta et al. (2021). Extending the previous work,

which considered only one CR fluid representing CR protons with a single energy, here we evolve multiple non-interacting CR fluids, each representing either CR protons or electrons within a given range of energies. Each individual CR component, denoted by the subscript j, is evolved independently, with transport following the same equations as in Armillotta et al. (2021):

$$\frac{\partial e_{\mathrm{c},j}}{\partial t} + \nabla \cdot \mathbf{F}_{\mathrm{c},j} = -(\mathbf{v} + \mathbf{v}_{\mathrm{s},j}) \cdot \overleftrightarrow{\sigma}_{\mathrm{tot},j} \cdot [\mathbf{F}_{\mathrm{c},j} - \mathbf{v} \cdot (\overleftrightarrow{\mathbf{P}}_{\mathrm{c},j} + e_{\mathrm{c},j}\, \overleftrightarrow{\mathbf{I}})] \tag{2.1}$$

$$\frac{1}{v_{\mathrm{m}}^2}\frac{\partial \mathbf{F}_{\mathrm{c},j}}{\partial t} + \nabla \cdot \overleftrightarrow{\mathbf{P}}_{\mathrm{c},j} = -\overleftrightarrow{\sigma}_{\mathrm{tot},j} \cdot [\mathbf{F}_{\mathrm{c},j} - \mathbf{v} \cdot (\overleftrightarrow{\mathbf{P}}_{\mathrm{c},j} + e_{\mathrm{c},j}\, \overleftrightarrow{\mathbf{I}})]\,, \tag{2.2}$$

where $e_{\mathrm{c},j}$ is the CR energy density, $\mathbf{F}_{\mathrm{c},j}$ is the CR flux vector, and $\overleftrightarrow{\mathbf{P}}_{\mathrm{c},j}$ is the CR pressure tensor. We adopt an adiabatic equation of state and assume the CR pressure is isotropic, such that $\overleftrightarrow{\mathbf{P}}_{\mathrm{c},j} = P_{\mathrm{c},j}\, \overleftrightarrow{\mathbf{I}}$, with $P_{\mathrm{c},j} = (\gamma - 1)e_{\mathrm{c},j}$. Here, $\overleftrightarrow{\mathbf{I}}$ is the identity tensor.

In line with most MHD simulations that include a CR fluid, we make the simplifying assumption that CRs are relativistic, and therefore, the adiabatic index of the CR fluid is $\gamma_{ad} = 4/3$ (e.g. Pfrommer et al., 2017; Butsky et al., 2020; Bustard & Zweibel, 2021; Werhahn et al., 2021a). We note that while this assumption is always valid for CR electrons, the CR protons modeled in this work are not all strictly relativistic, so the actual adiabatic index of the CR proton fluids can differ slightly from 4/3. Specifically, the true value of γ_{ad} is $\lesssim 1.4$ for $p = 2$ GeV/c (corresponding to our lowest momentum bin), and it decreases with increasing p, reaching $\gamma_{ad} = 4/3$ for $p \geq 10$ GeV/c (see Girichidis et al., 2022).

Theoretically, the maximum velocity at which relativistic CRs can propagate is the speed of light, c. However, in Equation 2.2, we limit the maximum CR velocity to $v_{\mathrm{m}} \approx 10^4$ km/s $\ll c$. Jiang & Oh (2018) show that the simulation outcomes are not sensitive to the value of v_{m} as long as v_{m} remains larger than any other speed in the simulation. The reduced speed of light approximation allows us to reduce the computational time of the simulation by increasing the size of the time step allowed by the CFL condition.

In Equation 2.1 and Equation 2.2, $\mathbf{v}$ is the gas velocity, while $\mathbf{v}_{\mathrm{s},j}$ is the streaming velocity in the direction determined by the CR pressure gradient:

$$\mathbf{v}_{\mathrm{s},j} = -v_{\mathrm{A},i}\hat{B}\frac{\hat{B}\cdot\nabla P_{\mathrm{c},j}}{|\hat{B}\cdot\nabla P_{\mathrm{c},j}|}\,. \tag{2.3}$$

Here, $v_{\mathrm{A},i} = B/\sqrt{4\pi\rho_{\mathrm{i}}}$ is the ion Alfvén speed, with B the magnetic field strength and ρ_{i} the ion density, allowing for partial ionization in gas at $T < 5\times10^4$ K (see Section 2.2.6). The magnitude of the CR streaming velocity is the same for all CR components, but the direction differs depending on the value of $\nabla P_{\mathrm{c},j}$.

The diagonal tensor $\overleftrightarrow{\sigma}_{\mathrm{tot},j}$ is the wave-particle interaction coefficient. In the Jiang & Oh (2018) implementation, its component along the magnetic field direction accounts for both scattering and streaming, and is defined as:

$$\sigma^{-1}_{\mathrm{tot},\parallel,j} = \sigma^{-1}_{\parallel,j} + \frac{v_{\mathrm{A},i}}{|\hat{B}\cdot\nabla P_{\mathrm{c},j}|}(P_{\mathrm{c},j} + e_{\mathrm{c},j})\,, \tag{2.4}$$

where $\sigma_{\parallel,j}$ is the scattering coefficient (see Section 2.2.5). Perpendicular to the magnetic field direction, there is only scattering, such that $\sigma_{\mathrm{tot},\perp,j} = \sigma_{\perp,j}$. As noted by Armillotta et al. (2021), in the time-independent limit of Equation 2.2 ($\partial\mathbf{F}_{\mathrm{c},j}/\partial t \approx 0$ or large v_{m}), the flux becomes:

$$\mathbf{F}_{\mathrm{c},j} = \frac{4}{3}e_{\mathrm{c},j}(\mathbf{v}+\mathbf{v}_{\mathrm{s},j}) - \overleftrightarrow{\sigma}_j^{-1}\cdot\nabla P_{\mathrm{c},j} \tag{2.5}$$

and the work on the right-hand side of the CR energy equation reduces to

$$(\mathbf{v}+\mathbf{v}_{\mathrm{s},j})\cdot\nabla P_{\mathrm{c},j} \tag{2.6}$$

This clearly shows that the transport of CRs is given as a sum of advection ($4/3e_{\mathrm{c},j}\mathbf{v}$), streaming ($4/3e_{\mathrm{c},j}\mathbf{v}_{\mathrm{s},j}$), and diffusion ($-\overleftrightarrow{\sigma}_j^{-1}\cdot\nabla P_{\mathrm{c},j}$).

We note that, by evolving each CR momentum (or energy) component independently, our model neglects transfer across momentum bins. In Armillotta et al. (2025), we discuss

how Equation 2.1 and Equation 2.2 would be modified when adiabatic energy transfer is taken into account, showing that the coefficients of the source terms change. Specifically, they become $-(\gamma_{\rm j}-3)\,\overset{\leftrightarrow}{\sigma}_{{\rm tot},j}\cdot(\mathbf{v}+\mathbf{v}_{{\rm s},j})\cdot(\mathbf{F}_{{\rm c},j}-(\gamma_j/3)\mathbf{v}e_{c,j})$ and $-\overset{\leftrightarrow}{\sigma}_{{\rm tot},j}\cdot(\mathbf{F}_{{\rm c},j}-(\gamma_j/3)\mathbf{v}e_{c,j})$ for Equation 2.1 and Equation 2.2, respectively, assuming that the CR distribution function in each bin can be approximated by a power law $f_j \propto p^{-\gamma_j}$. For $\gamma_j = 4$, we recover the exact form of the source terms used in Equation 2.1 and Equation 2.2. In our simulations, γ_j varies from -4.3 (the injection slope) to -5.3 (see Section 2.3), implying that the resulting difference in the individual source terms is small. As demonstrated in Armillotta et al. (2025), while accounting for energy transfer may lead to a slight shift of the final CR spectrum in momentum space, the overall behavior and key conclusions of the present study remain unchanged.

If we included energy transfer between momentum bins, there would be an additional source term associated with CR energetic losses (described in Section 2.2.7). When any CR interacts with the background gas, radiation field, or magnetic field, it loses energy and would therefore move into a lower-momentum bin, but we do not add energy into the lower-momentum bin representing this shift. We find, however, that the injected CR spectrum is sufficiently steep that energy shifted from a higher to lower momentum bin is not significant.

Energy and momentum are transferred between the CRs and the surrounding gas at a rate determined by the right-hand side of Equation 2.1 and Equation 2.2 respectively. Any energy and momentum lost (or gained) by the CRs is correspondingly applied as a source (or sink) term in the equations for gas energy and momentum. For the majority of the CR post-processing, however, we freeze the background gas and magnetic field distribution, and therefore do not include these additional terms in the MHD equations. We also omit the adiabatic work term from the CR energy equation, because it would otherwise introduce spurious sources of CR energy at interfaces between cold/warm and hot gas when there is no CR backreaction on the gas (see below).

After the total CR energy density has reached a steady state (e.g. $\int_{\rm Vol} \dot{e}_{\rm c} dx^3 \approx 0$, with *Vol* the simulation volume), however, we let the gas and CRs evolve together for a short period (2 Myr) of MHD relaxation. Armillotta et al. (2024) found that when the gas is frozen, there may be locations (especially at shock interfaces between diffuse hot gas and other phases) where the magnetic fields remain aligned perpendicular to the density gradient. In this situation, CRs may be trapped in dense regions, which produces large CR pressure gradients at the boundaries between the warm, dense gas and the hot, diffuse regions. If MHD back-reaction is not permitted, the large CR gradient at the interface is preserved. As discussed in Armillotta et al. (2024), it is therefore necessary during the stage of the solution when MHD is frozen to omit the work term in the CR energy equation to avoid an unphysical enhancement in CR energy. Conversely, we include the adiabatic work term during the MHD relaxation step. We note, however, that in the midplane region the work term is generally small compared to loss terms because the CR pressure is quite uniform, due to strong wave damping in neutral gas.

When the background gas is briefly allowed to evolve, the CR pressure gradient at interfaces causes expansion at the surface of dense regions. The magnetic and velocity fields reorient, becoming more in line with the CR pressure gradients. This allows the CRs to escape from the dense gas, such that the overall CR distribution becomes smoother. The orientations of the magnetic and velocity fields converge for evolution times $\gtrsim 1$ Myr, as was previously demonstrated in Armillotta et al. (2024). Because star formation and feedback are not included during the MHD relaxation step, we cannot allow the gas to evolve for more than 2 Myr without losing a significant fraction of hot gas. Additionally, to be consistent with the lack of thermal energy and momentum injection, we do not inject CRs during this stage.

Due to the relatively brief interval of MHD relaxation, the vertical CR energy density profiles do not evolve to an entirely new steady state. We find, however, that neither the vertical CR energy profile nor the CR energy spectrum change significantly before and after

the MHD relaxation step. This is shown in Section 2.A.[1] All results presented in this paper are taken at the end of the MHD relaxation step.

Other works including a variable scattering model based on self-confinement have found that while the midplane ISM structure does not change significantly with the addition of CR feedback – due to efficient diffusion and thus negligible CR pressure gradients – the extraplanar region is more strongly affected (e.g. Sike et al., 2024; Thomas et al., 2024). Therefore, while we discuss the CR distribution in the extraplanar region qualitatively throughout Section 2.3, we note that these results may differ in fully self-consistent CR-MHD simulations. When comparing to to direct observations, we consider only the midplane ISM.

In Section 2.2.4 and Section 2.2.7, we describe additional source and sink terms that enter the right-hand sides of Equation 2.1 and Equation 2.2. These include the injection of energy into CRs by SNe, as well as various collisional processes through which CRs lose energy and momentum.

2.2.3 CR Proton and Electron Momentum Spectra

We model the CR spectrum by evolving 10 CR components – 5 representing protons and 5 representing electrons – each corresponding to a specific bin of momentum values. For the protons, the bins are equally divided in log space between momenta of $2 - 101$ GeV/c, corresponding to kinetic energies between $1 - 100$ GeV. The 5 bins are centered at $p_j = 2$, 5, 13, 36, and 101 GeV/c. Each bin has a width of $d\ln p = 0.1$.

The momenta of the electron bins are based on the predictions of the self-confinement scenario, which we assume in this work. According to detailed modeling of the local CR spectra, CRs in the energy range investigated here ($1 - 100$ GeV) are mostly scattered by self-excited resonant Alfvén waves (e.g. Zweibel, 2013). Since the total CR energy density is

[1] A potential concern is that in a fully self-consistent CR-MHD simulation evolved over an extended period, both the vertical MHD and CR profiles could differ from those under our present approach due to CR pressure forces on the gas. However, preliminary analysis of a new fully self-consistent TIGRESS CR-MHD simulation with a single GeV CR component (C.-G. Kim et al, in prep.) shows that the CR pressure throughout the midplane region (at $|z| \lesssim 300$pc) is nearly the same as in the present simulations.

dominated by protons, the scattering of the electrons is determined primarily by interactions with Alfvén waves generated by these protons. Therefore, we need to determine which electrons interact with the waves excited by the protons in any given momentum bin. The resonance condition of a CR with an Alfvén wave is given by

$$\pm\Omega \approx -kv_{c,\parallel}\,, \tag{2.7}$$

(e.g. Bai et al., 2019), where k is the wavevector of the Alfvén wave and $\Omega = qB/(\gamma mc)$ is the gyrofrequency for a particle with charge q (equal to $\pm e$ for protons or electrons), Lorentz factor γ, and particle mass m in a magnetic field with magnitude B. The CR velocity v_c is related to CR energy by

$$v_c = c\sqrt{1-\frac{1}{\gamma^2}} = \sqrt{1-\left(\frac{mc^2}{E}\right)^2} \tag{2.8}$$

for a CR with mass m and relativistic energy E, and $v_{c,\parallel}$ represents the component of this velocity parallel to the background magnetic field.

For a CR proton and electron to interact with the same Alfvén wave of a given wavevector k, it must be true that $\Omega_\mathrm{p}/v_\mathrm{p} = \Omega_\mathrm{e}/v_\mathrm{e}$, where the subscripts p and e indicate protons and electrons, respectively. Substituting for the gyrofrequency, we find that $\gamma_p m_p v_p = \gamma_e m_e v_e$. CR protons and electrons that are resonant with the same Alfvén waves must have the same relativistic momentum. Therefore, to model both species, we use the same bins in momentum space for both protons and electrons and will consider protons and electrons with the same momentum to have the same scattering coefficient (see Section 2.2.5).

As mentioned in Section 2.2.2, each CR fluid component has an associated energy density and flux which are evolved according to Equation 2.1 and Equation 2.2 respectively. The fluids do not interact with each other except for the determination of the scattering coefficient. We note that the energy density of CRs within a given momentum bin is related to

the CR distribution function $f(p)$ as follows:

$$\begin{aligned} e_{\mathrm{c},j} &= 4\pi \int_{\mathrm{p}-}^{\mathrm{p}+} f(p) E(p) p^2 dp \\ &\approx 4\pi f(p_j) E(p_j) p_j^3 d\ln p \,, \end{aligned} \tag{2.9}$$

where $p_\pm$ are the extrema of the bin, and $E(p)$ is the total relativistic energy for a particle of relativistic momentum p_j. Taking the approximation in the second line of Equation 2.9 makes a negligible difference, changing $e_{\mathrm{c},j}$ by less than 0.05%, because our spectral bins are sufficiently small.

The initial distribution function is defined as $f(p) = Cp^{-\gamma_{\mathrm{input}}}$ where γ_{input} is the initial spectral power law slope and C is a normalization constant, and this power law is assumed to hold for $p \geq p_{\mathrm{min}}$. We choose γ_{input} to be consistent with the initial CR distribution produced in SNR, estimated by direct observations to be approximately 4.3 (see e.g. Caprioli, 2023), although we will consider variations in this value.

We set the normalization of the CR proton distribution as follows. First, we simulate CR transport using the one-bin model as in Armillotta et al. (2021). In this case, the full CR population is modeled as if all CRs were protons with kinetic energy of 1 GeV. When this model approaches steady state, we use the resulting proton energy density ($e_{\mathrm{c,p,tot}}$) to solve for C by setting

$$e_{\mathrm{c,p,tot}} = 4\pi \int_{\mathrm{p_{min}}}^{\infty} f(p) E(p) p^2 dp \tag{2.10}$$

where $p_{\mathrm{min}} = 1$ GeV/c. Below this value the injection slope is uncertain, and the relativistic assumption is not valid. By changing the value of p_{min}, we only change the overall normalization of the initial CR distribution. The CRE spectrum is initialized such that it has the same spectral shape as the CR protons, but $e_{\mathrm{c,e,tot}}$ is reduced by a factor of 50 compared to $e_{\mathrm{c,p,tot}}$. This is consistent with direct observations of the CR spectra (e.g. Zweibel, 2013).

This process for setting the normalization of the energy spectrum of the CR protons and electrons in the initial conditions is done only to reduce the time it takes for the multi-fluid

simulations to reach a steady state. The final CR distributions are not dependent on the initialization.

2.2.4 CR Energy Injection

The method for injecting energy of the CR fluid onto the grid based on SN feedback from star cluster particles is described in detail by Armillotta et al. (2021) when considering CRs with a single energy. We extend this method to allow for injection of CRs with different momenta. The total rate of CR energy injected from SNe is

$$\dot{E}_c = \epsilon_{\rm inj,tot} E_{\rm SN} \dot{N}_{\rm SN} \tag{2.11}$$

where $E_{\rm SN} = 10^{51}$ erg is the energy released by one SN event, and $\dot{N}_{\rm SN}$ is the rate at which SNe occur. The SN rate from a given star cluster particle is defined as $\dot{N}_{\rm SN} = m_{\rm sp}\xi_{\rm SN}(t_{\rm sp})$ where $m_{\rm sp}$ is the star cluster particle mass, and $\xi_{\rm SN}(t_{\rm sp})$ is the rate of SNe per unit mass for a star cluster particle of age $t_{\rm sp}$ as computed using STARBURST99 (Kim & Ostriker, 2017).

In the energy injection expression, $\epsilon_{\rm inj,tot}$ represents the fraction of SN energy that goes into production of CRs, assumed to be equal to 0.1 (see e.g. Caprioli, 2023). When considering only one CR fluid, Armillotta et al. (2021) assume the total injected energy goes into acceleration of 1 GeV CRs. To instead model a CR spectrum, we must divide the total injected energy between CRs of different momenta. We do so as follows.

The total CR energy density produced by one SN is

$$e_{\rm inj,tot} = \epsilon_{\rm inj,tot} \frac{E_{\rm SN}}{V}\,, \tag{2.12}$$

with V the volume in which the energy is injected. The injected CR energy density, $e_{\rm inj,tot}$, is determined by Equation 2.10 where the distribution function $f(p)$ is replaced by the

distribution of injected particles with the same power-law index ($\gamma_{\rm inj} = -4.3$) but a different normalization.[2]

The energy density injected into a single bin is

$$e_{{\rm inj},j} = \epsilon_{{\rm inj},j} \frac{E_{\rm SN}}{V} \tag{2.13}$$

where $\epsilon_{\rm inj,j}$ is the fraction of the SN energy injected into the jth bin. We substitute $E_{\rm SN}/V$ from Equation 2.12 into Equation 2.13. Then, using Equation 2.10 and the approximation in Equation 2.9, we obtain

$$\epsilon_{{\rm inj},j} = \epsilon_{\rm inj,tot} \frac{p_j^{-\gamma_{\rm inj}} E(p_j) p_j^3 d{\rm ln}p}{\int_{\rm p_{min}}^{\infty} p^{-\gamma_{\rm inj}} E(p) p^2 dp} \,. \tag{2.14}$$

Taking a relativistic limit $E(p) \approx pc$ for Equation 2.14, this simplifies to

$$\epsilon_{{\rm inj},j} \approx \epsilon_{\rm inj,tot} (\gamma_{\rm inj} - 4) \left(\frac{p_{\rm min}}{p_j} \right)^{\gamma_{\rm inj}-4} d{\rm ln}p \,, \tag{2.15}$$

(assuming $\gamma_{\rm inj} > 4$).

As in Section 2.2.3, we inject electrons with the same spectral slope as the protons, but change the normalization such that the magnitude of the electron distribution is reduced by a factor of 50 compared to the protons ($\epsilon_{\rm inj,tot} = 0.002$). Other simulations of multiple CR species have also adopted an injected ratio of 0.02 between electrons and protons (e.g. Werhahn et al., 2021a).

Like in Armillotta et al. (2021), the injected energy appears as a source term in Equation 2.1. The injection follows a Gaussian distribution around each star cluster particle, such

[2]More generally, $f(p)$ is often treated as a piecewise power law. Our implicit assumption in adopting a single power law with $p_{\rm min} = 1$ GeV/c is that $f(p)$ is flat enough below 1 GeV that the total CR energy at p <1 GeV is negligible.

that the total source term in a cell at location $\mathbf{x}$ is

$$Q(\mathbf{x}) = \frac{1}{(2\pi\sigma_{\rm inj}^2)^{3/2}} \sum_{\rm sp=1}^{N_{\rm sp}} \dot{E}_{\rm c,sp} \cdot {\rm e}^{-{\rm r}_{\rm sp}^2/2\sigma_{\rm inj}^2} \tag{2.16}$$

where Q represents the injected CR energy density per unit time and $\dot{E}_{\rm c,sp}$ is the energy injection rate (Equation 2.11) from one star cluster particle, with $r_{\rm sp} = |\mathbf{x} - \mathbf{x}_{\rm sp}|$ the distance from the cell to each contributing star particle. The sum is taken over all star particles in the simulation with age less than 40 Myr. We adopt $\sigma_{\rm inj} = 32$ pc; Armillotta et al. (2021) found that the choice of $\sigma_{\rm inj}$ did not have a significant impact on the final CR distribution.

We note that in Equation 2.1, the CR energy density is approximately linearly proportional to Q with the exception of $\sigma_{\rm tot}$ which has a weak dependence on e_c (see Section 2.2.5). Therefore, the overall normalization of the injected CR spectrum (see Equation 2.9 and Equation 2.10 in Section 2.2.3) does not have a significant effect on the rate of CR transport. The final CR distribution (and resulting synchrotron emissivity) can be renormalized after it has evolved to a steady state. This would represent, for example, a different choice of $p_{\rm min}$ or $\epsilon_{\rm inj,tot}$.

2.2.5 Scattering Coefficient

We compute the scattering coefficient in line with the predictions of the self-confinement picture. Similar to Armillotta et al. (2021), the scattering coefficient, $\sigma_{\parallel}$, is determined by balancing the growth of Alfvén waves with different damping mechanisms. We will provide a brief summary of the derivation here as well as a description of how we include the contribution of CREs.

Armillotta et al. (2021) demonstrated that, for quasi-steady CR flux (see Equation 2.5), the growth of Alfvén waves due to the streaming instability (e.g. Kulsrud, 2005) can be written as:

$$\Gamma_{\rm stream}(p_{1,j}) = \frac{\pi^2}{4} \frac{\Omega_0 m v_{\rm A,i}}{B^2} \frac{|\hat{B} \cdot \nabla P_{{\rm c},j}|}{\sigma_{\parallel,j} P_{{\rm c},j}} n_{1,j} \,, \tag{2.17}$$

where $\Omega_0 m = eB/c$, with Ω_0 the cyclotron frequency, and $p_{1,j} = \Omega_0 m/k_{\rm j} = eB/(k_j c)$ the resonant momentum for wave number k_j, which we set to the momentum of the CR bin (see Section 2.2.3). The waves propagate at the ion Alfvén speed, $v_{\rm A,i} = B/\sqrt{4\pi\rho_{\rm i}}$, where $\rho_{\rm i}$ is the ion density as defined in Section 2.2.6. The value of $n_{1,j}$, which represents the number density of CRs resonant with a given wave mode, is defined as

$$n_{1,j} \equiv 4\pi p_{1,j} \int_{p_{1,j}}^{\infty} p f(p) dp \,. \tag{2.18}$$

Here, we assume $f(p) = C(p/p_{1,j})^{-\gamma_{\rm obs}}$, where C is a normalization constant dependent on the CR energy density in the bin with momentum $p_{1,j}$ and $\gamma_{\rm obs} = 4.7$ represents a fixed power law slope consistent with observations of CR protons with kinetic energy $\gtrsim 1$ GeV (e.g. Grenier et al., 2015). The normalization constant is computed from the approximation in Equation 2.9, using the energy density of CRs within the bin centered at $p_{1,j}$, i.e. $C = e_c(p_{1,j})/[4\pi E(p_{1,j}) p_{1,j}^3 d\ln p]$. Therefore, $n_{1,j}$ simplifies to

$$n_{1,j} = \frac{e_c(p_{1,j})}{2.7 E(p_{1,j}) d\ln p} \,. \tag{2.19}$$

We note that properly speaking, the factor 2.7 in the denominator would be replaced by a numerical factor $\gamma_j - 2$ that depends on the local slope of the CR spectrum. Since the final, evolved slopes we obtain are very close to observed values, however, we have adopted the above approach for simplicity.

The value of $n_{1,j}$ is only dependent on the CR energy density and relativistic energy of bin j. We note that because $e_{\rm c}/E(p) \propto p^3 f(p)$, $n_{1,j}$ decreases with increasing momentum p for distribution functions with slope less than -3, which is always true in our simulations.

The growth of Alfvén waves is balanced by damping mediated by local gas properties. We consider both ion-neutral (IN) and nonlinear Landau (NLL) damping. The IN damping is due to collisions between ions and neutrals, and is the dominant damping mechanism in denser, poorly-ionized gas, where neutrals are not tied to magnetic fields. The IN damping

rate is (Kulsrud & Pearce, 1969)

$$\Gamma_{\rm damp,in} = \frac{1}{2}\frac{n_{\rm n} m_{\rm n}}{m_{\rm n} + m_{\rm i}} \langle \sigma v \rangle_{\rm in} \,, \tag{2.20}$$

where $n_{\rm n}$ and $m_{\rm n}$ are the number density and mean mass of neutral gas particles, and $m_{\rm i}$ is the mean mass of ions (see Section 2.2.6 for the definitions of these values). $\langle \sigma v \rangle_{\rm in} \sim 3 \times 10^{-9}$ cm^3 s^{-1} is the rate coefficient for IN collisions (Draine, 2011). If we assume that only protons contribute to the Alfvén wave growth, and balance the wave growth rate and the IN damping rate, $\Gamma_{\rm stream} = \Gamma_{\rm damp,in}$, solving for $\sigma_\parallel$ we find

$$\sigma_{\parallel,{\rm in}}(p_{1,j}) = \frac{\pi}{8}\frac{|\hat{B}\cdot\nabla P_{{\rm c},j}|}{v_{{\rm A},i} P_{{\rm c},j}} \frac{\Omega_0 m}{n_{\rm n}\langle\sigma v\rangle_{\rm in}} \frac{(m_{\rm n}+m_{\rm i})}{m_{\rm i} m_{\rm n}} \frac{n_{1,j}}{n_{\rm i}} \,. \tag{2.21}$$

This is the form of the scattering coefficient used in Armillotta et al. (2021). We now consider the contribution of both protons and electrons, so we instead solve $\Gamma_{\rm stream,p} + \Gamma_{\rm stream,e} = \Gamma_{\rm damp}$. Because this is a linear equation in $\sigma_\parallel$, the total value of $\sigma_\parallel$, including contributions from both protons and electrons, is simply

$$\sigma_{\parallel,{\rm in,tot},j} = \frac{\pi}{8}\frac{\Omega_0 m}{v_{{\rm A},i} n_{\rm n}\langle\sigma v\rangle_{\rm in}} \frac{(m_{\rm n}+m_{\rm i})}{m_{\rm i} m_{\rm n} n_{\rm i}} \left(\frac{|\hat{B}\cdot\nabla P_{{\rm c,p},j}|}{P_{{\rm c,p},j}} n_{1,{\rm p},j} + \frac{|\hat{B}\cdot\nabla P_{{\rm c,e},j}|}{P_{{\rm c,e},j}} n_{1,{\rm e},j} \right) \tag{2.22}$$

where the subscripts p and e represent the contributions made by the protons and electrons respectively. The energy density of electrons is much lower than that of protons, so the contribution of protons dominates.

We also consider NLL damping, which occurs when the thermal ions have a resonance with the beat wave formed by the interaction of two resonant Alfvèn waves. In this case, the damping rate is given by Kulsrud (2005) to be

$$\Gamma_{\rm damp,nll} = 0.3\Omega \frac{v_{{\rm t},i}}{c}\left(\frac{\delta B}{B}\right)^2 \approx 0.3\frac{8}{\pi}\frac{v_{{\rm t},i} v_{\rm p}^2}{c}\sigma_\parallel \,, \tag{2.23}$$

where Ω is the relativistic cyclotron frequency, $v_{\mathrm{t},i}$ is the ion thermal velocity, and $\delta B/B$ is the magnetic field fluctuation. The above employs the quasilinear theory relation $\nu_s = (\pi/8)\Omega(\delta B/B)^2$ for the scattering rate $\nu_s = v_p^2\sigma_\parallel$.

In the NLL case, we set $2\Gamma_{\mathrm{stream}}(p_1) = \Gamma_{\mathrm{damp,nll}}$, considering only proton contributions to wave growth.[3] Solving for $\sigma_\parallel$ then gives

$$\sigma_{\parallel,\mathrm{nll}}(p_{1,j}) = \frac{\pi}{8}\sqrt{\frac{|\hat{B}\cdot\nabla P_{\mathrm{c},j}|}{v_{\mathrm{A},i}P_{\mathrm{c},j}}\frac{\Omega_0 c}{0.3v_{\mathrm{t},i}v_{\mathrm{p}}^2}\frac{m}{m_{\mathrm{i}}}\frac{n_1}{n_{\mathrm{i}}}}\,. \tag{2.24}$$

Now when including both protons and electrons we have a quadratic expression in $\sigma_\parallel$, so

$$\sigma_{\parallel,\mathrm{nll,tot},j} = \frac{\pi}{8}\sqrt{\frac{\Omega_0 mc}{0.3v_{\mathrm{t},i}v_{\mathrm{A},i}v_{\mathrm{p}}^2}\frac{1}{m_{\mathrm{i}}n_{\mathrm{i}}}\left(\frac{|\hat{B}\cdot\nabla P_{\mathrm{c,p},j}|}{P_{\mathrm{c,p},j}}n_{1,\mathrm{p},j} + \frac{|\hat{B}\cdot\nabla P_{\mathrm{c,e},j}|}{P_{\mathrm{c,e},j}}n_{1,\mathrm{e},j}\right)}\,. \tag{2.25}$$

We solve for both $\sigma_{\parallel,\mathrm{in,tot},j}$ and $\sigma_{\parallel,\mathrm{nll,tot},j}$, then take the minimum of the two values (which corresponds to the stronger damping rate). This is a valid approximation, as in almost all regimes either IN or NLL damping will dominate.

The parallel scattering coefficient, $\sigma_\parallel$, determines transport aligned with the local magnetic field. We also consider a perpendicular scattering coefficient, $\sigma_\perp$, which represents scattering due to unresolved fluctuations in the mean magnetic field. Here, we consider two cases, one in which $\sigma_\perp = 10\times\sigma_\parallel$ (see Section 4.3 in Armillotta et al., 2021) and another case with very little to no perpendicular diffusion with $\sigma_\perp \gg \sigma_\parallel$. For the $\sigma_\perp \gg \sigma_\parallel$ case, we set $\sigma_\perp$ to a very large, fixed value (1 cm^{-2} s). Armillotta et al. (2021) do not find a significant difference between these two cases. However, they considered only 1 GeV protons where the value of $\sigma_\perp = 10\times\sigma_\parallel$ is relatively large ($\langle\sigma_\perp\rangle \lesssim 10^{-29}$ s cm^{-2} in the cold/warm ISM and $\gtrsim 10^{-27}$ s cm^{-2} in the warm/hot ionized gas). When we consider higher energy CRs, the value of $\sigma_\parallel$ is greatly reduced ($\sigma \propto n_1$ or $n_1^{1/2}$), which in turn reduces the value of $\sigma_\perp$. In

[3]Equation 2.17 and Equation 2.20 represent linear growth and damping rates of the wave amplitude. In this case, the growth rate is $2\Gamma_{\mathrm{stream}}(p_1) = \Gamma_{\mathrm{damp,nll}}$ due to non-linear effects, see Chapter 11 in Kulsrud (2005).

this case, we do see a difference in the final CR distribution depending on the definition of $\sigma_\perp$, as discussed in Section 2.3.2.

2.2.6 Ionization Fraction

In Section 2.2.5 and Section 2.2.7 we use the electron, ion, and neutral densities of the gas to determine the value of the scattering coefficient and magnitude of CR energy losses. The electron density is defined as $n_e = x_e n_H$ where x_e is the electron fraction. We find this value as in Armillotta et al. (2021). For gas with $T > 2 \times 10^4$ K, the value of x_e is interpolated from the values listed in Sutherland & Dopita (1993), which is computed under the condition of collisional ionization equilibrium.

For cooler gas, with $T \leq 2 \times 10^4$ K, the electron fraction is instead computed by balancing cosmic ray ionization with recombination for hydrogen, also allowing for low ionization potential metals to be ionized by far-UV (Draine, 2011). The free electron abundance is

$$x_e = x_{\rm M} + \frac{\sqrt{(\beta + \chi + x_{\rm M})^2 + 4\beta} - (\beta + \chi + x_{\rm M})}{2}\,. \tag{2.26}$$

Here $x_{\rm M} = 1.68 \times 10^{-4}$ is the adopted contribution from metals with ionization potential less than that of hydrogen (13.6 eV). The value of β is $\zeta_H/(\alpha_{rr} n_H)$ with ζ_H the CR ionization rate per hydrogen atom and $\alpha_{rr} = 1.42 \times 10^{-12}$ cm^3 s^{-1} the rate coefficient for radiative recombination. χ is the ratio $\alpha_{\rm gr}/\alpha_{\rm rr}$ where $\alpha_{\rm gr} = 2.83 \times 10^{-14}$ cm^3 s^{-1} is the grain assisted recombination rate coefficient.

The CR ionization rate, ζ_H, includes ionization due to CR nuclei and secondary electrons produced by primary ionization events. This value can be approximated as $\zeta_H \approx 1.5\zeta_c$, with ζ_c the ionization rate due to primary events (e.g. Padovani et al., 2020). We compute ζ_c as

$$\zeta_{\rm c} = \zeta^{\rm obs} \frac{e_{\rm c,0}}{e^{\rm obs}_{\rm c,0}}\,, \tag{2.27}$$

where $\zeta^{\rm obs} = 2 \times 10^{-16}$ s^{-1} is the average CR ionization rate measured in the local ISM (e.g. Indriolo et al., 2007). $e_{\rm c,0}$ and $e_{\rm c,0}^{\rm obs}$ are, respectively, the simulated and observed energy densities of CRs within the lowest-momentum bin, centered in $p_0 = 2$ GeV/c. To determine $e_{\rm c,0}^{\rm obs}$, we use the approximation in Equation 2.9, with $p_{\rm bin} = p_0$, and $f(p_{\rm bin})$ the observed distribution function for protons (obtained from Equation 1 in Padovani et al., 2018) evaluated at p_0.

We define the ion number density in an analogous way to n_e as $n_{\rm i} = x_{\rm i} n_H$ where $x_{\rm i}$ is the ion fraction. For $T \leq 2 \times 10^4$ K, Equation 2.26 can also be used to estimate the value of $x_{\rm i}$ as it considers only singly ionized species, so that $x_e = x_{\rm i}$. For $T > 2 \times 10^4$ K, we approximate the ion fraction directly from the electron fraction taking $x_{\rm i} = \min(x_e, 1.099)$. The maximum value 1.099 comes from the simplifying assumption that the number of free electrons is dominated by the ionization of hydrogen and helium, and that the hydrogen to helium ratio is approximately 10:1. From the ion fraction, we define the ion density as $\rho_{\rm i} = \mu_{\rm i} m_p n_{\rm i}$ where $\mu_{\rm i}$ is the ion mean molecular weight, defined as

$$\mu_{\rm i} = \frac{x_{\rm H^+} + 4(x_{\rm He^+} + x_{\rm He^{++}}) + 12 x_{\rm M}}{x_{\rm i}}\,, \tag{2.28}$$

where we approximate the mean atomic mass number of metals to be 12. To find $x_{\rm H^+}$ and $x_{\rm He^+} + x_{\rm He^{++}}$, we must assume that all hydrogen is ionized before any helium. Therefore, if $x_{\rm i} - x_{\rm M} < 1$ then $x_{\rm H^+} = x_{\rm i} - x_{\rm M}$. If all hydrogen is ionized, $x_{\rm i} - x_{\rm M} > 1$, and $x_{\rm H^+} = 1$. In this case, the fraction of ionized helium is defined as, $x_{\rm He^+} + x_{\rm He^{++}} = x_{\rm i} - x_{\rm M} - 1$.

Once we have the ion density, the neutral density is then defined as $n_{\rm n} m_{\rm n} = \rho - \rho_{\rm i}$. The magnitude of some CR losses (discussed in Section 2.2.7) depends on the fraction of neutral hydrogen rather than the total neutral density. Therefore, we define

$$x_{\rm n} = \frac{n_{\rm HI} + 2 n_{\rm H2}}{n_H}\,. \tag{2.29}$$

We approximate this value as we do for $\mu_{\rm i}$ by assuming that if $x_{\rm i} - x_{\rm M} > 1$, then all hydrogen is ionized and $x_{\rm n} = 0$. Otherwise, $x_{H^+} = x_{\rm i} - x_{\rm M}$ and $x_{\rm n} = 1 - x_{H^+}$.

2.2.7 Energetic Losses

Both CR protons and electrons lose energy to the surrounding ISM, for example through collisions with ambient atoms or through interactions with magnetic or radiation fields. We include losses as in Armillotta et al. (2021) with updates to include analytic expressions for different loss mechanisms.

Individual CRs lose energy at a rate given by

$$\left[\frac{dE}{dt}\right]_j = -v_{c,j} L(E_j) n_H \equiv -\Lambda(E_j) E_j n_H \,, \tag{2.30}$$

with E_j the relativistic energy of the particle in bin j and $v_{c,j}$ the CR velocity (Equation 2.8). $L(E_j)$ is the energy loss function described in Padovani et al. (2020).

Since CRs in the same momentum bin share the same energy, the energy density lost from CRs in a given bin is calculated as

$$\dot{e}_{{\rm c},j,{\rm loss}} = -\Lambda(E_j) n_H e_{{\rm c},j} \,. \tag{2.31}$$

This total loss rate is applied to the right-hand side of Equation 2.1. The CR fluxes are updated correspondingly by applying the following term to the right-hand side of Equation 2.2

$$\dot{F}_{{\rm c},j,{\rm loss}} = -\Lambda(E_j) n_H F_{{\rm c},j} / v_{{\rm c},j}^2 \,. \tag{2.32}$$

The loss function Λ includes the contribution from all sources of energy losses. A summary of these follows, with the exact expressions provided in Section 2.B and Section 2.C for protons and electrons, respectively.[4]

[4]Equation 2.31 and Equation 2.32 are equivalent to Equation 11 in Armillotta et al. (2021) but we introduce a new, clearer notation.

At low kinetic energies, energy losses of CR protons are dominated by either the ionization of neutral hydrogen or Coulomb interactions with free electrons. These two sources are relevant in the warm/cold, primarily neutral ISM or the hot, well-ionized medium respectively. At higher kinetic energies, greater than $\sim$1 GeV, losses are instead dominated by pion production due to collisions with atoms in the surrounding ISM. The total value of Λ for protons is then given by

$$\Lambda_{\mathrm{p},j} = \Lambda_{\mathrm{pion},j} + \Lambda_{\mathrm{ion},j} + \Lambda_{\mathrm{Coulomb},j}. \tag{2.33}$$

Similarly to protons, low energy CREs lose their energy primarily through ionization of neutral hydrogen and Coulomb interactions. In addition to these losses, CREs are also subject to energy losses due to bremsstrahlung interactions. At higher energies, synchrotron and IC losses dominate. The total Λ for electrons is given by

$$\Lambda_{\mathrm{e},j} = \Lambda_{\mathrm{synch},j} + \Lambda_{\mathrm{IC},j} + \Lambda_{\mathrm{ion},j} + \Lambda_{\mathrm{Coulomb},j} + \Lambda_{\mathrm{brem},j}. \tag{2.34}$$

As discussed in Section 2.2.2, the loss of energy by CRs in a given energy bin should result in energy gain in a lower energy bin. However, we do not include transfer of energy between CR energy bins due to these losses. The CR distribution follows a steep power law slope. Therefore, the number of CRs that would be transferred from a higher to a lower energy bin is not significant compared to the number of CRs injected by SNe.

2.2.8 CR Spectrum

We use the final values of $e_{c,j}$ to estimate the CRE spectrum, j_e. The latter is related to the CRE distribution function as $j_{\mathrm{e}}(E) = v_{\mathrm{e}} f_{\mathrm{e}}(p) p^2 dp/dE$. If we substitute this expression in Equation 2.9, we obtain

$$j_e(E_j) \approx \frac{e_{\mathrm{c},j} v_{\mathrm{e},j}}{4\pi E_j^2 d\ln E}\,, \tag{2.35}$$

where $d\ln E$ is the width of the bin in log space. In the relativistic limit $d\ln E \approx (p^2c^2/E^2)d\ln p \approx d\ln p$. The value of j_e is in units of the number per unit energy, time, area, and solid angle. To estimate the CRE spectrum at all energies we interpolate between the momentum bins, approximating j_e as a broken power law.

2.3 Results

2.3.1 CR Distribution

In Figure 2.1, we present vertical and horizontal slices (through $y = 0$ and $z = 0$ respectively) of relevant MHD and CR variables. These quantities are taken from the TIGRESS snapshot at $t = 214$ Myr following both post-processing and subsequent MHD relaxation. The first column shows the hydrogen number density, n_H, along with the young star clusters colored by their age. The second panel shows the gas temperature, T. From these two panels, we can see the transition from the disk midplane region, mostly composed of warm and cold moderate-density gas ($T \lesssim 10^4$ K, $n_H \sim 0.1 - 100$ cm^{-3}), to the extraplanar region, where most of the volume is occupied by hot, diffuse gas ($T \gtrsim 10^6$ K, $n_H \lesssim 10^{-3}$ cm^{-3}). The star clusters, which act as CR sources, are within $|z| \lesssim 200$ pc.

The next three panels represent the magnitudes of the gas flow speed v, ion Alfvén speed $v_{\rm A,i}$ (equal to the magnitude of the CR streaming velocity $\mathbf{v}_{\rm s}$), and magnetic field strength B, respectively. The arrows overlaid on each of these panels indicate the projected direction of the CR streaming velocity, gas velocity, and magnetic field, respectively. Compared to v, the magnitude of $v_{\rm A,i}$ is larger in cool, high-density, primarily neutral gas, and much smaller in hot, low-density, ionized gas. Therefore, while CR advection dominates in the hot phase, streaming can be important in the cooler gas (see also Armillotta et al., 2021, 2024). In general, $v_{\rm A,i}$ is more turbulent than v. Above $z \sim 1$ kpc, the gas velocity is predominantly oriented outward from the simulation box, due to the presence of strong outflows. Although

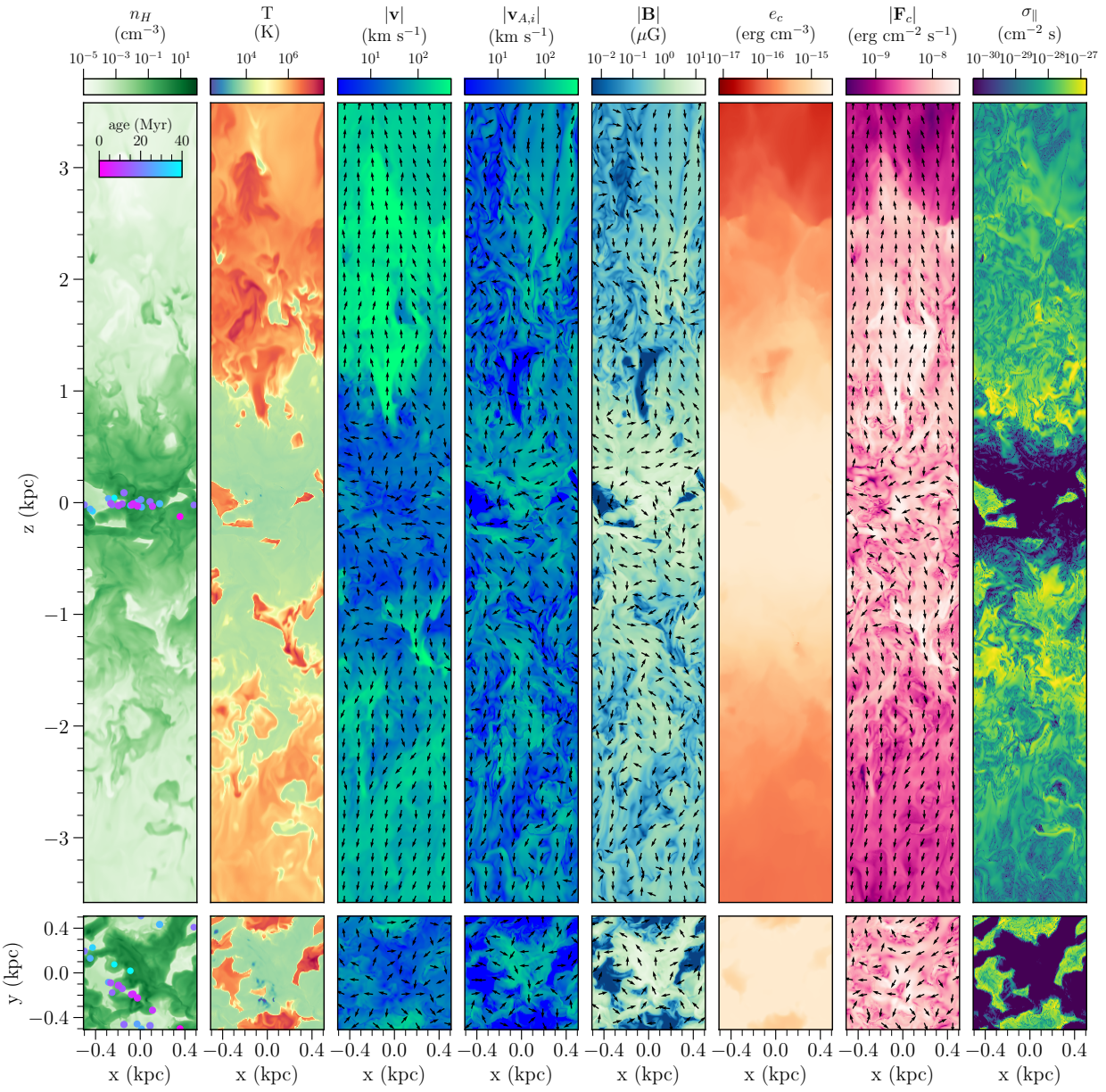

Figure 2.1: Vertical (through $y = 0$) and horizontal (through $z = 0$) slices of MHD and CR variables from the snapshot at $t = 214$ Myr. From left to right, the first five slices show number density of hydrogen (n_H), temperature (T), magnitude of the gas velocity ($|\mathbf{v}|$), magnitude of the ion Alfvén velocity ($|\mathbf{v}_{\rm A,i}|$), and magnitude of the magnetic field ($|\mathbf{B}|$). The final three slices show energy density (e_c), flux magnitude ($|\mathbf{F}_c|$), and scattering coefficient ($\sigma_\parallel$) of CREs with momentum $p = 2$ GeV/c. The arrows overlaid on the slices of gas velocity, Alfvén speed, magnetic field, and flux magnitude indicate the projected directions of the gas velocity, CR streaming velocity, magnetic field, and CR flux respectively.

there is some organization of $v_{\rm A,i}$ pointing out of the simulation box at large z, the alignment is not nearly as clear as in v.

In the last three panels, we show the energy density $e_{\rm c}$, flux $F_{\rm c}$, and parallel scattering coefficient $\sigma_\parallel$ of the lowest energy CREs ($p = 2$ GeV/c) for the case where $\sigma_\perp = 10 \times \sigma_\parallel$. As with the velocity and magnetic field, the F_c panel has the projected vectors overlaid on the magnitude. The CR energy density distribution is very smooth compared to the gas density distribution, highlighting the importance of streaming and diffusive transport in addition to advection. Near the midplane, the CR flux is somewhat turbulent. Above $z \sim 1$ kpc, however, $\mathbf{F}_c$ mostly aligns with the velocity streamlines, confirming that advection is the dominant propagation mechanism in the hot wind. In the denser neutral gas near the midplane, $\sigma_\parallel$ is small, meaning that diffusion is significant. In contrast, $\sigma_\parallel$ is relatively large in the diffuse, hot, ionized gas.

2.3.2 Choice of Perpendicular Scattering Coefficient

We model CR transport with two choices of the perpendicular scattering coefficient, $\sigma_\perp$: $\sigma_\perp = 10 \times \sigma_\parallel$ or $\sigma_\perp \gg \sigma_\parallel$ (see Section 2.2.5). In previous work considering only 1 GeV CRs, the choice of $\sigma_\perp$ did not lead to significant differences in the final CR distribution (Armillotta et al., 2021). When we consider higher energy CRs, however, we do see changes in the resulting CR distribution depending on the choice of scattering coefficient.

In Figure 2.2, we present the value of the CR mean free path, $\ell = 1/(c\sigma_\parallel)$, along with $\sigma_\parallel$ as a function of gas temperature, T. Each of the three panels represents one of our momentum bins at $E \approx pc = 2$, 13, and 101 GeV, corresponding to the lowest, middle, and highest momentum bins that we simulate. Within each panel, we compare the value of ℓ for the two definitions of $\sigma_\perp$. At low temperatures, IN is the dominant damping mechanism while at higher temperatures, $T \gtrsim 10^4$ K, NLL dominates. The transition between these two regimes is evident through a drop by more than four orders of magnitude of ℓ.

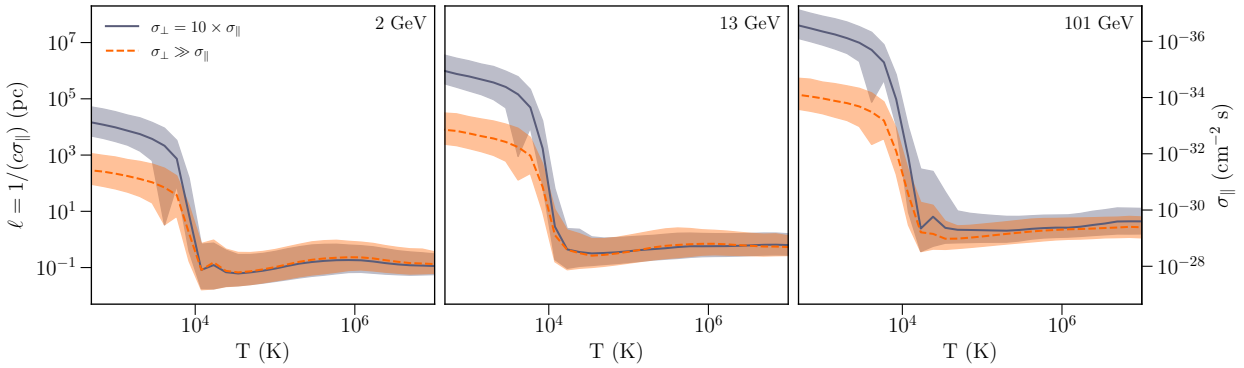

Figure 2.2: CR mean free path, $\ell = 1/(c\sigma_\parallel)$ and $\sigma_\parallel$ as a function of gas temperature, T. The lines represent the median value across all snapshots, while the shaded regions represent the 16th-84th percentiles. Each panel represents a different CR momentum bin, $pc = 2$, 13, and 101 GeV. In each bin, we include the distribution of ℓ and $\sigma_\parallel$ for both $\sigma_\perp = 10 \times \sigma_\parallel$ (gray, solid lines) and $\sigma_\perp \gg \sigma_\parallel$ (orange, dashed lines).

For $T \gtrsim 10^4$ K, ℓ is the same for either choice of $\sigma_\perp$. At these temperatures, ℓ is short so the CRs are well coupled to the gas and advection is the dominant mechanism for CR transport. If T $\lesssim 10^4$ K, however, diffusion is more important than advection. In this regime, ℓ is consistently shorter when $\sigma_\perp \gg \sigma_\parallel$. With this choice of $\sigma_\perp$, the CRs are less diffusive, and larger CR energy gradients form. This increases ∇P_c thereby increasing $\sigma_\parallel$ and further reducing the diffusivity of the CRs.

The difference in the rate of diffusion between the two choices of $\sigma_\perp$ is evident in the spatial distribution of the CRE energy spectrum, $E^2 j_e \propto e_c$ (see Equation 2.35), which we present in Figure 2.3. We compare vertical slices through the simulation box at $y = 0$ at the same energy values as in Figure 2.2 ($pc = 2$, 13, and 101 GeV). All slices are taken from the snapshot at $t = 214$ Myr.

The distribution of the lowest energy CREs is similar in each of the two cases (as in Armillotta et al. 2021). The values of $\sigma_\parallel$ and $\sigma_\perp$ are large enough in both definitions to limit significant diffusion. As energy increases, however, $\sigma_\parallel$ decreases and the value of $\sigma_\perp = 10 \times \sigma_\parallel$ becomes much smaller compared to the large, fixed value we set for $\sigma_\perp \gg \sigma_\parallel$. The difference in $\sigma_\parallel$ between the two cases also becomes larger (Figure 2.2). Therefore, there is significantly more diffusion if $\sigma_\perp = 10 \times \sigma_\parallel$ case compared to $\sigma_\perp \gg \sigma_\parallel$. In the highest momentum bin,

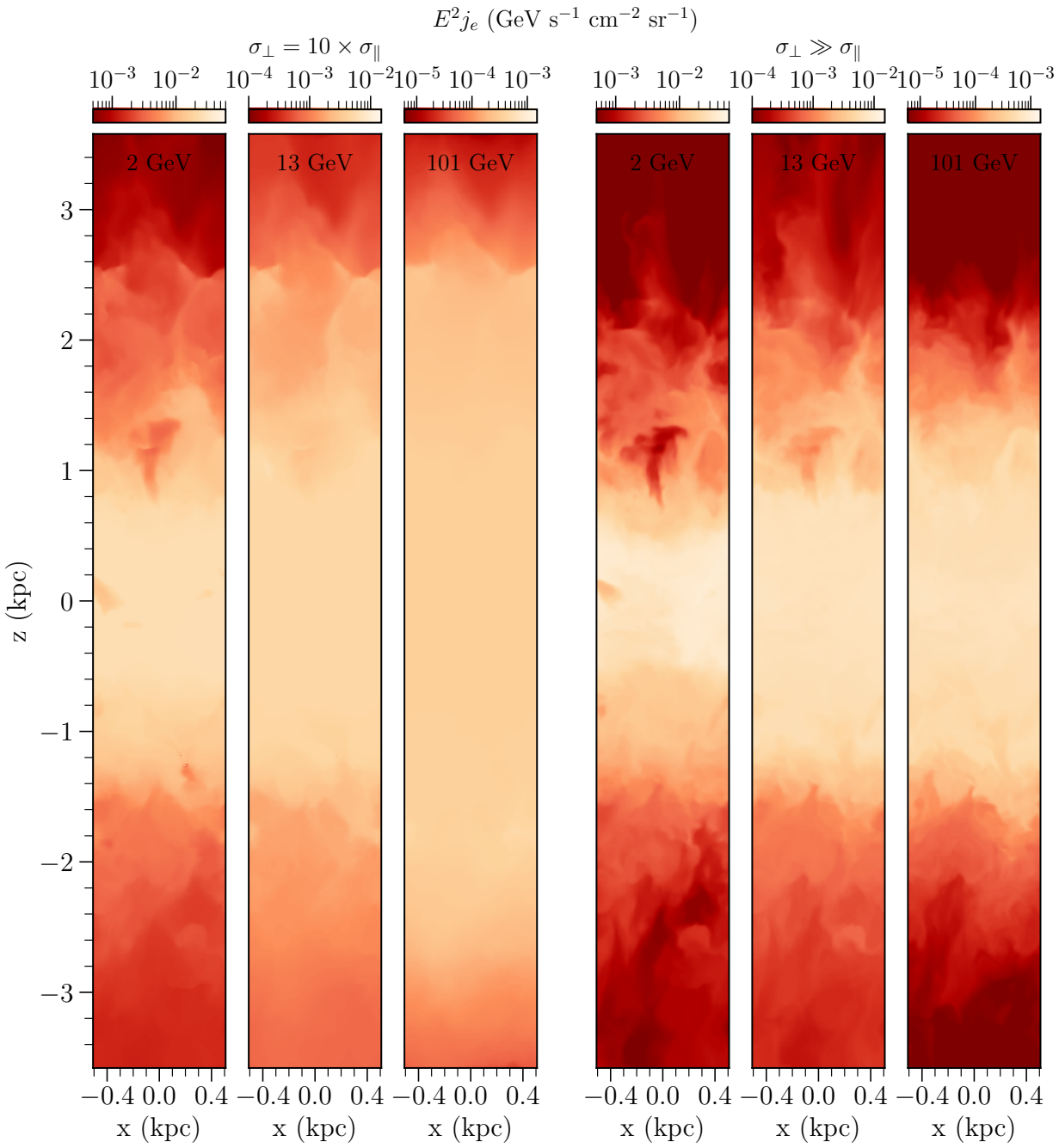

Figure 2.3: Vertical slices (through $y = 0$) of the CRE energy spectrum ($E^2 j_e$) in the bins centered at $pc = 2$, 13, and 101 GeV taken from the snapshot at $t = 214$ Myr. For each bin, we include the results for both $\sigma_\perp = 10 \times \sigma_\parallel$ (left three panels) and $\sigma_\perp \gg \sigma_\parallel$ (right three panels).

the distribution of CREs when $\sigma_\perp = 10 \times \sigma_\parallel$ is practically uniform, whereas the $\sigma_\perp \gg \sigma_\parallel$ case still shows significant structure with greater j_e near $z = 0$. This result is true across all the snapshots.

In Figure 2.4, we show horizontally averaged profiles of the CRE spectral flux j_e at different momenta as a function of z for both values of $\sigma_\perp$. The profiles are computed as follows: within each snapshot, we find the horizontally averaged value of j_e at each z, denoted as $\langle j_e \rangle$; we then determine the median and 16th-84th percentile values of $\langle j_e \rangle$ across all snapshots. For all momenta, the profiles show a smaller scale height when $\sigma_\perp \gg \sigma_\parallel$ than when $\sigma_\perp = 10 \times \sigma_\parallel$, with the difference in scale height increasing with CRE momentum. In the highest momentum bin, the CRE spectrum is practically uniform across z when $\sigma_\perp = 10 \times \sigma_\parallel$, owing to the high diffusion. Near the midplane, however, the magnitude of j_e is very similar for both $\sigma_\perp$ conditions in all bins. Therefore, we conclude that the results derived from the CR distribution near the midplane will be consistent regardless of the condition on $\sigma_\perp$.

2.3.3 Energy Losses

In CR electrons, unlike protons, the rate of energy loss is extremely important for determining the steady state CR spectrum. We show the horizontally and temporally averaged values of the CRE energy loss rate, $[dE/dt]_j$ (Equation 2.30), as a function of height for each CRE momentum bin j in Figure 2.5 (the equivalent figure for CR protons is shown in Figure 2.11). Different lines represent different loss mechanisms as described in Section 2.2.7 (and in more detail in Section 2.C): ionization, bremsstrahlung, synchrotron, and IC. As in Figure 2.4, we compute the vertical profiles by evaluating the median and 16th-84th percentile of the horizontally averaged $\langle dE/dt \rangle$ across all snapshots.

For the lowest momentum CREs, all loss rates are roughly comparable near the midplane. As CR momentum increases, however, the relative scaling of the loss mechanisms leads to IC dominating. Synchrotron losses have the same energy scaling as IC ($\propto \gamma^2$), but the magnetic

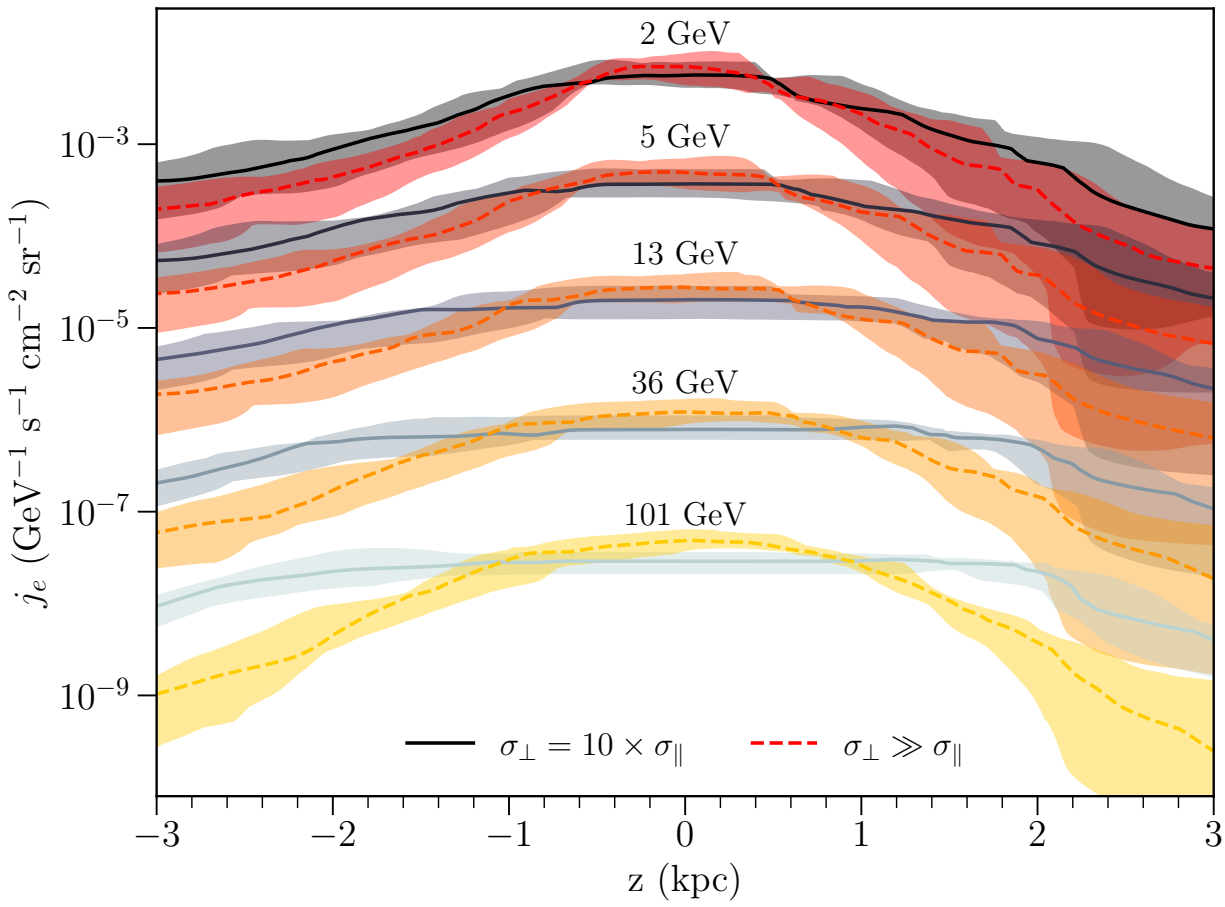

Figure 2.4: Horizontally and temporally averaged vertical profiles of the CRE spectrum, j_e, in each momentum bin. The shaded area covers the 16th and 84th percentiles from temporal variations while the central line represents the median value. The solid lines with a gray color scale represent the simulations with $\sigma_\perp = 10 \times \sigma_\parallel$. The dashed lines with a red-yellow color scale represent simulations with $\sigma_\perp \gg \sigma_\parallel$.

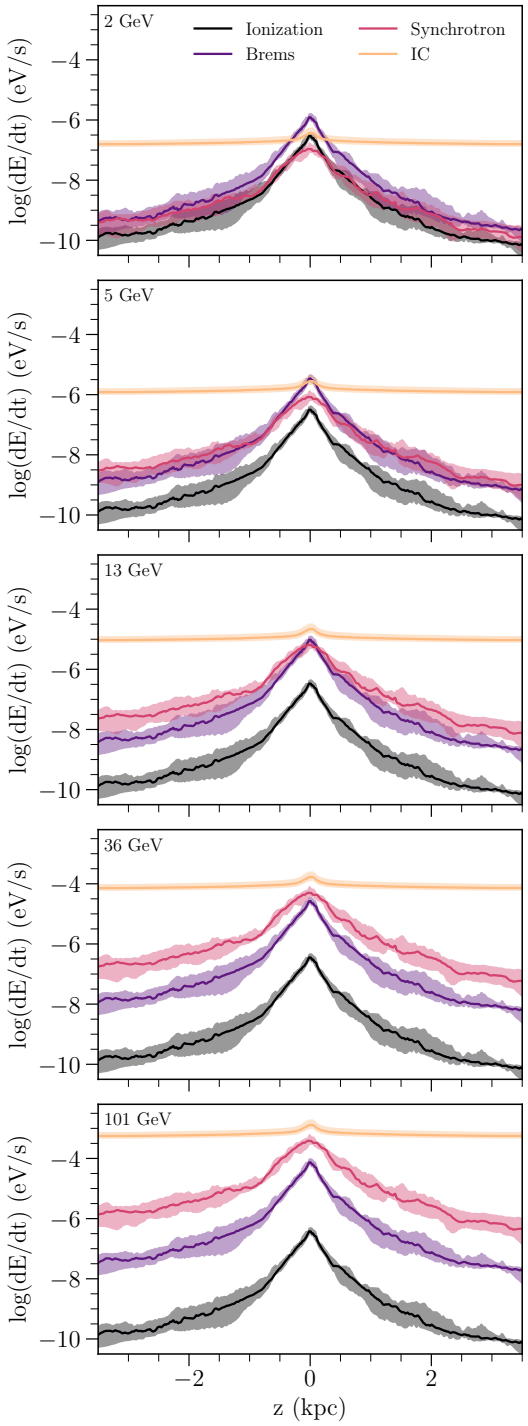

Figure 2.5: Horizontally and temporally averaged vertical profiles of CRE energy loss rates dE/dt. Different colors represent different loss mechanisms: ionization (black), bremsstrahlung (purple), synchrotron (magenta), and IC (light orange). Each panel shows results for CREs within a different momentum bin. At each z, the solid lines represent the median value of the horizontally averaged $\langle dE/dt \rangle$ evaluated across all snapshot times. The shaded regions cover the 16th-84th percentiles.

energy density is generally lower than the photon energy density in the solar-neighborhood TIGRESS simulations, so the IC losses dominate overall. Above z $\approx$ 500 pc, the IC losses dominate at all energies. IC dominates losses at large $|z|$ because the photon energy density drops off much less steeply with z than either the magnetic energy density (relevant for the synchrotron losses) or number density of the gas (important for the bremsstrahlung and ionization losses).

Using these loss rates, we define a loss timescale as

$$t_{\mathrm{loss},j}(z) = \frac{E_j}{\left[\frac{dE}{dt}\right]_j(z)}\,, \tag{2.36}$$

where the denominator includes all four loss mechanisms. This is an approximation for the time it would take a CRE at height z to lose all of its energy. It does not account for the fact that dE/dt would change as the CRE loses energy, or that the CRE can propagate in space.

We compare this loss timescale to an estimate of the transport time defined as

$$t_{\mathrm{transport},j}(z) = H_{\mathrm{gas}}\frac{4}{3}\frac{\langle e_{\mathrm{c},j}(z)\rangle}{\langle |F_{\mathrm{c},z,j}(z)|\rangle}\,, \tag{2.37}$$

which represents the average time it takes for a CRE to traverse the scale height of the gas. The ratio $\frac{4}{3}\langle e_{\mathrm{c},j}(z)\rangle/\langle |F_{\mathrm{c},z,j}(z)|\rangle$ is the inverse of the effective mean vertical propagation speed, $v_{\mathrm{eff,z,j}}$, with $\langle e_{\mathrm{c},j}\rangle$ and $\langle |F_{\mathrm{c},z,j}(z)|\rangle$ the horizontally averaged CR energy density and vertical component of the CR flux respectively. H_{gas} is the scale height of the horizontally averaged gas density. If we wanted to estimate the total CR transport time out of the galaxy, we would need to multiply this expression by a factor of $H_{\mathrm{c}}/H_{\mathrm{gas}}$, where H_{c} is the CR scale height.

The transport time is most limited by downstream regions (at larger $|z|$) where $v_{\mathrm{eff,z,j}}$, due to the combination of advection, streaming, and diffusion, is smallest. Figure 2.1 shows that the scattering coefficient $\sigma_{\parallel}$ is quite small in most of the midplane region (where the

gas is mostly neutral), becoming large only at $|z| \gtrsim 0.5$ kpc. Because all CRs have to pass through the high-scattering region at $|z| \gtrsim 0.5$ kpc in order to escape from the box, this limits the net vertical flux and hence $v_{\rm c,eff,z}$ in the "upstream" region near the midplane as well, even though the scattering rate is small there so that the CRs are highly diffusive.

Thus, it is also useful to consider the diffusion time

$$t_{{\rm diff},j}(z) = H_{\rm gas}\frac{4}{3}\frac{\langle e_{{\rm c},j}(z)\rangle}{\langle |F_{{\rm diff},z,j}(z)|\rangle}\,, \tag{2.38}$$

where $\langle |F_{{\rm diff},z,j}|\rangle$ is the horizontal average of the diffusive flux in the vertical direction, i.e. $|\overleftrightarrow{\sigma}_j^{-1}\cdot\hat{z}\partial P_c/\partial z|$. This is the time it would take a cosmic ray to traverse the scale length of the gas considering only diffusion. Previously, Armillotta et al. (2024) (see Eq. 16 and Fig. 8 of that paper) showed that the diffusion speed for GeV CRs in the majority of the neutral gas near the midplane is $\sim 10^2$ km s^{-1}, which with $H_{\rm gas} = 300$ pc would imply a diffusion time of a few Myr. Since higher energy CRs have even lower scattering rate, we would expect their diffusion timescales to be even lower.

We show a comparison of the loss time with the transport and diffusion timescales for CRs in each momentum bin in Figure 2.6. The loss timescale is minimized at the midplane where the loss rates are greatest (Figure 2.5). At larger z, this timescale is roughly constant with z due to constant IC losses. As CRE momentum increases, energetic losses increase dramatically, so the timescale shortens correspondingly. For the highest momentum CRs, the loss timescale is only a few Myr at $z = 0$.

Unlike the loss timescale, the transport time is maximized at $z = 0$ and decreases as $|z|$ increases due to the increasing value of the advection speed of the gas (see Figure 2.1). As CR momentum increases, the transport time decreases slightly because, unlike the advection and streaming velocities which are momentum-independent, the diffusion velocity increases with CR momentum. The decrease in transport time at higher energy means that even in the absence of losses, the actual CR spectrum would be steeper than the injection spectrum.

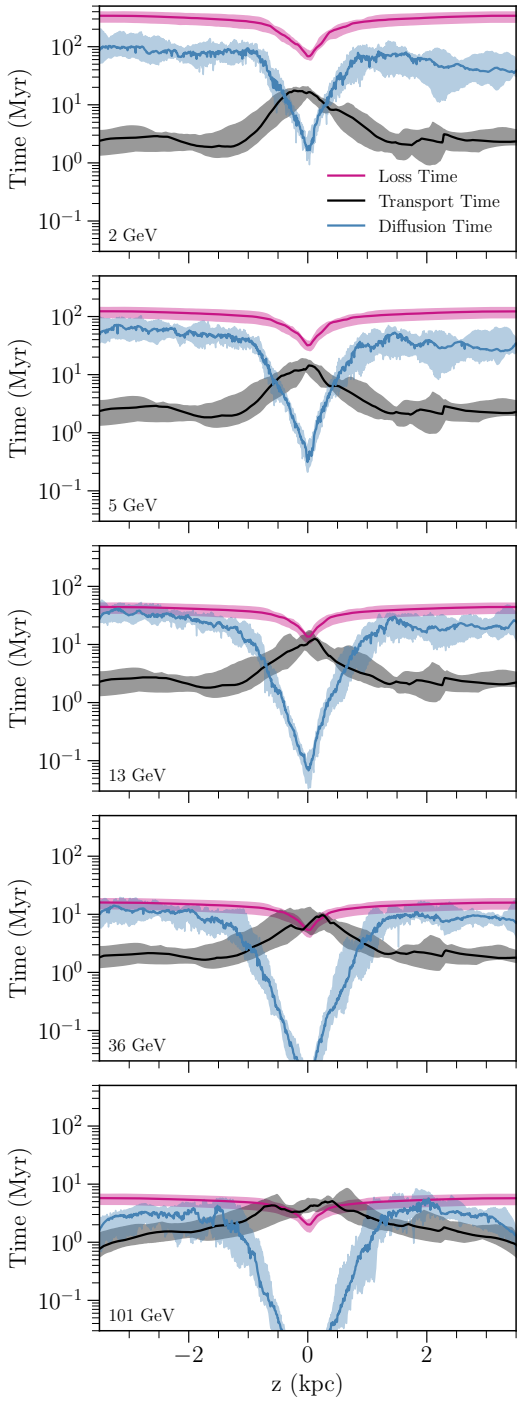

Figure 2.6: Horizontally and temporally averaged vertical profiles of the timescale for energy loss (magenta) in comparison to transport (black) and diffusion (blue). These timescales are defined in Equation 2.36, Equation 2.37, and Equation 2.38, respectively. Each panel presents results for CREs within a given momentum bin. At each z, the solid line represents the median value of the horizontally averaged $\langle t \rangle$ evaluated across all snapshots. The shaded regions show the 16-84th percentile values across all snapshots.

For the lowest momentum CREs, the transport time is faster than the loss timescale at all z. At higher momentum, however, the loss timescale decreases such that it is comparable to the transport time near the midplane for the three highest momentum bins. We conclude that it is a combination of both the energy dependent losses and the reduction in transport time with increasing CRE energy that drives the steepening of the electron spectrum compared to the injected spectrum (see Section 2.3.4).

Near the midplane, the CRE distribution is highly uniform, as seen in Figure 2.3 and Figure 2.4. This indicates that diffusion may be a dominant process in this region, and indeed Armillotta et al. (2024) showed quantitatively that for GeV protons, diffusion is the dominant transport mechanism in the warm/cold neutral medium found near the midplane. Figure 2.6 shows that the local diffusion time in the midplane region is significantly lower than the transport and loss timescales for the CREs in all momentum bins. As discussed above, even though CRs easily diffuse along field lines in the neutral midplane region (leading to a short local transport time), the net flux out of the box is limited by the much higher scattering rate at large $|z|$ where gas is ionized. This means that CRs effectively transverse the midplane region many times before they are able to escape from the disk.

2.3.4 CR Spectrum

We compare the simulated CRE spectrum to the directly observed, solar neighborhood values in Figure 2.7. To best recreate typical conditions representative of the ISM we use only the warm gas ($T < 3\times10^4$ K) in the disk region ($|z| < 300$ pc). The limit on temperature removes the hot gas surrounding the injection regions (e.g. Redfield & Linsky, 2004), but does not significantly change the results. We limit our comparison to the midplane region of the simulation both to mimic solar neighborhood conditions, and because our post-processing simulations do not necessarily reproduce accurate ISM conditions at larger z (where CR pressure gradients may transfer momentum to the gas, accelerating it, see Section 2.2.2)

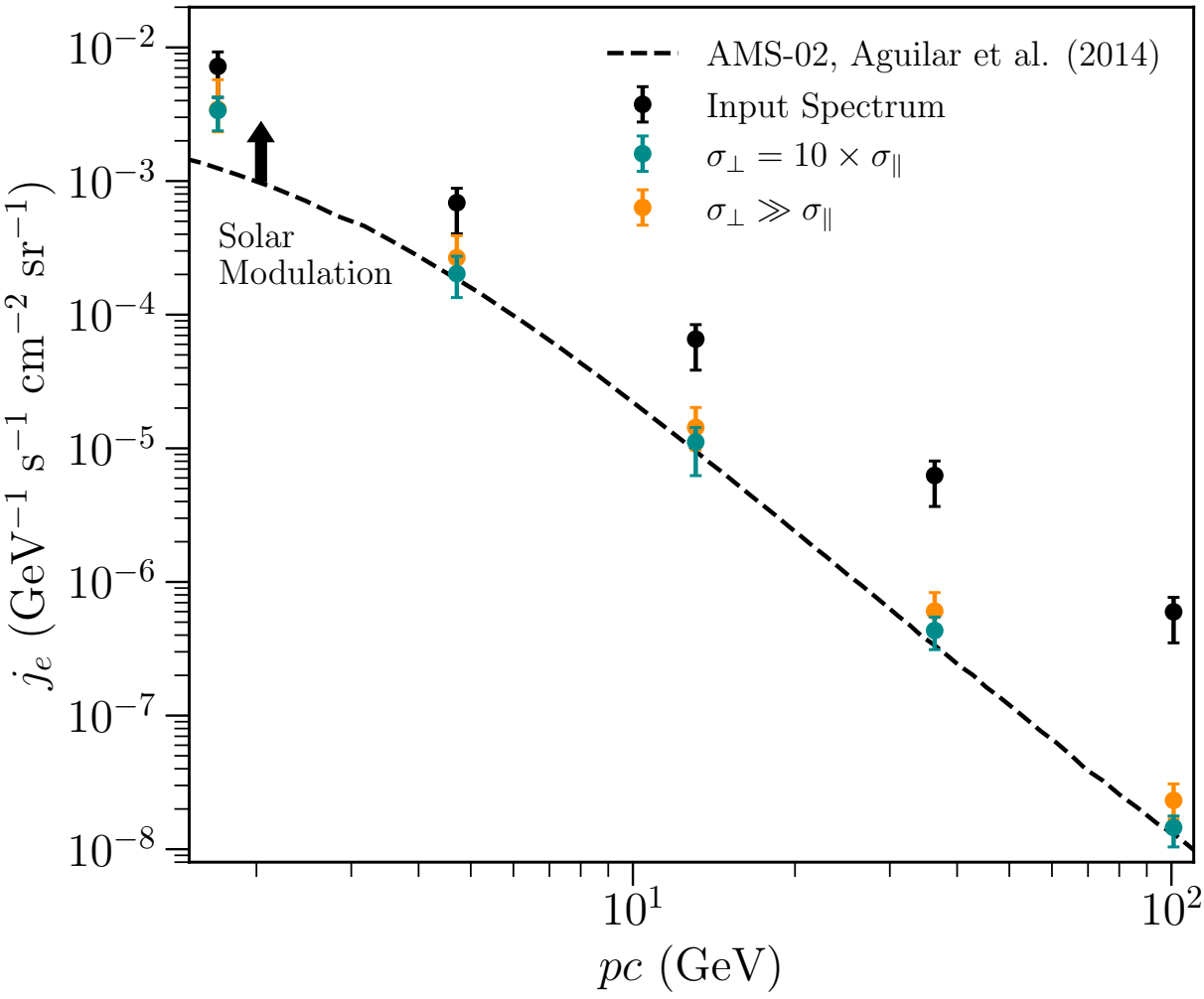

Figure 2.7: Spatially and temporally averaged CRE spectrum in the warm gas ($T < 3{\times}10^4$ K) within the disk region ($|z| < 300$ pc). The points represent the median value across space and time, while the error bars show the 16th-84th percentiles. The black points represent the input spectrum with a fixed power-law slope of $s = -2.3$. The blue and orange points represent the final CRE spectra for the two different conditions for $\sigma_\perp$. The normalization of the CRE spectrum has been reduced by a factor of two to more closely match the observed values from AMS shown in the black dashed line (Aguilar et al., 2014).

Figure 2.7 includes the input CR spectrum as a function of $E \approx pc$, as well as the final, evolved spectra in both $\sigma_\perp$ cases. These values are averaged both spatially and across all snapshots (different snapshots have different SN rates and hence different CR injection rates and input spectra). Each point represents the median value, and the error bars are the 16th-84th percentile values. The spectra for $\sigma_\perp = 10 \times \sigma_\parallel$ and $\sigma_\perp \gg \sigma_\parallel$ are very similar, with the former slightly steeper than the latter. Indeed, as noted in Section 2.3.2, the spectra are weakly dependent on the choice of $\sigma_\perp$ near the midplane. The final spectra are steeper than the initial spectrum due to the energy-dependent transport and, more significantly, the energy-dependent losses that CREs experience as they propagate through the ISM (see Section 2.3.3).

Along with the three simulated spectra, in Figure 2.7, we include direct observations of the CRE spectrum by AMS-02 (Aguilar et al., 2014). To more closely match the observed values, we have rescaled the simulated spectra (including the input spectra) across all bins, reducing the magnitude by a factor of two. As discussed in Section 2.2.4, the spectrum can be renormalized freely after the CR evolution to reflect a different initial normalization.

Although the normalization of the simulated CRE spectrum overestimates the observed value, the ratio to the simulated CR proton spectra is consistent with observations. We find the simulated proton spectra to also overestimate the observed values by a factor of two but reproduce the observed spectral slope well (see Figure 2.13, presented in more detail in Armillotta et al. (2025)). Therefore, the adopted choice of a 2% injection efficiency of electrons relative to protons is consistent with direct observations. The overestimation of the total CR energy density might be explained by an enhanced star formation rate (SFR) in the TIGRESS simulations ($\Sigma_{\rm SFR} \sim 5 \times 10^{-3}$ M$_\odot$ kpc^{-2} yr^{-1}) compared to the mean solar neighborhood value over the last 100 Myr ($2 \times 10^{-3} \lesssim \Sigma_{\rm SFR} \lesssim 5 \times 10^{-3}$ M$_\odot$ kpc^{-2} yr^{-1}) (Zari et al., 2023), which is the period when the CRs we observe today were generated. Alternatively, if the SFR and SN rate in the Solar neighborhood are in agreement with the TIGRESS level, it would imply that the total energy injection per SN at $p_{\rm min} > 1$ GeV/c

would need to be reduced by a factor two relative to our assumptions, i.e. becoming 5×10^{49} erg for CR protons, and 10^{48} erg for CR electrons.

The renormalized CRE spectrum matches the observations extremely well, especially in the four highest momentum bins. The lowest simulated momentum bin, however, has a larger magnitude than the observations. At energies below a few GeV, the AMS observations are affected by solar modulation such that the directly observed CR spectrum is reduced. This effect is also seen in other models of the CRE spectrum (e.g. Padovani et al., 2018; Werhahn et al., 2021b).

In Figure 2.8, we show the slope of the CRE spectrum as a function of energy. Assuming that the spectrum between two consecutive bins can be approximated by a power law, we define the spectral slope as

$$s = \frac{d\log\, j_e}{d\log\, E} \approx \frac{\log(j_{e,1}/j_{e,2})}{\log(E_1/E_2)} \tag{2.39}$$

where the subscripts represent consecutive CR bins.

The solid, horizontal lines in Figure 2.8 represent the median slope across all cells with $|z| < 300$ pc and $T < 3 \times 10^4$ from all snapshots. The shaded regions show the 16th-84th percentiles. We also include two lines representing models fit to the observed CRE spectrum from Orlando (2018) and Padovani et al. (2018). Orlando (2018) use a CR propagation model to fit a combination of gamma-ray and radio emission along with direct CR observations. Padovani et al. (2018) use a multi-parameter fit to best match the direct observations from a combination of AMS and Voyager results. We see agreement between our simulations and these empirically-fit models in all energy bins.

The CRE spectrum steepens with increasing energy due to changes in the dominant energy loss mechanisms and their varying dependence on CRE energy. As discussed in Section 2.3.3, the contribution of synchrotron and IC increases with E, while Bremsstrahlung and ionization losses become less important. The former mechanisms have a stronger energy dependence ($\propto \gamma^2$) than the latter ($\propto \gamma \ln\gamma$ or $\ln\gamma$), which explains why the spectrum steepens at higher energies. The energy-dependent diffusion rate also contributes to steepening

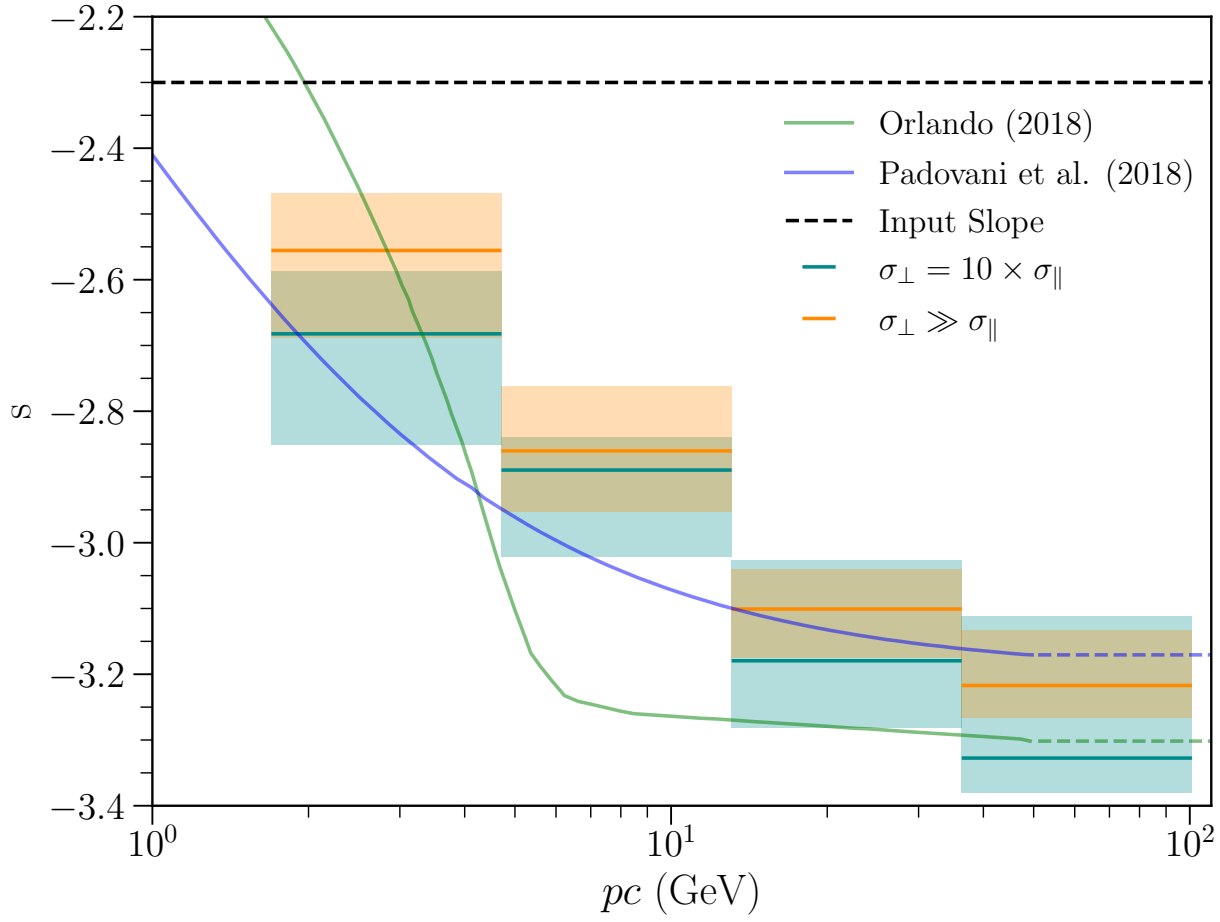

Figure 2.8: Power-law slope of the CRE spectrum (Figure 2.7) as a function of CR momentum. The slope is calculated across neighboring bins as in Equation 2.39. The solid horizontal lines represent the median value of the slope across all cells with $|z| < 300$ pc and $T < 3 \times 10^4$ from all snapshots. The shaded region shows the 16th-84th percentiles. The two colors represent the two conditions for $\sigma_\perp$. The green and purple lines are reproduced from Padovani et al. (2021) and represent the values of s estimated from a combination of direct observations and modeling as detailed in Orlando (2018) and Padovani et al. (2018) respectively. We have extrapolated the observed values at high energy using a constant slope for the sake of comparison (shown in the dashed lines). The black dashed line represents the input slope.

of the CRE spectrum. If advection and Alfvénic streaming were the dominant transport mechanism, we would not see any change in the spectral slope from the injected value where losses are negligible. This effect is more obvious in the proton spectrum where the energy loss mechanisms are not significant, and diffusion alone is responsible for energy-dependent steepening (Figure 2.14, presented in more detail in Armillotta et al. (2025)).

To determine the effect of the injection slope on the final CRE spectrum, we simulate the transport of CRs within the TIGRESS snapshot at $t = 214$ Myr using three different slopes of the injected distribution function: $\gamma_{\rm inj} = 4.2$, 4.3 (our fiducial value), and 4.4. These correspond to CRE spectral slopes: $s_{\rm inj} = -2.2$, -2.3, and -2.4. The evolved CR spectral slopes as a function of momentum from each model are shown in Figure 2.9. This figure includes both the final value of s (as in Figure 2.8), along with the change in slope, Δs, from the injected value.

We find that the change in slope, Δs, does not vary significantly when the injection slope is modified. As noted in Section 2.2.4, the CR energy density (Equation 2.1) is roughly linearly proportional to the injected spectrum except through effects from $\sigma_{\rm tot}$. Therefore, the final slope could be simply rescaled to a different choice of injection slope. Based on our physical result that Δs varies with CRE momentum from -0.4 at 2 GeV to -1.2 at 100 GeV, we conclude that an injection slope of $s = -2.3$ is needed for a good match to the observed spectrum.

2.4 Discussion

Although many studies have simulated CR transport on galactic scales, only a limited number have modeled spectrally resolved CREs. As the total energy density of CREs is negligible compared to that of protons, they are not generally included in MHD simulations only concerned with the effects of CRs on ISM dynamics and galactic wind driving. CREs,

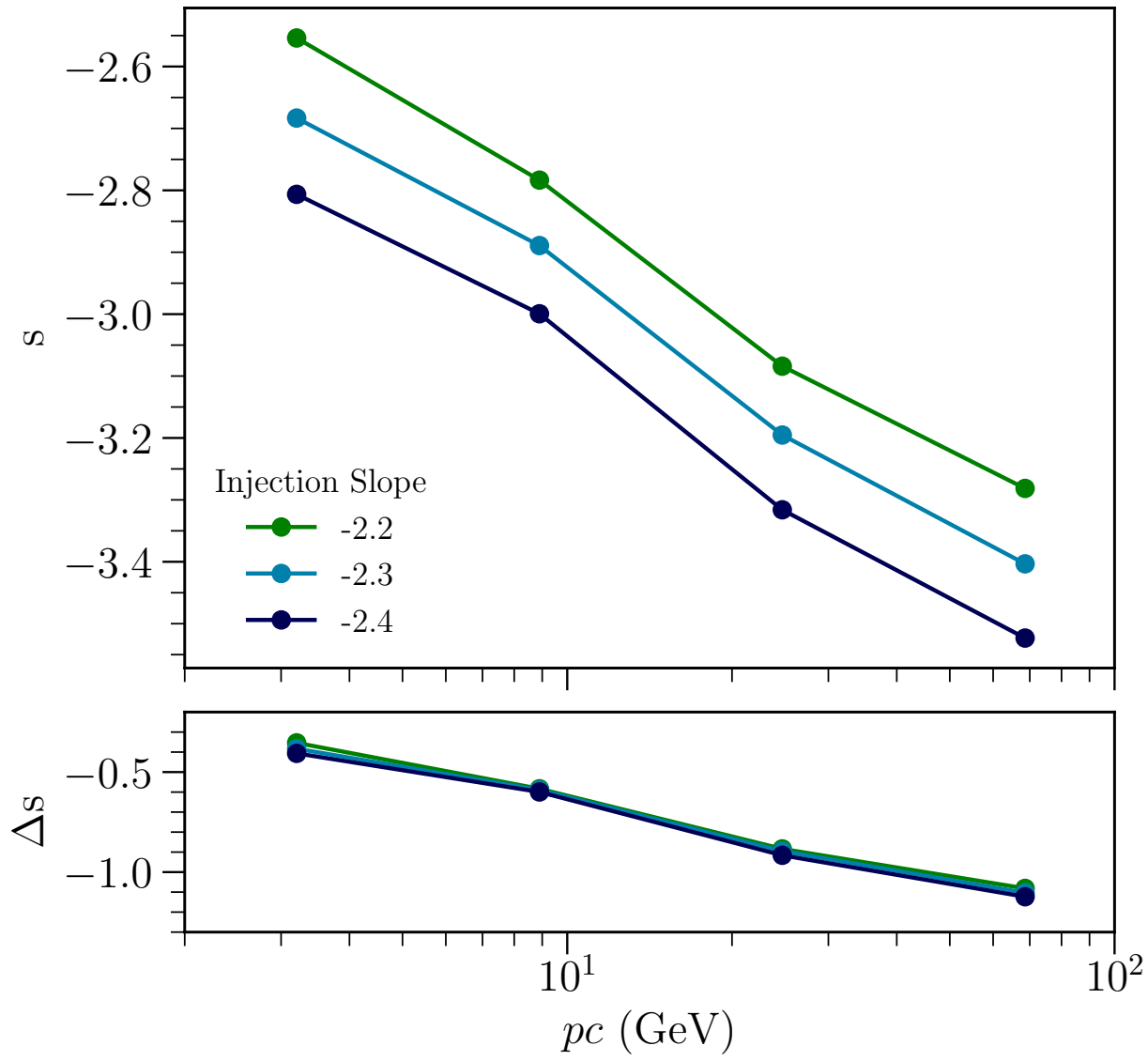

Figure 2.9: Power-law slope of the CRE spectrum (Equation 2.39) as a function of momentum for three choices of the injection spectrum. The points represent the median value across all cells with $|z| < 300$ pc and $T < 3 \times 10^4$ K. The lower panel shows the change in slope from the injected value.

however, represent a powerful observable, and simulating their transport on galactic scales is crucial to enable comparisons with observations (see Chapter 3).

To date, other studies that have modeled the transport of spectrally resolved CREs in ISM/galaxy simulations include those by Werhahn et al. (2021a,b) and Hopkins et al. (2022a,b). Werhahn et al. (2021a,b) model the transport of both protons and electrons in simulations of isolated Milky Way-like galaxies. These simulations have a mass resolution of $1.6 \times 10^{2-4}$ $M_\odot$ corresponding to a spatial resolution of approximately 20-90 pc at a number density of 1 cm^{-3}. They first run simulations where single-energy GeV CR protons evolve along with the background gas. These simulations treat CR transport in terms of advection and diffusion, while neglecting streaming, which we find to be an important transport process in the warm, ionized gas, where both advection and diffusion are limited (Armillotta et al., 2024; Armillotta et al., 2025). After self-consistently evolving GeV protons and MHD, they post-process their simulations to compute the distribution of spectrally resolved CR protons and electrons. To do so, in each computational cell, they solve the Fokker-Planck equation for the proton and electron distribution functions, assuming steady state, and neglecting streaming transport and adiabatic losses. Diffusion is parametrized by a spatially constant, energy-dependent diffusion coefficient based on observational constraints, $D = 10^{28}(E/3$ $GeV)^{0.5}$ cm^2 s^{-1} (see Evoli et al., 2020b). For the electrons, they account for energetic loss mechanisms such as synchrotron and IC. With this method, Werhahn et al. (2021a,b) are able to reproduce the observed CR proton and electron spectra at a Galactocentric radius of $\simeq 8$ kpc.

The work by Hopkins et al. (2022a) models energy-dependent transport of CREs, along with many other species, in cosmological zoom-in simulations. These models have a mass resolution of $\sim 10^4$ $M_\odot$ corresponding to a spatial resolution of approximately 75 pc at a number density of 1 cm^{-3} (Chan et al., 2019; Hopkins et al., 2020). As in our model, they include CR transport via advection, diffusion, and streaming, as well as various energetic loss mechanisms, although they evolve the CR species self-consistently along with the back-

ground gas. Unlike our model, they also consider multiple methods of CR re-acceleration. Additionally, they employ a diffusion parameter that is dependent only on CR energy with $D \propto 10^{29}(R/1\ \mathrm{GV})^{0.5}\ \mathrm{cm}^2\ \mathrm{s}^{-1}$, where $R = pc/q$ is the particle rigidity. The normalization of the diffusion coefficient is calibrated to reproduce observed spectra. We note that this diffusion coefficient is more than an order of magnitude higher than the value employed by Werhahn et al. (2021a,b). With this model, Hopkins et al. (2022a) reproduce the observed CRE spectrum, along with the spectra of the CR protons and other heavier species.

In a subsequent work, Hopkins et al. (2022b) go beyond the assumption of spatially constant diffusion, and test a transport model with variable diffusion coefficient based on the predictions of the self-confinement scenario. With this model, however, they do not reproduce the observed CRE spectrum. A variety of reasons may contribute to the fact that the self-confinement model of Hopkins et al. (2022b) does not reproduce the observed CR spectrum, while our self-confinement model does. As discussed in Armillotta et al. (2021) and Armillotta et al. (2024), there are differences in the details of the CR implementation, as well as orders of magnitude difference in the mass resolution for hot gas.

It is encouraging, therefore, that our post-processing simulations using the self-confinement model are able to reproduce the observed CRE spectrum despite the simplifying assumptions made in the implementation of CR transport. We find that energy-dependent losses, in combination with energy-dependent CR diffusion using self-consistently determined scattering coefficients, and streaming and advection that are energy-independent (but strongly dependent on local multiphase gas properties), leads to energy-dependent steepening of the CRE spectrum. The CRE spectral slope obtained from our simulations is in good agreement with direct observations in the solar neighborhood. The factor of two enhancement of the total CR energy density in our simulations compared to solar neighborhood observations could be attributed to a different energy injection rate per SN, or a difference in the SFR between the simulations and the Milky Way.

2.5 Summary

We have extended the model of CR transport presented in Armillotta et al. (2021) to include spectrally resolved CR protons and electrons between 1-100 GeV. This is done by post-processing TIGRESS simulations of the multiphase ISM which include accurate thermal structure, magnetic fields, and gas dynamics (Kim & Ostriker, 2017), all of which are critical for CR transport. In particular, knowledge of local gas properties is necessary for determining the local rate of diffusion of the CRs, which is quite sensitive to the ionization state of gas since damping of small-scale magnetic fluctuations is very rapid in neutral gas. Working within the self-confinement framework for CR transport, we self-consistently determine the scattering coefficient as a function of local gas and CR properties, based on the balance of streaming-driven Alfvén wave growth and regime-specific wave damping.

To model the evolution of the CRE spectrum accurately, we also include energy dependent losses. Through a combination of these losses and transport mediated by the self-consistently determined scattering coefficient, we see evolution of the CRE spectrum that is consistent with direct observations. Our results are robust to the choice of the perpendicular scattering rate and the initial CRE spectrum. We also find the simulated CR proton spectrum to be consistent with direct observations (Section 2.D, Armillotta et al. (2025)). For protons, losses are negligible so the final spectrum is determined primarily by the energy-dependent diffusion rate. To our knowledge, this represents the first model that both implements a scattering rate determined using the self-confinement model and reproduces the observed CR spectrum. A caveat, however, is that we have adopted a simplified post-processing model with independent CR momentum bins. It will therefore be valuable in the future to revisit this spectral analysis in a fully self-consistent model with live MHD evolution. A discussion of future work is included in Chapter 5.

In this chapter we limit ourselves to solar neighborhood models of the ISM as a proof of concept, and also because for this environment we can compare to direct CRE observations. The transport model can, however, be applied to TIGRESS simulations representing

many different galactic environments (as in Armillotta et al., 2022) to explore how the CRE spectrum may respond to environmental conditions in various regimes. We will consider an inner galaxy environment in Chapter 4.

2.A Effects of MHD Relaxation

In Section 2.2.2, we describe our two stage method for modeling CR transport. First, we evolve the CRs to a steady state while the MHD is frozen. Then, we allow for a brief period of MHD relaxation in which the gas can react to the presence of CRs. This short relaxation step reduces the unphysically large CR pressure gradients that form during the first post-processing stage.

The MHD relaxation step, because of its short duration, only has relatively local effects. We find that while the spatial distribution of the CRs becomes smoother, neither the vertical CRE profile nor the CRE spectrum change significantly after the relaxation step, as shown in Figure 2.10. We can see the overall normalization of the CRE spectrum decreases slightly after MHD relaxation. However, the shape of the vertical CRE profile and the CRE spectral slope are consistent before and after the live MHD stage.

2.B Proton Losses

2.B.1 Pion Production

For CR protons with kinetic energies above ~ 1 GeV, the primary energy loss mechanism is pion production caused by elastic collisions with the surrounding atoms. Considering only interactions with hydrogen, the rate of energy loss due to pion production is given by Krakau & Schlickeiser (2015) to be

$$\frac{dE}{dt} = 3.85 \times 10^{-16} n_{\rm H} \left(\frac{E}{\rm GeV} \right)^{1.28} \left(\frac{E}{\rm GeV} + 200 \right)^{-0.2} \ {\rm GeV \ s^{-1}} \tag{2.40}$$

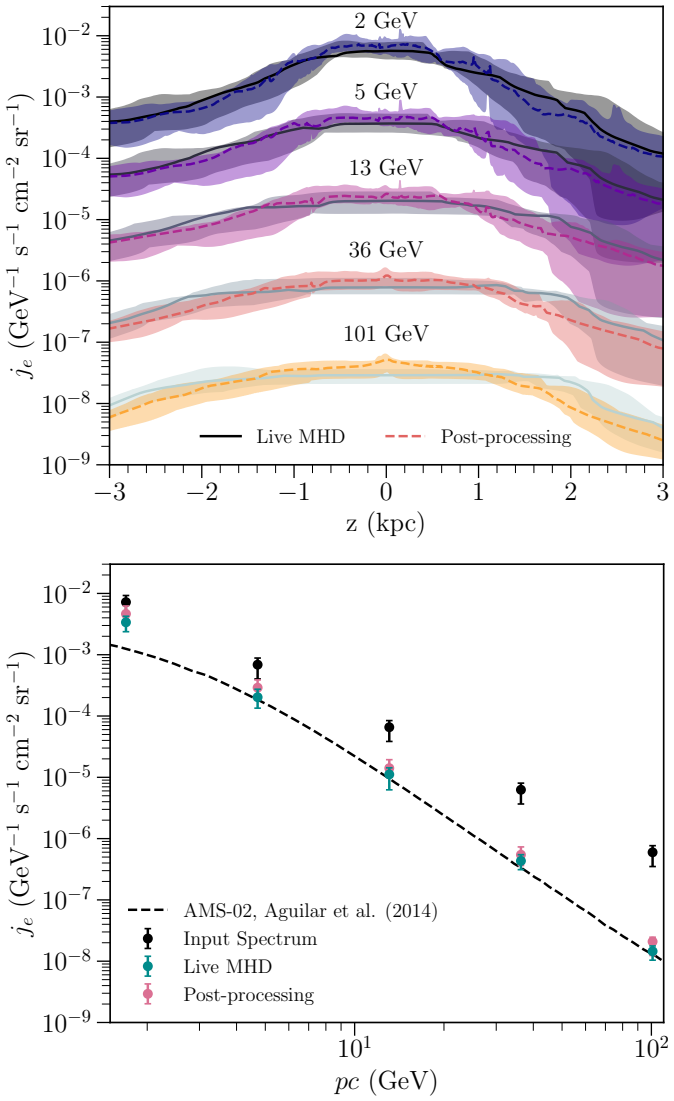

Figure 2.10: Comparisons of the CRE vertical profile and spectrum before and after live MHD relaxation. The upper panel is analogous to Figure 2.4 and shows the horizontally and temporally averaged vertical profiles of the CRE spectrum, j_e, in each momentum bin. The shaded area covers the 16th and 84th percentiles from temporal variations while the central line represents the median value. The solid lines with a gray color scale represent the simulations after live MHD relaxation. The dashed lines with a purple color scale represent simulations with only CR post-processing, i.e. prior to the MHD relaxation step. The lower panel is analogous to Figure 2.7 and shows the spatially and temporally averaged value of j_e in the warm gas ($T < 3 \times 10^4$ K) within the disk region ($|z| < 300$ pc). The points represent the median value across space and time, while the error bars show the 16th-84th percentiles. The blue and pink points represent the final CRE spectra with and without live MHD relaxation respectively. As in Figure 2.7, we include the input spectrum as black points, and reduce the normalization of all of the CRE spectra by a factor of two to more closely match the observed values from AMS (Aguilar et al., 2014). All simulation snapshots have $\sigma_\perp = 10 \times \sigma_\parallel$.

This energy loss rate is valid for kinetic energies greater than ~ 10 GeV where $E \approx E_k$. To extrapolate to lower kinetic energies, we define a continuous function with a constant slope below $E_k = 10$ GeV (Padovani priv. comm.)

$$\frac{dE}{dt} = \begin{cases} 3.85 \times 10^{-16} n_{\rm H} \left(\frac{E}{\rm GeV}\right)^{1.28} \left(\frac{E}{\rm GeV} + 200\right)^{-0.2} \text{ GeV s}^{-1} & \text{if } E_k > 10 \text{ GeV} \\ \frac{dE}{dt}(E_k = 10 \text{ GeV}) \left(\frac{E_k}{10 \text{ GeV}}\right)^{1.28} \text{ GeV s}^{-1} & \text{if } E_k < 10 \text{ GeV} \end{cases} \tag{2.41}$$

The rate of energy loss is greater if we consider atoms other than hydrogen. If we assume the local ISM has a solar composition, we must multiply the energy loss by a factor of $\epsilon = 1.18$ (Padovani et al., 2020). Writing the energy loss in terms of Λ rather than dE/dt, we find

$$\Lambda_{pion} = 1.18 \times \begin{cases} 3.85 \times 10^{-16} \left(\frac{E}{\rm GeV}\right)^{0.28} \left(\frac{E}{\rm GeV} + 200\right)^{-0.2} \text{ cm}^3 \text{ s}^{-1} & \text{if } E_k > 10 \text{ GeV} \\ 2.82 \times 10^{-15} \frac{1}{E/\rm GeV} \left(\frac{E_k}{10 \text{ GeV}}\right)^{1.28} \text{ cm}^3 \text{ s}^{-1} & \text{if } E_k < 10 \text{ GeV} \end{cases} \tag{2.42}$$

2.B.2 Ionization

At $E_k \sim 1$ GeV, the dominant loss mechanism for CRs in the neutral ISM is ionization of neutral hydrogen. The loss function is given by the Bethe-Bloch formula,

$$L_{p,H}^{ion}(E) = \frac{4\pi e^4}{m_e v^2} \left(\ln\left(\frac{2 m_e v^2}{E_{ion}(1-\beta^2)} \right) - \beta^2 \right) \text{ erg cm}^2 \tag{2.43}$$

(e.g. Draine, 2011). $E_{\rm ion}$ is the ionization energy of hydrogen, 13.6 eV, and $\beta = v/c$. The energy loss rate is then given by

$$\frac{dE}{dt} = v x_{\rm n} n_H L_{p,H}^{ion} \tag{2.44}$$

where we use the definition of the neutral number density given in Section 2.2.6. We again account for the solar composition by applying a multiplicative factor, $\epsilon = 1.1$ (Padovani

et al., 2020). Therefore, the total loss through ionization is given by

$$\Lambda_{ion} = 1.1 \frac{x_{\rm n}}{E} \frac{4\pi e^4}{m_e v} \left(\ln\left(\frac{2 m_e v^2}{E_{ion}(1-\beta^2)} \right) - \beta^2 \right) \text{ cm}^3 \text{ s}^{-1} \tag{2.45}$$

2.B.3 Coulomb

In ionized medium, the low energy CR protons primarily lose energy through Coulomb interactions. As in Werhahn et al. (2021b), this loss is given by Gould (1972) to be

$$\frac{dE}{dt} = \frac{3\sigma_T n_e m_e c^3}{2\beta} \left(\ln\left(\frac{2\gamma m_e c^2 \beta^2}{\hbar \omega_{pl}} \right) - \frac{\beta^2}{2} \right) \text{ erg s}^{-1} \tag{2.46}$$

where the plasma frequency, ω_{pl}, is given by

$$\omega_{pl} = \sqrt{\frac{4\pi e^2 n_e}{m_e}} = \sqrt{\frac{4\pi e^2 x_e n_H}{m_e}} \tag{2.47}$$

and $\sigma_T = 6.65 \times 10^{-25}$ cm^2 is the Thomson cross-section. This gives a final value of,

$$\begin{aligned} \Lambda_{coul} &= \frac{x_e}{E} \frac{3\sigma_T m_e c^3}{2\beta} \left(\ln\left(\frac{2\gamma m_e c^2 \beta^2}{\hbar \omega} \right) - \frac{\beta^2}{2} \right) \text{ cm}^3 \text{ s}^{-1} \\ &= \frac{x_e}{E} \frac{4\pi e^4}{m_e v} \left(\ln\left(\frac{2\gamma m_e v^2}{\hbar \omega} \right) - \frac{\beta^2}{2} \right) \text{ cm}^3 \text{ s}^{-1} \end{aligned} \tag{2.48}$$

2.B.4 Energetic Loss Profiles

We present the the horizontally and temporally averaged values of the CR proton energy loss rate in Figure 2.11 as was done for CREs in Figure 2.5. The solid lines represent losses due to ionization, Coulomb interactions, and pion production, as described in the previous sections. The shaded areas span the 16th-84th percentiles across the different snapshots of the horizontally averaged $\langle dE/dt \rangle$.

In the lowest momentum bin, the ionization and pion production losses are similar, while the losses due to Coulomb interactions are less significant. As momentum increases, the

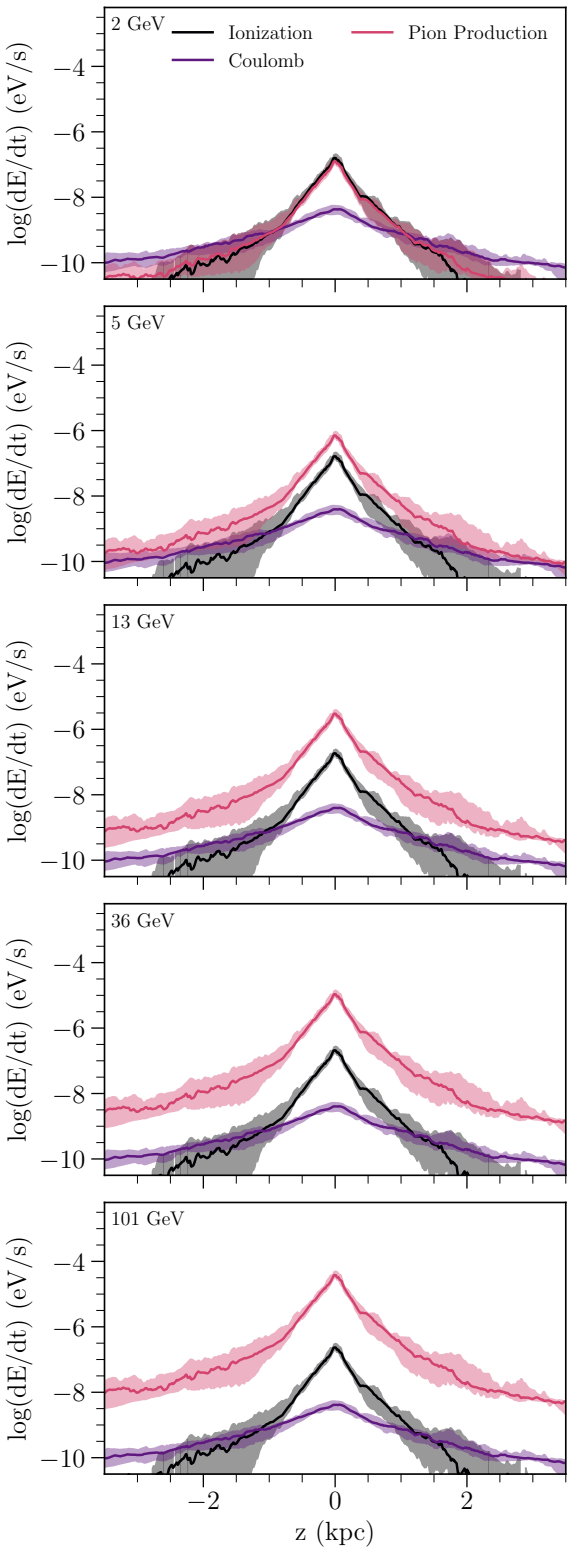

Figure 2.11: Same as Figure 2.5 but for CR proton energetic loss mechanisms. The different colors now represent losses due to ionization (black), Coulomb (purple), and pion production (magenta).

energy loss rate due to pion production increases by approximately two orders of magnitude while the ionization and Coulomb losses barely change due to the relative scalings of dE/dt with CR energy. These energetic losses are less significant than those for the CREs.

2.C Electron Losses

2.C.1 Synchrotron

CREs experience energy loss via interactions with the local magnetic field by emitting synchrotron radiation. The energy loss rate for one electron is

$$\frac{dE}{dt} = \frac{c\sigma_T}{4\pi}(B\sin(\theta))^2\gamma^2 \text{ erg s}^{-1} \tag{2.49}$$

(e.g. Schlickeiser, 2002). Here, B is the magnitude of the magnetic field, θ is the pitch angle of the CR, and γ is the Lorentz factor. Assuming an isotropic distribution of CRs, we can approximate

$$\langle(B\sin(\theta))^2\rangle \approx \frac{2}{3}B^2 \tag{2.50}$$

(see e.g. Torres (2004)). Therefore,

$$\Lambda_{synch} = \frac{1}{6\pi}\frac{\sigma_T}{mc}\gamma\frac{B^2}{n_H} \text{ cm}^3 \text{ s}^{-1} \tag{2.51}$$

2.C.2 Inverse Compton

IC losses take an identical form to the synchrotron losses replacing the magnetic energy density with radiation energy density. The energy loss of one electron interacting with photons with radiation energy density, w, is (e.g. Schlickeiser, 2002)

$$\frac{dE}{dt} = \frac{4}{3}c\sigma_T w\gamma^2 \text{ erg s}^{-1} \tag{2.52}$$

Therefore,

$$\Lambda_{IC} = \frac{4}{3}\frac{\sigma_T}{mc}\gamma\frac{w}{n_H}\ \mathrm{cm}^3\ \mathrm{s}^{-1} \tag{2.53}$$

We approximate the value of w as a combination of the radiation from the CMB and starlight. The value of w_{CMB} is a constant $\sim 4.2 \times 10^{-13}$ erg/cm^3 (Draine, 2011). The value of $w_{\rm star}$ is a combination of UV, optical, and IR emission. The TIGRESS-NCR simulations (Kim et al., 2023a) implement adaptive ray tracing to model the UV radiation field and have similar initial conditions to those of the TIGRESS models that we are post-processing. Therefore, we use the horizontally-averaged, vertical profile of the TIGRESS-NCR radiation field to estimate the value of w_{UV}. Additionally, we take a time average over a 200 Myr span of the TIGRESS-NCR simulation.

To account for optical emission, we use an estimate of the SED of a stellar population taken from Kim et al. (2023b). We multiply the value of w_{UV} by the ratio of UV to optical emission in the SED to find w_{opt}.

The radiation energy density of IR emission must be found separately, as it will not be attenuated as the UV emission is. We approximate,

$$w_{\rm IR}(x_0, y_0, z_0) = \frac{1}{4\pi c}\iiint \frac{L_{IR}(x,y,z)dxdydz}{(x-x_0)^2 + (y-y_0)^2 + (z-z_0)^2} \tag{2.54}$$

where L is the IR luminosity at any point. For our solar neighborhood model, we take $x_0 = 8$ kpc and $y_0 = 0$ kpc. The radiation energy density is then only a function of z, as are w_{UV} and w_{opt}. The IR luminosity of the Milky Way (representing emission from dust heated by starlight) is taken to follow a double exponential,

$$L(x,y,z) = Ae^{-\sqrt{x^2+y^2}/H_r}e^{-|z|/H_z} \tag{2.55}$$

where we choose $H_r = 3$ kpc and $H_z = 200$ pc as the radial and vertical scale lengths. The normalization factor, A, is fixed such that the midplane value of w_{IR}/w_{UV+opt} matches the observed value in the solar neighborhood (Draine, 2011).

We rescale the total value of w to the SFR of each post-processed TIGRESS snapshot by multiplying by the ratio of the SFR in the post-processed simulation to the average SFR in the TIGRESS-NCR model.

2.C.3 Bremsstrahlung

Low energy electrons (E $\lesssim$ 1 GeV) experience significant losses through bremsstrahlung interactions. The form of the energy loss can be divided into two limits, weak and strong shielding. In the weak shielding or completely ionized case, the expression for the energy loss is given by Schlickeiser (2002) to be

$$\frac{d\gamma}{dt} = \frac{3\alpha c\sigma_T}{2\pi}\gamma \sum_Z n_Z Z(Z+1)\left(\ln(\gamma) + \ln(2) - \frac{1}{3}\right) \tag{2.56}$$

where α is the fine structure constant. The sum included in this expression is over all ionized species with atomic number Z. Considering only hydrogen and helium, we have

$$\sum_Z n_Z Z(Z+1) = 2n_{\mathrm{H}^+} + 6(n_{\mathrm{He}^+} + n_{\mathrm{He}^{++}}) \tag{2.57}$$

Therefore,

$$\Lambda_{\mathrm{BS,i}} = \frac{3\alpha c\sigma_T}{\pi}\left(x_{\mathrm{H}^+} + 3x_{\mathrm{He}^+}\right)\left(\ln(\gamma) + \ln(2) - \frac{1}{3}\right) \tag{2.58}$$

where $x_{\mathrm{H}^+} = \frac{n_{\mathrm{H}^+}}{n_H}$ and $x_{\mathrm{He}^+} = \frac{n_{\mathrm{He}^+} + n_{\mathrm{He}^{++}}}{n_H}$. These values are determined as in Section 2.2.6.

In the neutral or strong shielding limit, the expression for bremsstrahlung losses is instead given by Schlickeiser (2002) to be

$$\frac{d\gamma}{dt} = \frac{3.9\alpha c\phi_{\mathrm{HI}}^{s-s}\sigma_T}{8\pi}\gamma(n_{\mathrm{HI}} + 2n_{\mathrm{H2}}) \tag{2.59}$$

where $\phi_{\rm HI}^{s-s} \approx 45$ is the scattering function. This gives,

$$\Lambda_{\rm BS,n} = \frac{3.9\alpha c \phi_{\rm HI}^{s-s} \sigma_T}{8\pi} x_{\rm n} \tag{2.60}$$

The total bremsstrahlung loss expression is then

$$\Lambda_{\rm BS} = \frac{\alpha c \sigma_T}{\pi} \left(3\big(x_{\rm H^+} + 3x_{\rm He^+}\big)\Big(\ln(\gamma) + \ln(2) - \frac{1}{3}\Big) + \frac{3.9\phi_{\rm HI}^{s-s}}{8} x_{\rm n} \right) \tag{2.61}$$

2.C.4 Ionization and Coulomb

At the lowest energies, ionization and Coulomb interactions are the dominant sources of energy losses in CREs. From Schlickeiser (2002), the rate of energy loss due to ionization of neutral hydrogen and helium is

$$\frac{d\gamma}{dt} = 2.7 c \sigma_T (6.85 + \ln(\gamma))(n_{\rm HI} + 2n_{\rm H2}) \tag{2.62}$$

Therefore,

$$\Lambda_{\rm ion} = 2.7 c \sigma_T \frac{6.85 + \ln(\gamma)}{\gamma} x_{\rm n} \tag{2.63}$$

In ionized medium, Coulomb interactions are more important than ionization losses. Interactions with free electrons results in energy losses with the form (Schlickeiser, 2002)

$$\frac{d\gamma}{dt} = \frac{3}{4} c \sigma_T n_e \big(74.3 + \ln(\gamma) - \ln(n_e)\big) \tag{2.64}$$

Therefore,

$$\Lambda_{\rm Coulomb} = \frac{3}{4} c \sigma_T \frac{74.3 + \ln(\gamma) - \ln(n_e)}{\gamma} x_e \tag{2.65}$$

The total energy loss from these two terms is then

$$\Lambda_{\rm ion+Coulomb} = \frac{3}{4} \frac{c\sigma_T}{\gamma} \left(3.6\big(6.85 + \ln(\gamma)\big) x_{\rm n} + \big(74.3 + \ln(\gamma) - \ln(n_e)\big) x_e \right) \tag{2.66}$$

2.D Proton Spectrum

As a comparison, we reproduce some of the figures presented in Chapter 2 considering the CR protons rather than the CREs. The distribution and transport of CR protons in our post-processed models are presented in more detail in Armillotta et al. (2025) along with analytic models of the CR profiles.

The energetic loss rates of CR protons are less significant than those of CREs resulting in a much longer loss timescale (Equation 2.36) compared to either the transport (Equation 2.37) or diffusion (Equation 2.38) timescales. We present these timescales as a function of z for CR protons in Figure 2.12 (as shown for CREs in Figure 2.6). The transport and diffusion timescales are extremely similar between the protons and electrons because both the advection speed and the scattering coefficient are the same between the two populations.

Because the loss timescale is significantly longer for the CR protons compared to the transport times, we would expect the final CR proton spectrum to be determined primarily by energy-dependent transport rather than the energy dependence of the loss mechanisms. In Figure 2.13, we present both the injected and measured midplane CR proton spectra as was done in Figure 2.7 for the CREs making the same temperature and spatial cuts, $T < 3 \times 10^4$ K and $|z| < 300$ pc. We compare our CR proton spectra to direct observations taken with AMS-02 (Aguilar et al., 2015). As with the CRE spectra, we reduce the normalization of the proton spectra by a factor of two to more closely match the observed values. After this renormalization, the CR proton spectra match the direct observations extremely well with the exception of the lowest momentum bin where solar modulation affects the direct observations. As discussed in Section 2.3.4, the disagreement between our results and observations in terms of normalization can be explained by either a difference in SFR between the simulations and the solar neighborhood value, or a difference in energy injection rate per SN. It is encouraging that we reproduce not only the observed CRE and CR proton spectral shapes, but also the proton to electron ratio.

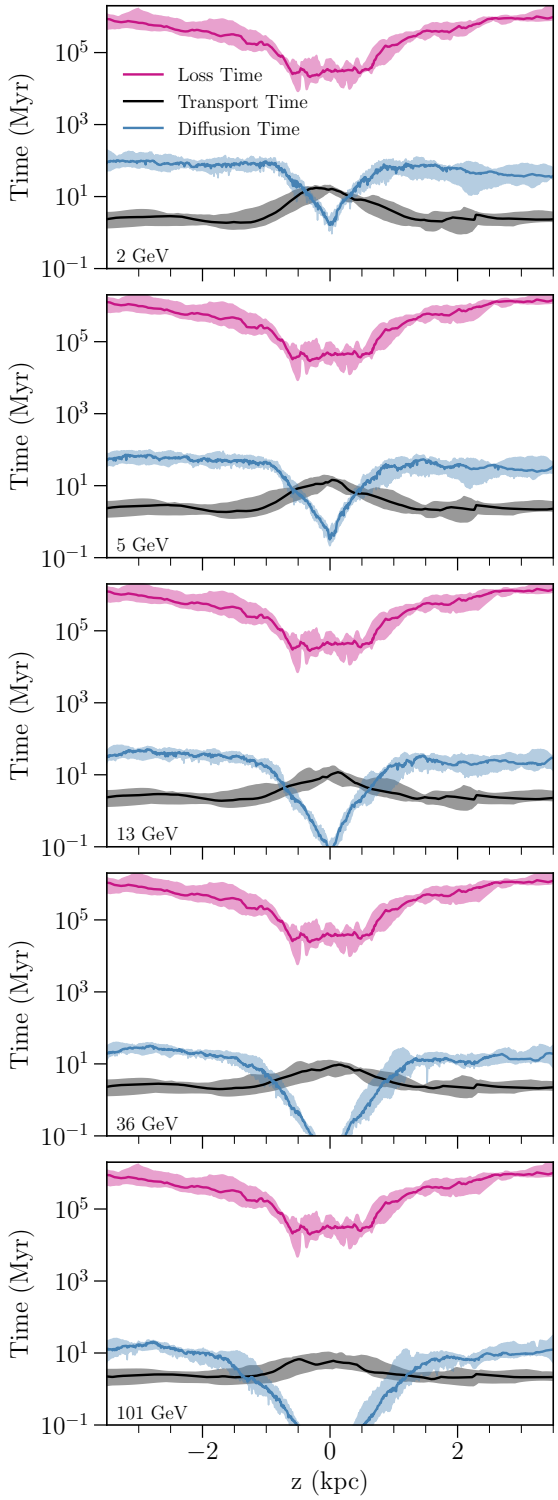

Figure 2.12: Same as Figure 2.6 but for CR protons.

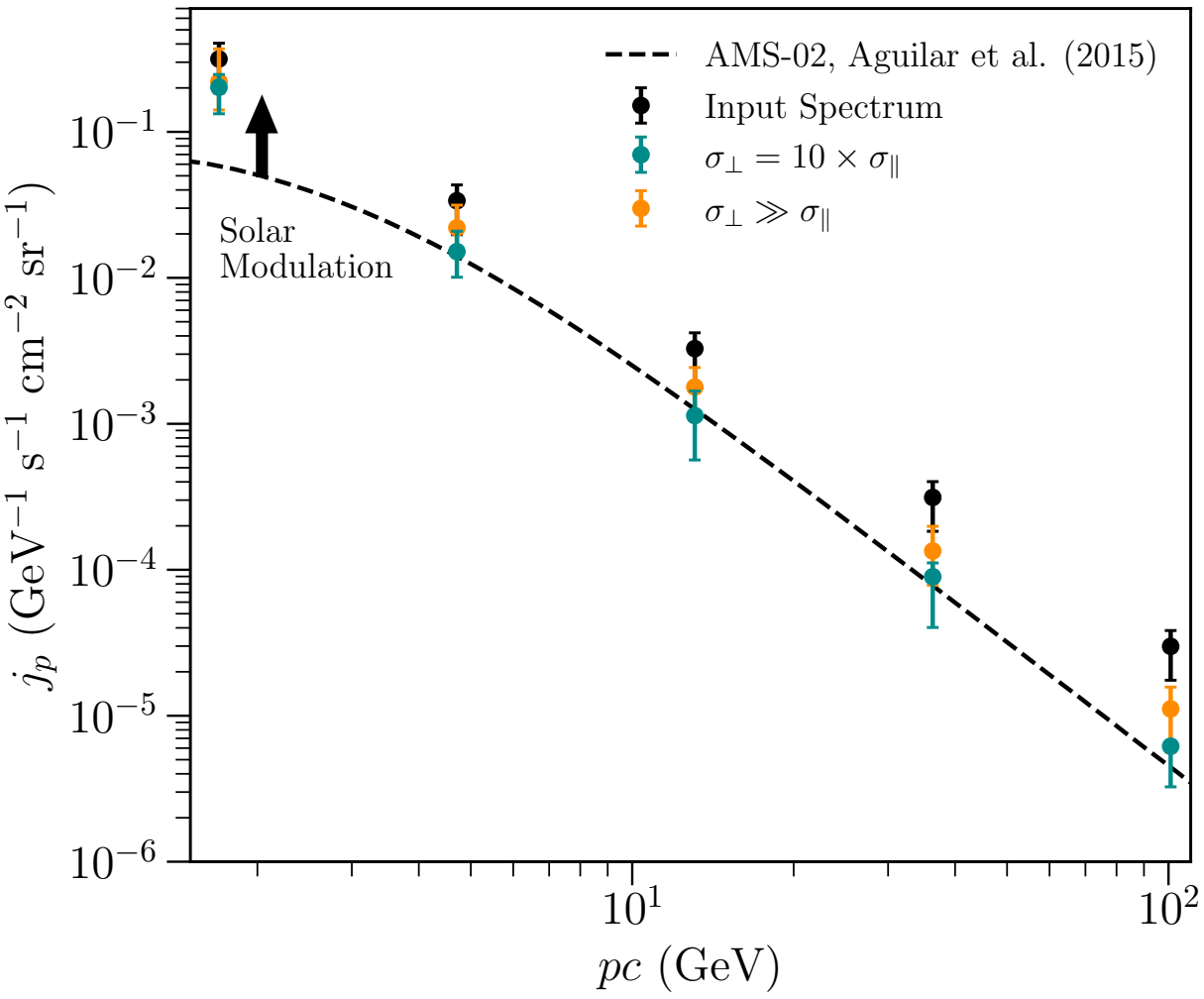

Figure 2.13: Same as Figure 2.7 but for CR protons. The observed values from AMS shown in the black dashed line are taken from Aguilar et al. (2015).

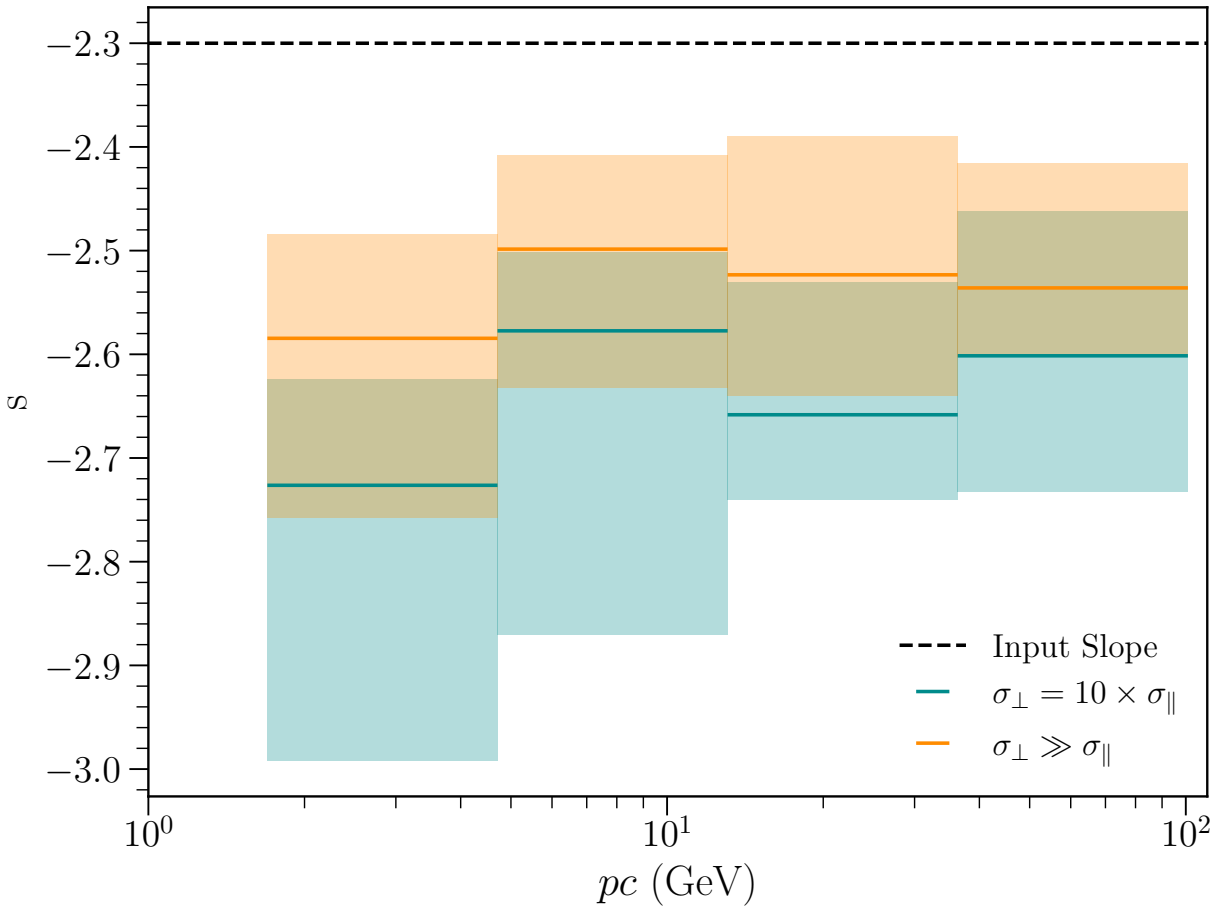

Figure 2.14: Same as Figure 2.8 but for CR protons.

The steepening of the CR proton spectrum is determined by the energetic scaling of the diffusion rate, so it does not change as a function of energy as with the CREs. This can be seen in the CR proton spectral slope, shown in Figure 2.14. Here, we compare the injected slope, $s = -2.3$, to the slope of the final spectra (Equation 2.39). The slope of both the $\sigma_\perp = 10 \times \sigma_\parallel$ and $\sigma_\perp \gg \sigma_\parallel$ models are consistent with a constant value, although the slope of the $\sigma_\perp = 10 \times \sigma_\parallel$ models is slightly steeper than that of the $\sigma_\perp \gg \sigma_\parallel$ models.

Chapter 3

Synchrotron Emission and the Estimation of Magnetic Fields

3.1 Introduction

Direct measurement of the CRE spectrum is possible only in the solar neighborhood, and we have found our model to reproduce this result well. Our understanding of the CR distribution beyond the solar system relies on indirect observations, primarily through radio synchrotron emission. Synchrotron emission is also the most important probe of the magnetic field strength and structure in extragalactic sources (e.g. Beck, 2016; Han, 2017). Other measures of magnetic field strength, such as Zeeman splitting and Faraday rotation, are feasible in the Milky Way but are more challenging in distant galaxies (e.g. Heiles & Crutcher, 2005; Robishaw et al., 2008; Han, 2017). To extract information about the magnetic field from radio synchrotron emission, however, requires assumptions about the CR electron and proton spectra and the relative CR and magnetic field distribution.

The most common simplifying assumption is that of equipartition between the magnetic and total CR energy densities (e.g. Govoni & Feretti, 2004). In the solar neighborhood, it has been shown through independent measurements that these two values are roughly equal

(each approximately 1 eV cm^{-3}). Additionally, equipartition is thought to be a reasonable assumption because the CRs are confined by the magnetized ISM, and the magnetic and CR energy densities could therefore be coupled (e.g. Draine, 2011). There is not a clear justification, however, for why these energy densities should necessarily be equal in all environments and across all physical scales. Below ~ 1 kpc, for example, the CR and magnetic field energy densities are not likely to be in equipartition due to the long mean free path of CR propagation (e.g. Stepanov et al., 2014; Seta & Beck, 2019).

Standard equipartition magnetic field estimates also rely on assumptions about the local CR spectrum (e.g. Beck & Krause, 2005). Although synchrotron emission is primarily produced through interactions of CREs with the magnetic field, the total CR energy density is dominated by protons with energies of approximately 1 GeV (e.g. Zweibel, 2013). In the solar neighborhood, there are direct measurements of the relative normalization and spectral shape of the proton and electron spectra, but for extragalactic sources these values typically must be estimated (except to some extent in the few sources with both gamma-ray and radio observations; e.g., McDaniel et al. (2019)). The choice of CRE spectral index has been shown to make an impact on the resulting measurement of magnetic field strength (Padovani et al., 2021; Bracco et al., 2024).

Other groups have previously used simulations to test the equipartition assumption. For example, Ponnada et al. (2024) use magnetohydrodynamic (MHD) cosmological zoom-in FIRE simulations (Hopkins et al., 2022a), which evolve CR spectra self-consistently, to produce mock synchrotron observations and estimate the equipartition magnetic field strength. They find this method to underestimate the true magnetic field and present a possible improvement to the method by considering the volume filling fraction of synchrotron emission in the multi-phase ISM. On the other hand, Dacunha et al. (2025) impose different CR distributions onto galaxy simulations and find that the equipartition assumption overestimates the magnetic field strength.

The post-processed models presented in Chapter 2 include both a spectrally resolved CRE population, and the magnetic field strength, and we can therefore use them to produce synthetic synchrotron maps. The synthetic synchrotron emission obtained from our simulations is at a spatial resolution of 8 pc (or 12 pc, see Section 3.2.1), equivalent to an angular resolution of approximately 1.65" (or 2.5") for a galaxy at 1 Mpc. This resolution is achievable with observations from surveys such as the Local Group L-Band Survey[1] using the Karl G. Jansky Very Large Array (VLA) or future observations using the next-generation VLA (e.g. McKinnon et al., 2019) or Square Kilometre Array (e.g. Braun et al., 2015). We will use this mock radio emission to test the equipartition estimate of magnetic field strength on small ($\lesssim$ kpc) scales.

In Section 3.2, we describe the method we use to produce synthetic synchrotron maps and estimate the equipartition magnetic field strength from these mock observations. Section 3.3.2 presents one application of our model to testing diagnostic methods, in which we compare the CRE spectrum that would be inferred from synchrotron observations to the underlying CRE spectrum, as would be measured with direct detection. We test of the equipartition estimate of magnetic fields in Section 3.2.3, and possible alternative methods to extract the magnetic field strength with additional observations in Section 3.3.4. We present our final results looking at magnetic field structure using polarized emission in Section 3.3.5. In Section 3.4 we discuss the implication of our results on the use of the synchrotron emission for understanding the underlying CRE spectrum and magnetic field. Finally, we summarize our results and present our conclusions in Section 3.5.

[1] https://www.lglbs.org/

3.2 Methods

3.2.1 TIGRESS Models

We make use of the post-processed `R8` simulations presented in Chapter 2 to produce synthetic maps of synchrotron emission. One goal of this work is to test the dependence of the equipartition estimate on physical scale. Therefore, we additionally post-process four snapshots from the `R8 Arm` model using the same CR transport scheme. This model has a larger box size compared to `R8`, and includes a denser, central arm feature. The `R8 Arm` box has $L_x = 3141.6$ pc and $L_y = L_z = 6283.2$ pc with a resolution of $\Delta x \approx 12.3$ pc. Hix et al. (in prep.) analyzes CR transport in the `R8 Arm` model in more detail, along with TIGRESS models representing different galactic conditions beyond the solar neighborhood. All of the simulations in this chapter use one definition of the perpendicular scattering coefficient, with $\sigma_\perp = 10 \times \sigma_\parallel$.

All results presented for the `R8` model are after the MHD relaxation step (Section 2.2.2), although we find that the synthetic synchrotron emission, and the resulting equipartition estimate of the magnetic field, does not change significantly before and after the MHD variables are allowed to evolve. The `R8 Arm` post-processing does not include this step due to its more complex boundary conditions, which would necessitate modifications to the code.

3.2.2 Synthetic Synchrotron Emission

We use the simulated CRE spectrum to produce synthetic synchrotron emission using the method described in Padovani et al. (2021), which we summarize here (see also Ponnada et al., 2024). The specific emissivity (i.e. per unit volume per unit time per unit solid angle per unit frequency) from each cell is given by

$$\epsilon_{\nu,\parallel} = \int_{m_e c^2}^{\infty} \frac{j_e(E)}{v_e(E)} P_{\nu,\parallel}(E) dE \tag{3.1}$$

$$\epsilon_{\nu,\perp} = \int_{m_e c^2}^{\infty} \frac{j_e(E)}{v_e(E)} P_{\nu,\perp}(E) dE \tag{3.2}$$

where the parallel and perpendicular components are relative to the line of sight. Here, the emissivity is found by integrating over all CRE energies, but we only simulate CREs with energies between 2-101 GeV. We extrapolate to a range of 1-10^3 GeV by assuming a constant power law slope at energies above and below our simulated bins. This approximation is consistent with direct observations (e.g. Padovani et al., 2021). However, we are limited to modeling synchrotron frequencies in which the emissivity is dominated by CREs in our simulated energy range.

The synchrotron power per unit frequency emitted at frequency ν is given by

$$P_{\nu,\parallel} = \frac{\sqrt{3} e^3}{2 m_e c^2} B_\perp (F(x) - G(x)) \tag{3.3}$$

$$P_{\nu,\perp} = \frac{\sqrt{3} e^3}{2 m_e c^2} B_\perp (F(x) + G(x)) \tag{3.4}$$

where $B_\perp$ is the magnitude of the magnetic field perpendicular to the line of sight. F(x) and G(x) are the synchrotron functions given by

$$F(x) = x \int_x^{\infty} K_{5/3}(\xi) d\xi \tag{3.5}$$

$$G(x) = x K_{2/3}(x) \tag{3.6}$$

in which $K_{5/3}$ and $K_{2/3}$ are modified Bessel functions of order 5/3 or 2/3 and $x = \nu/\nu_c$ with ν_c the critical frequency,

$$\nu_c = \frac{3 e B_\perp}{4 \pi m_e c} \left(\frac{E}{m_e c^2} \right)^2. \tag{3.7}$$

The values of F(x) and G(x) are taken from tables provided by Padovani et al. (priv. comm.) (also tabulated in Shu, 1991).

These emissivities are integrated along the line of sight to find the specific intensity, I_ν, along with the Stokes parameters, Q_ν and U_ν as follows

$$I_\nu = \int_{-L_z/2}^{L_z/2} (\epsilon_{\nu,\parallel} + \epsilon_{\nu,\perp}) dz, \tag{3.8}$$

$$Q_\nu = \int_{-L_z/2}^{L_z/2} (\epsilon_{\nu,\perp} - \epsilon_{\nu,\parallel}) \cos(2\varphi) dz, \tag{3.9}$$

$$U_\nu = \int_{-L_z/2}^{L_z/2} (\epsilon_{\nu,\perp} - \epsilon_{\nu,\parallel}) \sin(2\varphi) dz. \tag{3.10}$$

In these equations, φ, describes the local polarization angle, which is found by rotating 90° relative to $B_\perp$ in the observed plane.

If the CR distribution were described by a single power law in energy with $j_e \propto E^s$ (where $j_e \propto f(E)E^2$ in the relativistic regime) then the synchrotron intensity will also be a power law with $I_\nu \propto \nu^{-\alpha}$ where $\alpha = -(s+1)/2$ (see e.g. Shu (1991) equation 19.31). Note that with $f(p) \propto p^{-\gamma}$ (i.e. $\gamma = 2 - s$ in the relativistic regime) this is equivalent to $\alpha = (\gamma - 3)/2$.

From these mock observables, we can estimate the polarization angle as

$$\varphi = \frac{1}{2} \arctan\left(\frac{U_\nu}{Q_\nu}\right). \tag{3.11}$$

3.2.3 Equipartition Estimate

Using our mock synchrotron observations, we will test the equipartition estimate of magnetic field strength as presented in Beck & Krause (2005). We summarize the results relevant to our analysis here, and point to Appendix A in Beck & Krause (2005) for the full derivation.

First, assume a CRE distribution with the number density given by

$$n_{\mathrm{e}}(E)\mathrm{d}E = n_{\mathrm{e},0}(E/E_0)^{-\gamma_{\mathrm{e}}}\mathrm{d}E \tag{3.12}$$

where $n_{\mathrm{e},0}$ represents the normalization at reference energy E_0, and the distribution has a power law slope with spectral index γ_e. This is related to the CRE spectrum as

$$j_e(E)\mathrm{d}E = \frac{v_e}{4\pi} n_e(E)\mathrm{d}E. \tag{3.13}$$

The total synchrotron intensity at frequency ν can then be estimated as

$$I_\nu = c_2(\gamma_\mathrm{e}) n_{\mathrm{e},0} E_0^{\gamma_\mathrm{e}} (\nu/2c_1)^{(1-\gamma_e)/2} \ell_z B_\perp^{(\gamma_\mathrm{e}+1)/2} \tag{3.14}$$

assuming a constant magnetic field and CRE spectrum along the line of sight. This differs from Equation 3.8 in which the synchrotron emissivity varies as a function of the local CR properties and magnetic field strength. The length scale of synchrotron emission, ℓ_z, is typically taken to be of order $1 - 2$ kpc when considering emission from a face-on source (Beck, 2016; Ponnada et al., 2024). We set $\ell_z = 1$ kpc, which is approximately twice the scale height of synchrotron emission in our simulation, but note that the choice of ℓ_z does not significantly impact the final estimate.

The constants c_1 and c_2 are defined as

$$c_1 = \frac{3e}{4\pi m_e^3 c^5} \approx 6.3 \times 10^{18}\ \mathrm{erg}^{-2}\ \mathrm{s}^{-1}\ \mathrm{G}^{-1} \tag{3.15}$$

and

$$c_2 = \frac{\sqrt{3}e^3}{16\pi m_e c^2} \frac{\gamma_\mathrm{e} + \frac{7}{3}}{\gamma_\mathrm{e} + 1} \Gamma\left(\frac{3\gamma_\mathrm{e} - 1}{12}\right) \Gamma\left(\frac{3\gamma_\mathrm{e} + 7}{12}\right). \tag{3.16}$$

Beck & Krause (2005) make the assumption that for kinetic energies above the proton rest mass energy ($E_\mathrm{p} \equiv m_\mathrm{p} c^2$, with m_p the proton mass), and below the energy at which synchrotron and IC losses become significant, the CR proton and electron spectra have the same slope with power law index $\gamma = \gamma_\mathrm{e}$, and the ratio in the normalization of the two distributions is $K_0 = 100$.

Using these assumptions, they solve equation Equation 3.14 for $n_{\rm e,0}$ and convert to $n_{\rm p,0}$. Then, integrating the distribution function (Equation 3.12) to find the total CR energy density ($e_{\rm c}$) gives

$$e_{\rm c} = \frac{\gamma(K_0+1)E_p^{2-\gamma}(\nu/2c_1)^{(\gamma-1)/2}}{2(\gamma-2)c_2(\gamma)} \frac{I_\nu}{\ell_z B_\perp^{(\gamma+1)/2}}. \tag{3.17}$$

To convert $B_\perp$ to the total magnitude of the magnetic field, Beck & Krause (2005) set

$$B_\perp^{(\gamma+1)/2} = [B\cos(i)]^{(\gamma+1)/2} = c_4(i)B^{(\gamma+1)/2} \tag{3.18}$$

where i is the inclination angle. In this case, $i = 0$ ($c_4 = 1$) corresponds to a face-on view which we use for this analysis.

At this point, an assumption must be made for the value of $e_{\rm c}$ to solve for B. In the traditional approach, this is where the equipartition assumption is adopted, letting $e_{\rm c} = B^2/8\pi$. Then, solving for the magnetic field strength gives the final estimate,

$$B_{\rm eq} = \left[\frac{4\pi(2\alpha+1)(K_0+1)E_{\rm p}^{1-2\alpha}(\nu/2c_1)^\alpha}{(2\alpha-1)c_2(\alpha)c_4(i)} \frac{I_\nu}{\ell_z}\right]^{\frac{1}{\alpha+3}}. \tag{3.19}$$

Here, $\alpha = (\gamma-1)/2$ and can be observationally estimated from synchrotron intensity measured at two different frequencies (ν_1 and ν_2) as

$$\alpha = -\frac{\log(I_{\nu_1}/I_{\nu_2})}{\log(\nu_1/\nu_2)}. \tag{3.20}$$

3.3 Results

3.3.1 Mock Synchrotron Maps

Using the method described in Section 3.2.2, we calculate the synchrotron emissivity in each snapshot as if an observer were looking vertically through the simulation box. We then integrate this emissivity to find the total synchrotron intensity. The total synchrotron

intensity is dominated by emission near the midplane where CR feedback does not strongly affect ISM structure. Therefore, we can produce useful mock synchrotron observations even without self-consistent MHD and CR evolution. Each snapshot of the `R8` model provides a mock observation of a 1 kpc square patch of a face-on galaxy.

One example of the synchrotron emission at 1.5 GHz (L-band) is shown for the `R8` snapshot at $t = 214$ Myr in Figure 3.1. The upper row shows slices through $z = 0$ of the CRE spectrum, $j_{\rm e}$, at $E = 5$ GeV, the square of the magnetic field strength B^2, and the synchrotron emissivity ϵ_ν. The vertically integrated values of each of these three quantities are shown in the second row. Both the single slice and vertical integral of B^2 show much more variation in the $x - y$ plane compared to j_e. Therefore, while the CRE spectrum is crucial for determining the overall magnitude of the synchrotron emission, the spatial distribution of synchrotron emission distribution is driven by that of the magnetic field.

3.3.2 Extracting the CRE Spectral Slope

Although the spatial distribution of synchrotron emission is almost independent of that of CREs, its distribution in frequency space is determined by the CRE spectral slope. Therefore, synchrotron observations at multiple frequencies can be used to estimate the underlying CRE spectral slope as in Equation 3.20. The corresponding CRE spectral slope can then be estimated as $s = -2\alpha - 1$ (Section 3.2.2).

Using our simulations, we can compare the true CRE spectral slope (as in Figure 2.8) to the slope that would be estimated from synchrotron observations. To do so, we generate maps of artificial synchrotron emission at eight frequencies corresponding to eight VLA radio bands (1.5, 3, 6, 10, 15, 22, 33, and 45 GHz)[2]. Between each pair of frequencies, we determine the radio spectral index and from this estimate the CRE spectral slope.

In Figure 3.2, we compare the slopes of the simulated CR spectrum at different E to the slopes estimated from the mock synchrotron observations. This is done for four of our

[2]https://science.nrao.edu/facilities/vla/docs/manuals/oss2013B/performance/bands

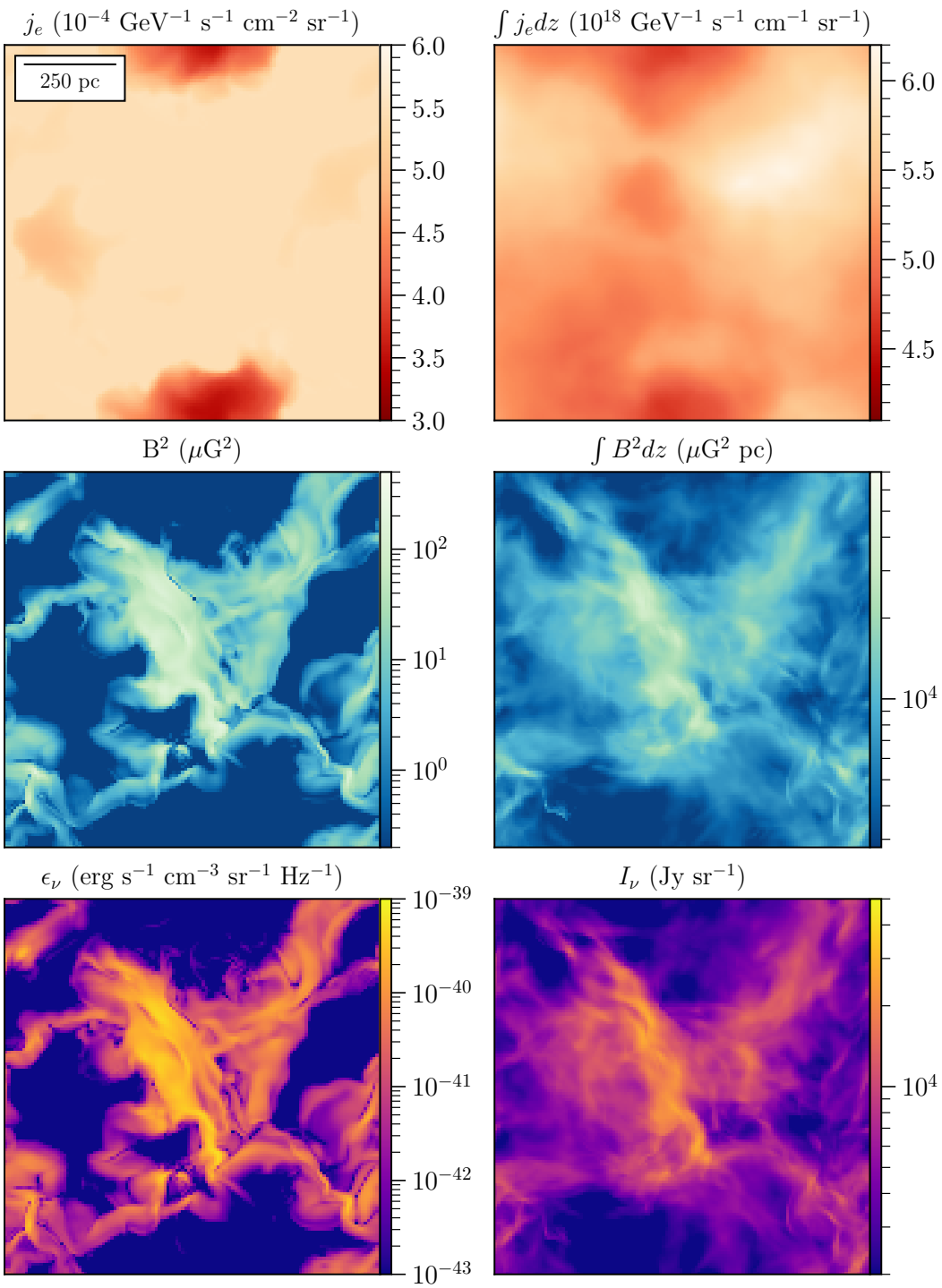

Figure 3.1: The left panels represent slices at $z = 0$ of quantities relevant to synchrotron emission from the `R8` snapshot at $t = 214$ Myr. From top to bottom, these are j_e, B^2, and synchrotron emissivity ϵ_ν. The right panels represent these same quantities integrated vertically through the entire box. The lower right panel shows the synchrotron intensity I_ν. The value of j_e is for the 5 GeV electron energy bin. The synchrotron emissivity and intensity are evaluated at 1.5 GHz (L-band).

snapshots. Each panel is labeled with the simulation time of the TIGRESS snapshot, along with the corresponding SFR surface density, $\Sigma_{\rm SFR}$. The true slopes of the underlying CRE spectrum (represented by black bars) are the median values calculated using Equation 2.39, including all cells within $z < |300|$ pc and with $T < 3 \times 10^4$ K, as in Figure 2.8. The majority of the variation in the slopes shown in Figure 2.8 is due to differences between snapshots rather than between cells in one snapshot. Therefore, the error bars representing the 16th-84th percentile ranges of the slope are not visible in most of the panels of Figure 3.2. These estimates for the CR slope represent the values that would be measured using direct detection, as we measure the CR spectrum in the solar neighborhood.

The red and blue bars in each panel represent the CRE slope estimated from the spectral index of the mock synchrotron emission. The dark central line within both the red and blue bars are the median value and the height of the bars shows the 16th-84th percentile range taking the distribution across all cells in the synchrotron map in the $x-y$ plane. The locations of these bars along the x-axis represent the CRE energies which contribute to the synchrotron emission at each frequency. An individual CRE at a given energy will produce synchrotron emission at a range of frequencies, with a peak at a critical frequency. Therefore, synchrotron emission at a given frequency will be due to a population of CREs with a range of energies peaking at a critical CR energy. Any measurement of the synchrotron spectral index will probe the CR slope at this specific range of CR energy.

We estimate the CR energies which contribute to the synchrotron emission at each frequency in two different ways. The wider, red bars use the simulated values of synchrotron emissivity, ϵ_ν, to find which CRE energies are responsible for the majority of the synchrotron emission. To define this range, we find the energies which represent the 16-84th percentile around the peak of ϵ_ν through Equation 3.1 and Equation 3.2. This estimate is not possible in reality, as only the integrated intensity rather than the emissivity is observable.

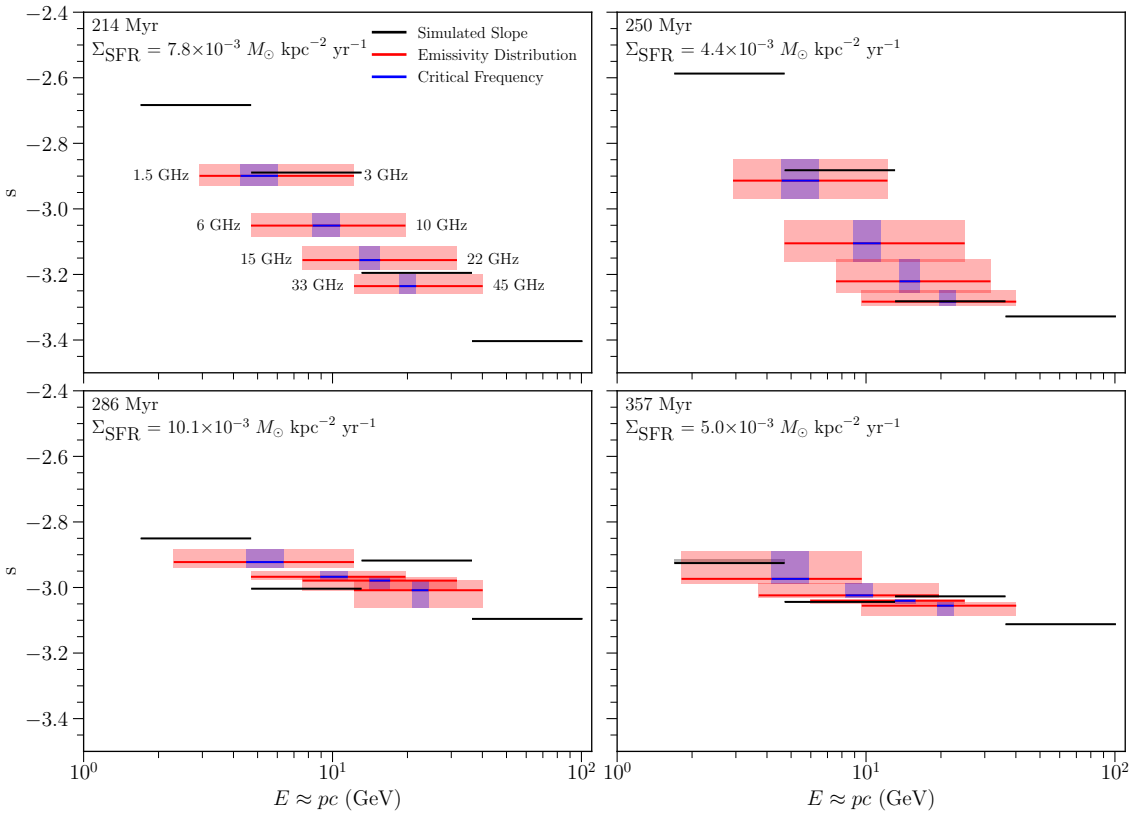

Figure 3.2: Comparison of the simulated CR power law slope to the value estimated from the mock synchrotron observations for four TIGRESS snapshots. The black bars represent the median power law slope of the simulated CR spectrum, evaluated over all cells within $z < |300|$ pc and with $T < 3 \times 10^4$ K (as in Figure 2.8). The red and blue bars represent the slope estimated from comparing the synchrotron intensities at the two frequencies listed to the side. The central line represents the median value, while the vertical extent shows the 16th-84th percentiles. The extension of the bars on the x-axis covers the range of energies of CREs contributing to the emission at those frequencies. The energy range shown in red is estimated from the integrand in Equation 3.1 and Equation 3.2, spanning the energies that represent the 16th-84th percentile of total emission. The blue bars span the critical energies corresponding to the two frequencies (Equation 3.21), assuming the magnetic field takes the equipartition value. Each panel is labeled with the snapshot time and the corresponding value of the SFR surface density.

The narrower, blue bars represent an estimate based only on observable values. For a given frequency, ν, the majority of emission will be due to CRs at energies of around

$$E_{\rm crit} \approx \left(\frac{\nu}{16\ {\rm MHz}}\right)^{0.5} \left(\frac{B_\perp}{\mu{\rm G}}\right)^{-0.5} \tag{3.21}$$

where $B_\perp$ is the component of the magnetic field perpendicular to the CR velocity (Beck & Krause, 2005). The magnetic field is not known in observations, but a value can be obtained using the equipartition assumption (Equation 3.19) which can then be used to determine $E_{\rm crit}$. The blue bars in Figure 3.2 span the values of $E_{\rm crit}$ at each of the radio frequencies used for the estimate of the CR spectral index.

We find that the value of the CR spectral index estimated from the synchrotron emission matches the directly measured values extremely well for each of the four snapshots shown in Figure 3.2. The magnetic field is strongest, and the CR energy density is highest, at the midplane, so the synchrotron emission is dominated by the midplane gas. Therefore, the CR slope estimated from this emission would be expected to match the directly observed values at the midplane. The CR spectral index can be robustly recovered from synchrotron observations. We note that our mock radio observations do not include any thermal free-free emission which would also be present especially at the higher frequencies we model. In true observations, this emission needs to be removed to learn about the underlying CR spectrum from the synchrotron emission.

3.3.3 Traditional Equipartition Estimate

3.3.3.1 `R8` Model

For each of our `R8` snapshots, we produce synthetic maps of synchrotron emission at 1.5 and 3 GHz (Section 3.2.2) corresponding to L and S band observations. Our results are insensitive to the particular choice of frequencies. From these mock observations, we determine the equipartition magnetic field strength in each pixel with Equation 3.19. In Figure 2.1 we

present the face-on view of one R8 snapshot including I_ν at 1.5 GHz as well as the mass-weighted average values of the total CR energy density ($e_{\mathrm{c},avg}$) and simulated magnetic field strength (B_{avg}). We also include the magnetic field strength determined by the equipartition estimate, B_{eq}.

The total CR energy density is found by integrating the CR proton spectrum, j_p, with respect to CR energy. We define j_p in an analogous way to j_e, with the CR proton spectrum in one energy bin given by $j_{\mathrm{p},j}(E_j) \approx e_{\mathrm{c},j} v_{\mathrm{p},j}/(4\pi E_j^2 d\ln E)$. We then interpolate between the simulated bins representing j_p as a broken power law.

Qualitatively, the maps of I_ν, B_{avg}, and B_{eq} have similar spatial structure. However, B_{avg} has much larger variation in magnitude than B_{eq}. Compared to the other three panels, $e_{\mathrm{c},avg}$ is smoother and has very little variation in magnitude across the simulation box. From only these snapshots, we can predict that equipartition between the magnetic field and CRs will not necessarily hold on the simulation-resolution scale.

In Figure 3.4, the two-dimensional histogram compares the values of B_{eq} and B_{avg} from every pixel across all R8 snapshots. We also include the kpc-scale mean value of both B_{eq} and B_{avg} by averaging across each snapshot individually. The kpc-averages of B_{eq} and B_{avg} are consistent with each other for each snapshot, but the distribution showing values from individual (projected) pixels does not have the same agreement. We include a linear best-fit relating $\log(B_{\mathrm{eq}})$ and $\log(B_{\mathrm{avg}})$ in purple. If B_{eq} were a good estimator of B_{avg} we would expect this relationship to have unity slope, matching the black, dashed line. Instead, we find that $B_{\mathrm{eq}} \propto B_{\mathrm{avg}}^{0.36}$.

We can understand this power-law scaling between B_{eq} and B_{avg} by considering the derivation of the equipartition magnetic field estimate. From Equation 3.14, we know $I_\nu \propto B^{\alpha+1} n_{\mathrm{e},0}$, with $n_{\mathrm{e},0} \propto e_c$. Based on the smooth CR distribution seen in Figure 2.1, $n_{\mathrm{e},0}$ is essentially constant, independent of B. Substituting $I_\nu \propto B^{\alpha+1}$ into Equation 3.19, we see that $B_{\mathrm{eq}} \propto B^{(\alpha+1)/(\alpha+3)}$. The CRE spectral index is observed to be between 2 and 3.3 for CREs between $\sim 1 - 10$ GeV which contribute primarily to 1.5-3 GHz emission in

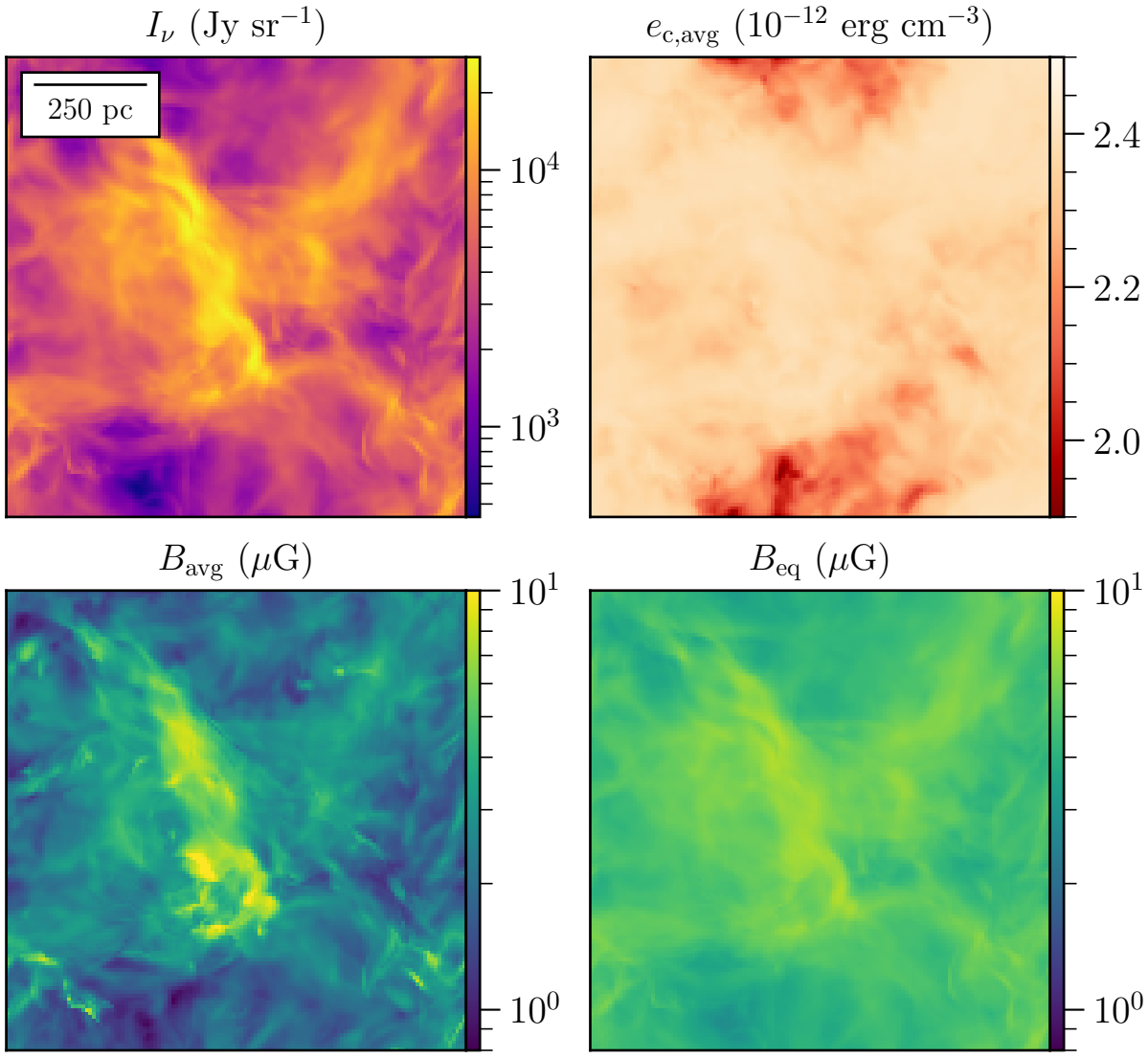

Figure 3.3: Vertically integrated and mass-averaged quantities from one snapshot of the `R8` simulation. From left to right, the four panels show synchrotron intensity (I_ν) at 1.5 GHz (Equation 3.8), the total mass-weighted average CR electron energy density ($e_{c,\rm avg}$), the mass-weighted average magnetic field strength ($B_{\rm avg}$), and the traditional equipartition estimate of the magnetic field strength ($B_{\rm eq}$) as determined by Equation 3.19 from the synchrotron intensity. We can see that $e_{c,avg}$ is nearly constant spatially while $B_{\rm avg}$ has much greater variation. Therefore, the spatial distribution of I_ν primarily traces $B_{\rm avg}$, and the traditional equipartition estimate fails at small scales.

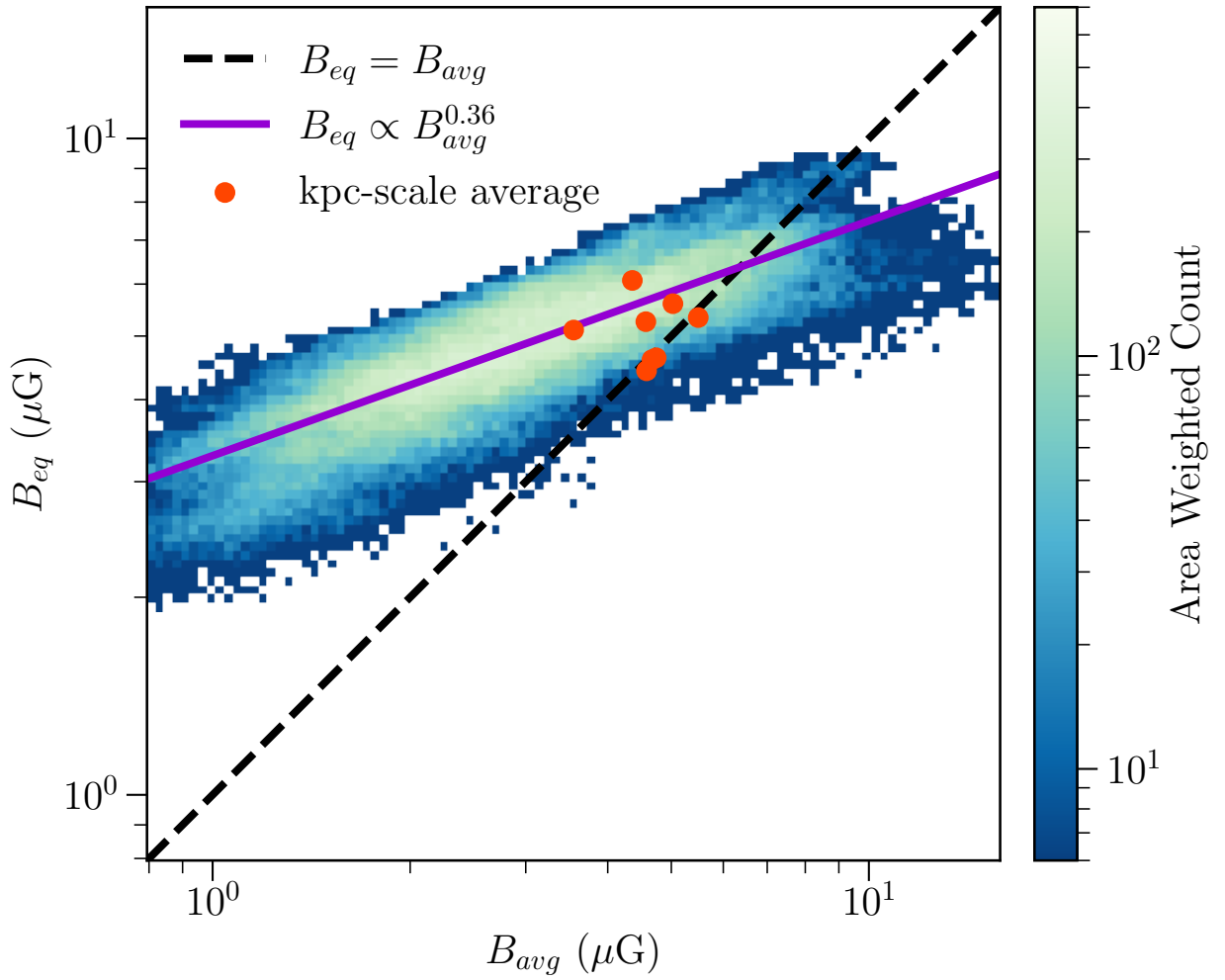

Figure 3.4: The blue distribution represents a two-dimensional histogram of the traditional equipartition magnetic field strength, $B_{\rm eq}$ (Equation 3.19), compared to the measured (mass-weighted) average magnetic field strength, $B_{\rm avg}$. The distribution includes each pixel across all `R8` model snapshots. The best fit power law to this distribution is included as a purple line with $B_{\rm eq} \propto B_{\rm avg}^{0.36}$. The black, dashed line represents $B_{\rm eq} = B_{\rm avg}$. The red points represent the values of $B_{\rm eq}$ and $B_{\rm avg}$ averaged over each kpc-scale simulation snapshot individually. While the large-scale snapshot-averaged value of $B_{\rm eq}$ estimates the large-scale average of $B_{\rm avg}$ well, the pixel-by-pixel comparison shows that $B_{\rm eq}$ fails to recover the true $B_{\rm avg}$ at smaller scales.

environments with $B \sim 1 - 10$ μG the (e.g. Padovani et al., 2021). This corresponds to α between 0.5 and 1.15. Therefore, we may expect $B_{\rm eq} \propto B^{0.4-0.5}$ when using Equation 3.19.

3.3.3.2 `R8 Arm` model

To supplement the `R8` models originally described in Chapter 2, we also post-process and analyze snapshots from the `R8 Arm` model. These additional models allow us to evaluate the traditional equipartition estimate across a wider range of spatial scales and physical conditions. In Figure 3.5 we present one snapshot of this model as in Figure 3.3. The `R8 Arm` model, like the `R8` simulation, shows a very smooth CR distribution compared to the magnetic field strength. The arm structure is visible in all panels but is most prominent in I_ν and in the magnetic fields. As in the `R8` model, the spatial structure is similar in all panels, but $B_{\rm eq}$ has less variation when compared to the true magnetic field strength.

As in Section 3.3.3.1, we estimate the magnetic field strength using the traditional equipartition estimate of Equation 3.19. We compare the values of $B_{\rm eq}$ to $B_{\rm avg}$ in each pixel in Figure 3.6. Similar to the results for the `R8` model, we see that $B_{\rm eq}$ does not agree with the true magnetic field at the simulation resolution ($\sim$12 pc). The best power-law fit of $B_{\rm eq}$ as a function of $B_{\rm avg}$ gives $B_{\rm eq} \propto B_{\rm avg}^{0.44}$. The reason for this sublinear scaling is the same as discussed in Section 3.3.3.1.

Because the `R8 Arm` simulation box is larger than for the `R8` model, we can compare the magnetic field strength averaged over kpc-scale patches to the equipartition estimate. We include these results in Figure 3.6 as green points. For the original, kpc-scale `R8` models, we found that the average equipartition magnetic field over the entire simulation box was a good estimate of the true magnetic field (see the red points in Figure 3.4). In the `R8 Arm` model, however, we do not see good agreement between $B_{\rm eq}$ and $B_{\rm avg}$ at the kpc scale. Instead, the green points follow roughly the same scaling between $B_{\rm eq}$ and $B_{\rm avg}$ as the values at the simulation resolution.

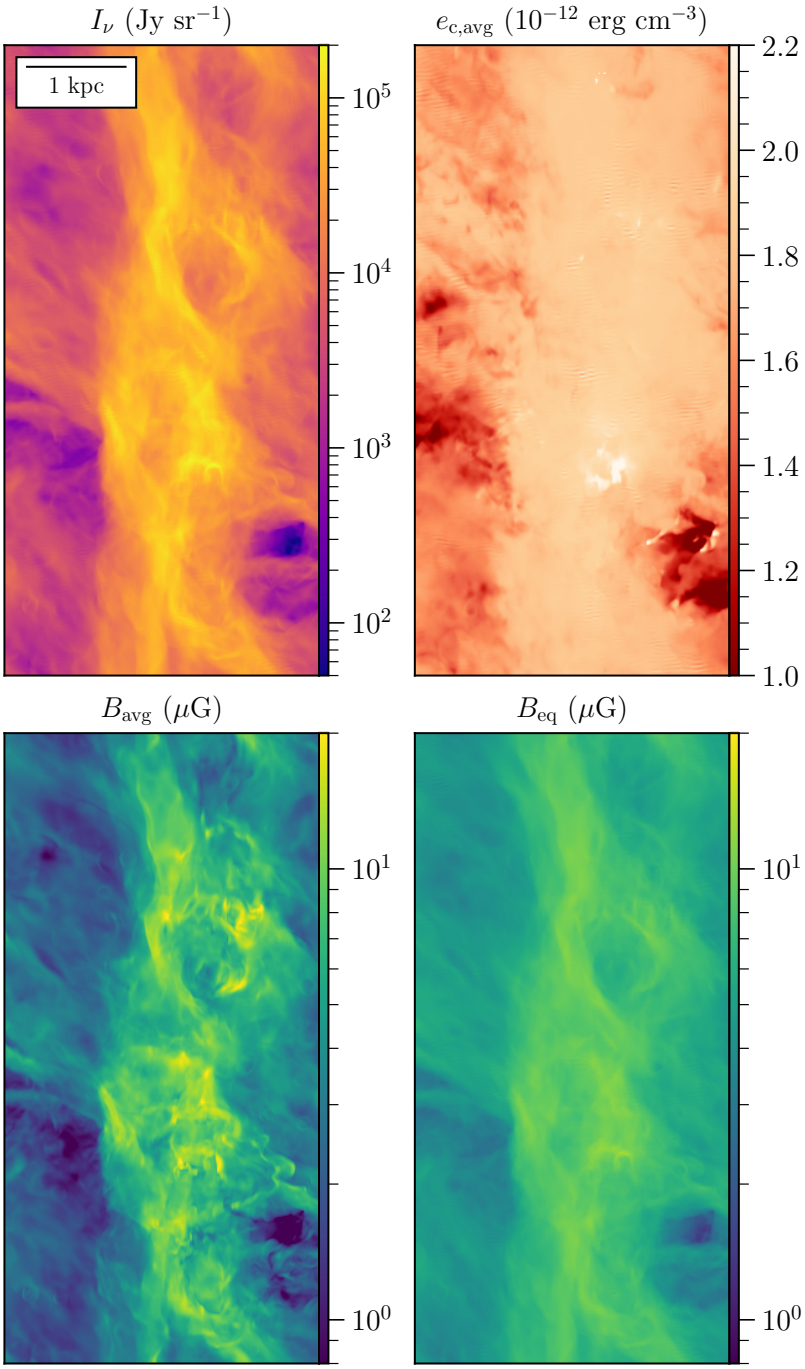

Figure 3.5: Vertically integrated and mass-averaged quantities from one snapshot of the `R8 Arm` simulation. From left to right, the four panels show synchrotron intensity (I_ν) at 1.5 GHz (Equation 3.8), the total mass-weighted average CR electron energy density ($e_{c,\mathrm{avg}}$), the mass-weighted average magnetic field strength (B_{avg}), and the equipartition estimate of the magnetic field strength (B_{eq}) from Equation 3.19. As in Figure 2.1, we see that $e_{c,\mathrm{avg}}$ is approximately constant while B_{avg} has greater variation. The spatial distribution of I_ν is again determined by B_{avg}, and B_{eq} does not estimate the small-scale magnetic field well.

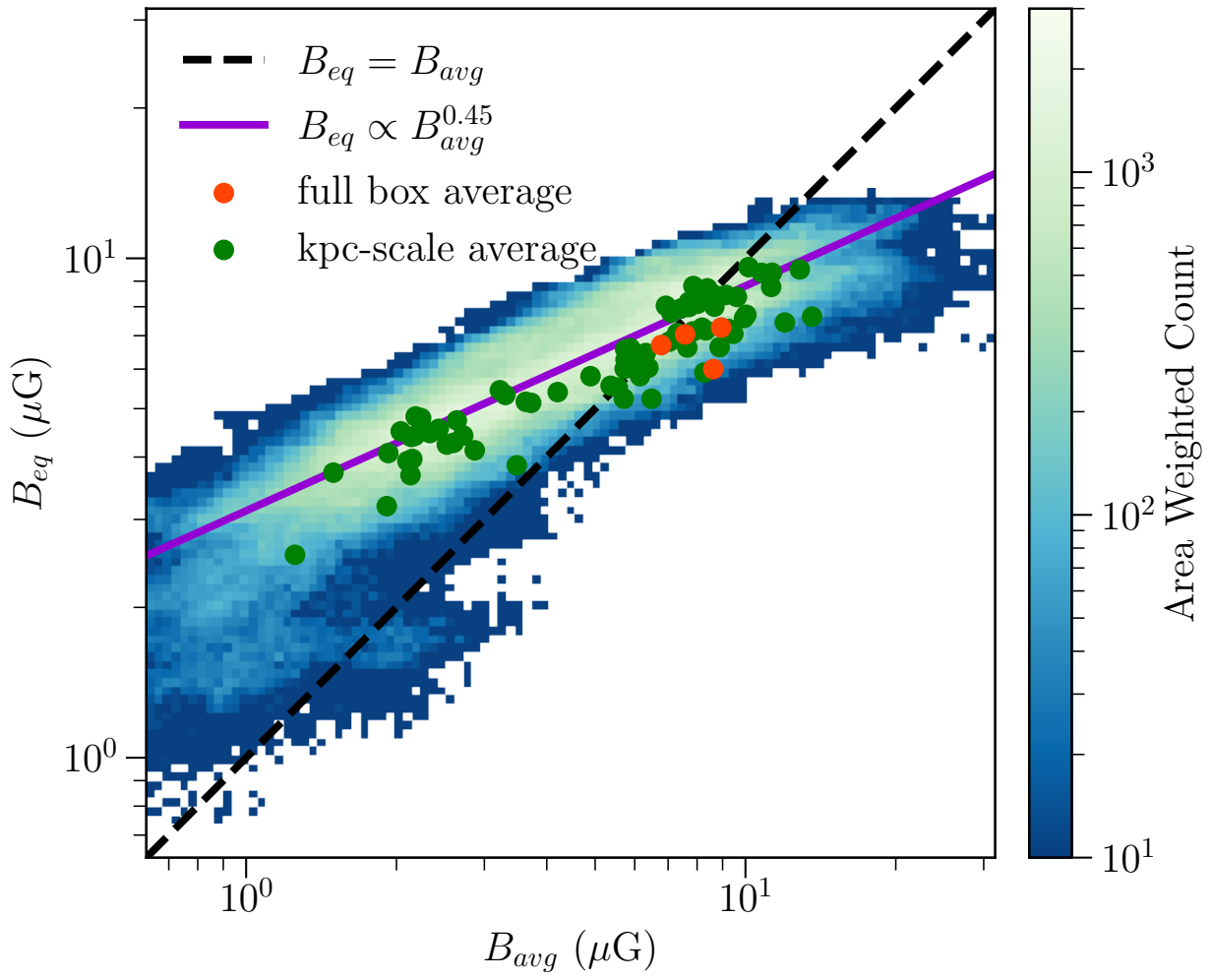

Figure 3.6: The blue distribution represents a two-dimensional histogram of the equipartition magnetic field strength, $B_{\rm eq}$, compared to the simulated, mass-averaged magnetic field strength, $B_{\rm avg}$. This distribution includes each pixel across all R8 Arm model snapshots. The best fit power law to this distribution is included as a purple line. The black, dashed line represents $B_{\rm eq} = B_{\rm avg}$. The red points represent the values of $B_{\rm eq}$ and $B_{\rm avg}$ averaged over the full simulation snapshots. The green points represent the averages over non-overlapping, 1 kpc-scale patches of each snapshot. As in Figure 3.4, the snapshot-averaged estimate of $B_{\rm eq}$ estimates $B_{\rm avg}$ well while there is disagreement between the two values at the simulation resolution scale. In these models, however, we see that an average estimate of $B_{\rm eq}$ over kpc-scale patches disagrees with $B_{\rm avg}$ unlike the kpc-scale, snapshot averaged values of the `R8` models.

If we average over the full `R8 Arm` snapshots, shown in the red points of Figure 3.6, we do see approximate agreement between $B_{\rm avg}$ and $B_{\rm eq}$. In our models, we find agreement with the equipartition assumption to hold over the full simulation box, independent of the box size. Equipartition at the kpc scale, however, does not necessarily hold in the larger simulations. The widths of both the arm and inter-arm regions in the `R8 Arm` model are ~ 1 kpc. While the CR energy density varies by a factor of ~ 2 between the two regions, the magnetic field strength varies by more than an order of magnitude. Therefore, equipartition cannot always hold at the ~ 1 kpc when considering both of these regions.

3.3.4 Alternative Estimates of Magnetic Field Strength

In both the `R8` and `R8 Arm` models, we find that the CR and magnetic energy densities are approximately in equipartition averaged across the entire simulation box. However, at smaller scales we find that the equipartition estimate given by Equation 3.19 does not accurately reproduce the simulated magnetic field strength from the mock observations. Therefore, we will consider alternative approximations to estimate the magnetic field strength from synchrotron emission including estimates which rely on additional observations.

First, we consider a modification to the equipartition estimate on small scales making use of the fact that we find equipartition to hold at large scales. Therefore, we consider setting $e_{\rm c} = \langle e_{\rm c} \rangle = \langle B^2 \rangle / 8\pi$ where $\langle e_{\rm c} \rangle$ and $\langle B^2 \rangle$ represent box-averaged values determined as follows.

Beginning with Equation 3.17, we apply Equation 3.18 and substitute for $\gamma = 2\alpha + 1$ to find

$$e_c B^{\alpha+1} = A I_\nu \tag{3.22}$$

where

$$A = \frac{(2\alpha+1)(K_0+1)E_{\rm p}^{1-2\alpha}(\nu/2c_1)^\alpha}{2(2\alpha-1)c_2(\alpha)c_4(i)\ell_z}. \tag{3.23}$$

By taking both sides of Equation 3.22 to the power $2/(\alpha+1)$ and averaging, we find

$$\langle e_c^{\frac{2}{\alpha+1}} B^2 \rangle = \langle A^{\frac{2}{\alpha+1}} I_\nu^{\frac{2}{\alpha+1}} \rangle. \tag{3.24}$$

We have made the assumption that e_c is approximately constant. Additionally, we assume that the CR spectral slope is similar in each pixel across the simulation box and we can therefore use a single, average value of $\bar{\alpha}$ defined as

$$\bar{\alpha} = -\frac{\log(\langle I_{\nu_1} \rangle / \langle I_{\nu_2} \rangle)}{\log(\nu_1/\nu_2)} \tag{3.25}$$

where $\langle I_\nu \rangle$ is the spatial average across the simulation snapshot. Therefore, we can write

$$\langle e_c \rangle^{\frac{2}{\bar{\alpha}+1}} \langle B^2 \rangle = 8\pi \langle e_c \rangle^{\frac{\bar{\alpha}+3}{\bar{\alpha}+1}} = A^{\frac{2}{\bar{\alpha}+1}} \langle I_\nu^{\frac{2}{\bar{\alpha}+1}} \rangle. \tag{3.26}$$

Thus,

$$\langle e_c \rangle = \frac{A^{\frac{1}{\bar{\alpha}+3}} \langle I_\nu^{\frac{2}{\bar{\alpha}+1}} \rangle^{\frac{\bar{\alpha}+1}{\bar{\alpha}+3}}}{(8\pi)^{\frac{\bar{\alpha}+1}{\bar{\alpha}+3}}}. \tag{3.27}$$

Returning to Equation 3.22, we can use the average value of the CR energy density to find the local magnetic field by solving

$$\langle e_c \rangle B^{\bar{\alpha}+1} = A I_\nu \tag{3.28}$$

where B and I_ν in this equation are the local values. Solving for B results in the final expression,

$$B_{\mathrm{pred},\langle B^2 \rangle} = I_\nu^{\frac{1}{\bar{\alpha}+1}} \left[\frac{4\pi(2\bar{\alpha}+1)(K_0+1)E_{\mathrm{p}}^{1-2\bar{\alpha}}(\nu/2c_1)^{\bar{\alpha}}}{(2\bar{\alpha}-1)c_2(\bar{\alpha})c_4(i)\ell_z \langle I_\nu^{\frac{2}{\bar{\alpha}+1}} \rangle} \right]^{\frac{1}{\bar{\alpha}+3}}. \tag{3.29}$$

We compare this new prediction to the simulated magnetic field in the left panel of Figure 3.7. As in Figure 3.4, we show the comparison between the observationally predicted and simulated magnetic field strength in each pixel across all snapshots of the `R8` model. The

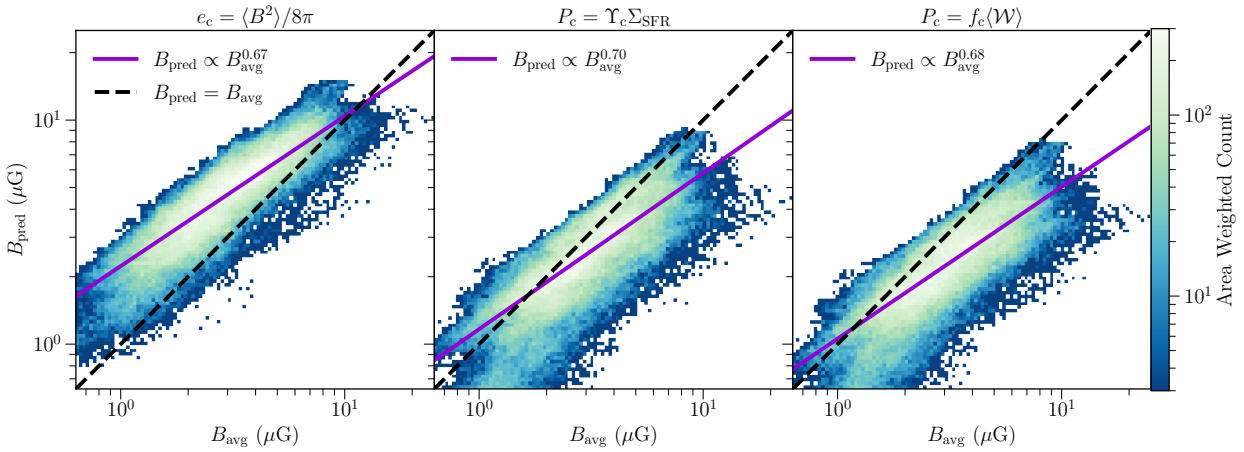

Figure 3.7: Each panel shows a two-dimensional histogram comparing one prediction of the magnetic field strength to the simulated, mass-averaged value. These distributions include all pixels across all R8 snapshots. The left panel estimates the magnetic field using Equation 3.29 where the total CR energy density is assumed to be a constant value determined by the average value of the equipartition field (Equation 3.19). The middle panel estimates the CR pressure as a fraction of the total ISM pressure as a function of Σ_{SFR}. The right panel estimates the CR energy density as a fraction of the total ISM weight (Equation 3.39). In all three panels, the black, dashed line shows $B_{pred} = B_{avg}$ and the purple line shows the best-fit power law to the distribution. In all three models we see an improvement in the scaling of B_{pred} relative to B_{avg} compared to the distribution shown in Figure 3.4.

best fit power law to this distribution is $B_{pred} \propto B_{avg}^{0.67}$. This is closer to a linear relationship when compared to the fit shown in Figure 3.4, representing an improvement to the original equipartition estimate from Equation 3.19.

This estimate still relies on the assumption of equipartition between the CR and magnetic energy density, although we make this estimate at a larger scale. A different method would be to estimate the CR energy density from alternative observables. For example, we could assume the total CR pressure is some fraction of the total ISM weight. From Ostriker & Kim (2022), the weight ($\mathcal{W}$) can be estimated as

$$\mathcal{W} = \frac{\pi G \Sigma_{gas}^2}{2} + \Sigma_{gas} \sigma_{eff} \sqrt{2 G \rho_{sd}} \tag{3.30}$$

where G is the gravitational constant and Σ_{gas} is the gas surface density. The combined stellar and dark matter density is given by ρ_{sd} and σ_{eff} represents the effective ISM velocity

dispersion. These quantities can all be estimated observationally. In our test, we take these values directly from the simulation snapshots.

The estimate in Equation 3.29 still relies on the assumption of equipartition between the CR and magnetic energy density, although we make this assumption only at large scales. A different method would be to estimate the CR energy density from alternative observables.

One alternative approach to estimating the midplane CR pressure, which corresponds approximately to the mass-weighted mean CR pressure in the simulation box, would employ observations that provide an estimate of the star formation rate per unit area, $\Sigma_{\rm SFR}$, which is assumed to be proportional to the energy injection rate from supernovae. The CR flux injected vertically to each half of the disk is $F_{\rm in} = 0.5\epsilon_{\rm c} E_{\rm SN} \Sigma_{\rm SFR}/m_\star$, where $E_{\rm SN} = 10^{51}$ erg is the energy released from a single SN event, $\epsilon_{\rm c} = 0.1$ is the fraction of SN energy converted into CR acceleration, and $m_\star$ is the mass of stars per SN ($95.5\,M_\odot$ in Kim & Ostriker 2017 from a Kroupa IMF). By approximating the midplane CR pressure as $P_{\rm c} \approx F_{\rm in}/(4v_{\rm eff,c})$, where $v_{\rm eff,c}$ is the effective CR propagation speed out of the midplane region (see also Equation 19 in Armillotta et al. 2022), we obtain the relation

$$P_{\rm c} = \Upsilon_{\rm c} \Sigma_{\rm SFR} \tag{3.31}$$

where $\Upsilon_{\rm c}$ is a theoretically-predicted CR feedback "yield,"

$$\Upsilon_{\rm c} \approx \frac{1}{v_{\rm eff,c}} \frac{\epsilon_{\rm c} E_{\rm SN}}{8 m_\star} \,. \tag{3.32}$$

We use the post-processed TIGRESS simulations from Hix et al. (in prep.) to relate $P_{\rm c}$ and $\Sigma_{\rm SFR}$ in different galactic environments and obtain a relation between $\Upsilon_{\rm c}$ and $\Sigma_{\rm SFR}$. These environments include the `R8`, `R8 Arm`, `R4`, and `R2` models from Kim et al. (2020); Kim et al. (2020), which have $\Sigma_{\rm gas} \sim 10 - 70$ M$_\odot$ pc^{-2} and $\Sigma_{\rm SFR} \sim 5 \times 10^{-3} - 1$ M$_\odot$ kpc^{-2} yr^{-1}. We find

$$\Upsilon_{\rm c} = 284 \text{ km s}^{-1} \left(\frac{\Sigma_{\rm SFR}}{0.01 \text{ M}_\odot \text{ kpc}^{-2} \text{ yr}^{-1}} \right)^{-0.23} \,. \tag{3.33}$$

The CR energy density is then $e_{\rm c} = 3\Upsilon_{\rm c}\Sigma_{\rm SFR}$ and the predicted magnetic field strength is

$$B_{\rm pred,SFR} = \left[\frac{(2\alpha+1)(K_0+1)E_{\rm p}^{1-2\alpha}(\nu/2c_1)^{\alpha}}{6(2\alpha-1)c_2(\alpha)c_4(i)}\frac{I_\nu}{\ell_z\Upsilon_{\rm c}\Sigma_{\rm SFR}}\right]^{\frac{1}{\alpha+1}}. \tag{3.34}$$

Here, $\Sigma_{\rm SFR}$ is the average value over the simulation box. This prediction for the magnetic field strength is shown in the middle panel of Figure 3.7. The best fit power-law of this distribution gives $B_{\rm pred} \propto B_{\rm avg}^{0.70}$.

Alternatively, we could also assume the midplane CR pressure is some fraction of the total ISM weight. A simple estimate of the weight in regions of galaxies where the gas disk is thinner than the stellar disk is

$$\mathcal{W} = \frac{\pi G\Sigma_{\rm gas}^2}{2} + \Sigma_{\rm gas}\sigma_{\rm eff}\sqrt{2G\rho_{\rm sd}}, \tag{3.35}$$

where G is the gravitational constant and $\Sigma_{\rm gas}$ is the gas surface density. The combined stellar and dark matter density is given by $\rho_{\rm sd}$ and $\sigma_{\rm eff}$ represents the effective vertical velocity dispersion. These quantities can all be estimated observationally.

For our test, we take the values directly from the simulation. In the `R8` model, $\rho_{\rm sd} = 0.0924\ M_\odot\ {\rm pc}^{-3}$. We estimate $\sigma_{\rm eff} = (\Sigma_{ijk}P_{\rm tot}/\Sigma_{ijk}\rho)^{1/2}$ where Σ_{ijk} represents the sum over the whole simulation box. Here we take the total pressure as the sum of the thermal and effective turbulent pressure, $P_{\rm tot} = P_{\rm th} + P_{\rm turb}$. In reality, the total pressure includes an additional term, the Maxwell stress, representing the magnetic pressure and tension. However, as this value is not accessible observationally we include only $P_{\rm th}$ and $P_{\rm turb}$. The exclusion of the magnetic pressure term results in at most a 10% reduction in $\sigma_{\rm eff}$ across the `R8` snapshots, so does not have a significant effect on our final results.

Ostriker & Kim (2022) show that, in the TIGRESS environments, the weight is balanced by the sum of the midplane thermal, kinetic, and magnetic pressure, such that $\mathcal{W} \approx P_{\rm tot} = \Upsilon_{\rm tot}\Sigma_{\rm SFR}$, where $\Upsilon_{\rm tot}$ is the combined feedback yield from thermal, kinetic, and magnetic components. We define the midplane CR pressure as a fraction of the total weight $P_{\rm c} = f_{\rm c}\mathcal{W}$.

Since $P_{\rm c} = \Upsilon_{\rm c}\Sigma_{\rm SFR}$ and $\mathcal{W} \approx \Upsilon_{\rm tot}\Sigma_{\rm SFR}$, we estimate the fraction as $f_{\rm c} = \Upsilon_{\rm c}/\Upsilon_{\rm tot}$. Ostriker & Kim (2022) fit $\Upsilon_{\rm tot}$ as a function of $\mathcal{W}$ (see Equation 25c), and find

$$\Upsilon_{\rm tot} = 7240 \text{ km s}^{-1}(\mathcal{W}/k_B)^{-0.21} \tag{3.36}$$

where $\mathcal{W}/k_B$ is in cm^{-3} K. To find the relation between $\Upsilon_{\rm c}$ and $\mathcal{W}$, we again use the post-processed TIGRESS simulations from Hix et al. (in prep.). The fit gives

$$\Upsilon_{\rm c} = 6310 \text{ km s}^{-1}(\mathcal{W}/k_B)^{-0.29}, \tag{3.37}$$

which results in a value of

$$f_{\rm c} = \frac{\Upsilon_{\rm c}}{\Upsilon_{\rm tot}} \approx 0.9(\mathcal{W}/k_B)^{-0.08}. \tag{3.38}$$

Substituting $P_{\rm c} = f_{\rm c}\mathcal{W}$, equivalently $e_{\rm c} = 3f_{\rm c}\mathcal{W}$, into Equation 3.17 results in a predicted magnetic field strength of

$$B_{{\rm pred},\mathcal{W}} = \left[\frac{(2\alpha+1)(K_0+1)E_{\rm p}^{1-2\alpha}(\nu/2c_1)^{\alpha}}{6(2\alpha-1)c_2(\alpha)c_4(i)}\frac{I_\nu}{\ell_z f_{\rm c}\langle\mathcal{W}\rangle}\right]^{\frac{1}{\alpha+1}}, \tag{3.39}$$

where $\langle\mathcal{W}\rangle$ is the average weight across the simulation box. We evaluate Equation 3.39 for each of the `R8` snapshots and plot the distribution in the right panel of Figure 3.7. As with the alternate evaluations given by Equation 3.29 and Equation 3.34, we see a scaling that is closer to linear of $B_{\rm pred} \propto B_{\rm avg}^{0.67}$.

The three alternative estimates show similar power-law relationships between $B_{\rm pred}$ and $B_{\rm avg}$ at the 8 pc scale, all of which are closer to linear than the unmodified equipartition estimate. Therefore, each of these new methods may provide a better estimate of the small-scale magnetic field strength, with caveats that we will discuss in Section 3.4.3. The overall normalization of $B_{\rm pred}$, however, differs based on the estimator used for e_c.

In each of the three alternative estimates, $B_{\rm pred}$ would better match $B_{\rm avg}$ if we were to include an additional constant in front of Equation 3.29, Equation 3.39, and Equation 3.34.

This value would vary between roughly 0.7 for Equation 3.29 to 1.5 for Equation 3.39. It is not clear, however, that this numerical prefactor would be the best value to use in all environments. If we had good observational constraints on the magnetic field strength through alternative methods, for example in the Milky Way, we might better constrain the normalization factor.

3.3.5 Polarization

In addition to probing the magnetic field strength, synchrotron observations also provide a way to determine the orientation of magnetic fields when we consider polarized emission. We evaluate the accuracy with which the magnetic field direction can be extracted from the Stokes parameters Q_ν and U_ν. To do so, we find the polarization angle, φ, using equation Equation 3.11 for each of the `R8` snapshots. We rotate this angle by 90° to recover an estimate of the magnetic field direction. Then, we compare this to the angle made by the true magnetic field in the plane of the sky. We estimate the average angle of the simulated magnetic field as

$$\varphi_B = \arctan\left(\frac{B_{\mathrm{y,avg}}}{B_{\mathrm{x,avg}}}\right) \tag{3.40}$$

where $B_{\mathrm{x,avg}}$ and $B_{\mathrm{y,avg}}$ are the mass-weighted average x and y components of the magnetic field along the line of sight. Note that we do not include Faraday rotation in our calculation, just polarized emission.

In Figure 3.8, we show the synchrotron intensity at 1.5 GHz for one snapshot of the `R8` model (also shown in Figure 3.3). Projected onto the snapshot, we show the magnetic field direction (Equation 3.40) with black arrows. We also include the angle of the magnetic field as estimated by the Stokes parameters with white bars. This value is ambiguous up to 180° so does not have a fixed direction. Qualitatively, we see that the magnetic field is generally aligned with the values estimated by polarization, as would be expected. However,

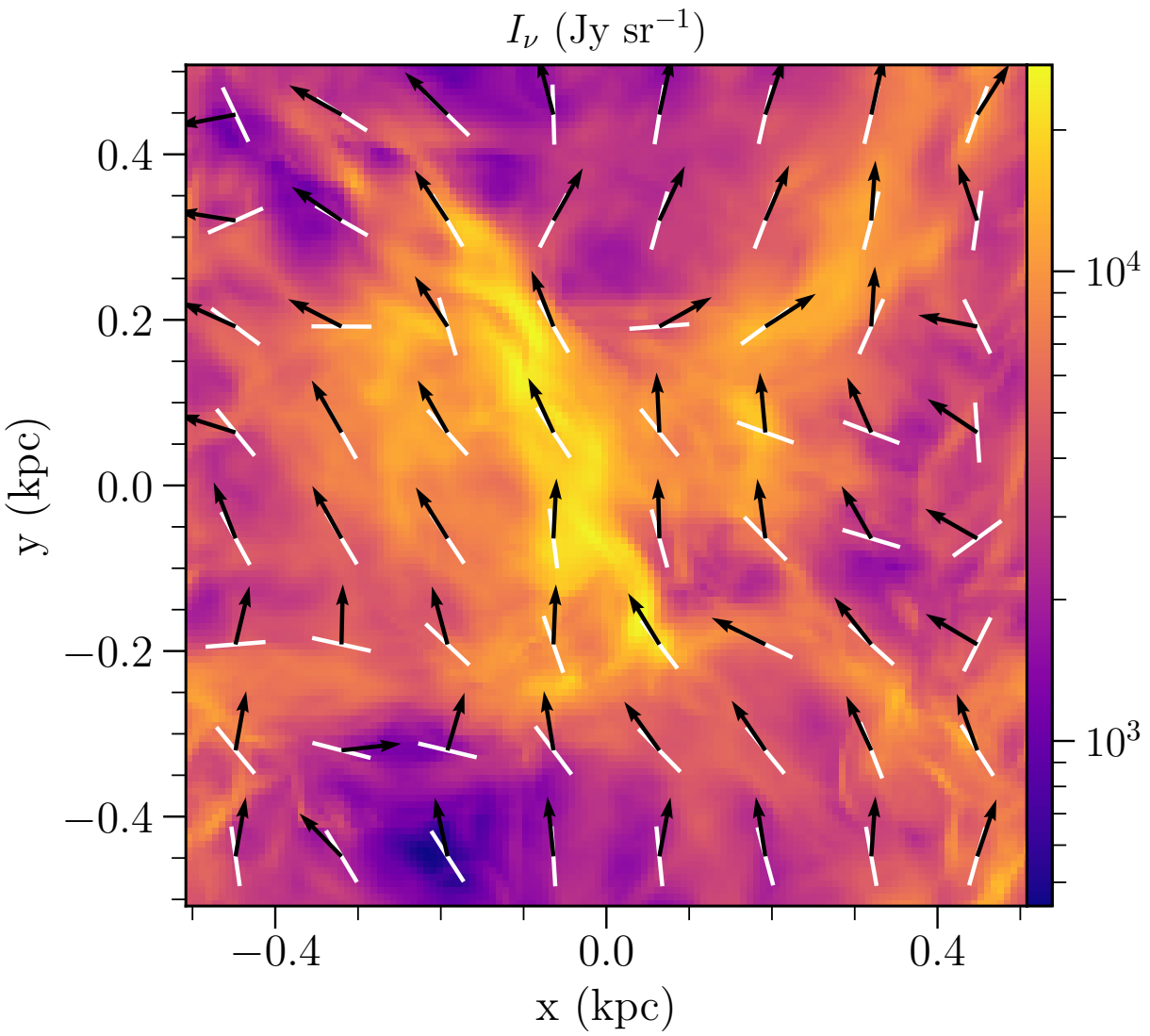

Figure 3.8: Synchrotron emission at 1.5 GHz from one snapshot of the `R8` model. The white bars represent the magnetic field direction estimated from polarization measurements. This is given by Equation 3.11 rotated by 90°. The black arrows represent the mass-weighted average magnetic field direction projected into the x-y plane (Equation 3.40).

the two angles are not strictly aligned, likely due to the variations in the magnetic field and synchrotron emission along the line of sight.

In Figure 3.9, we compare the true direction of the magnetic field to the value estimated using Equation 3.11 across all `R8` snapshots in a two-dimensional histogram. Because the polarization angle is ambiguous up to 180°, we limit both angles to between 0 and 180°. From the distribution in Figure 3.9, we see that the observational estimate does a good job

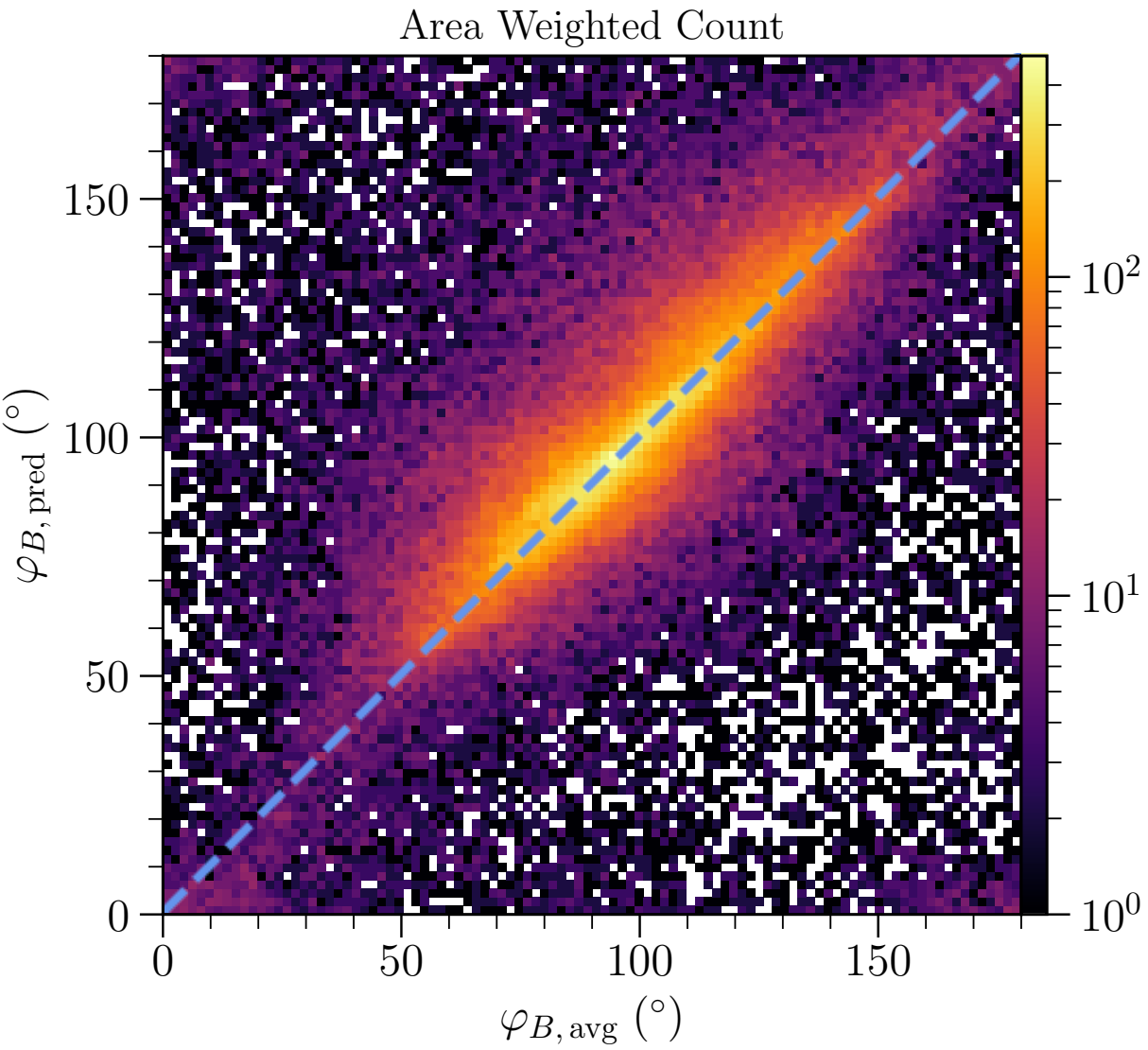

Figure 3.9: Comparison of the mass-weighted average magnetic field direction projected into the x-y plane ($\varphi_{B,avg}$) to the observationally estimated magnetic field direction $\varphi_{B,est} = \varphi + 90°$ (Equation 3.11). The blue dashed line represents $\varphi_{B,avg} = \varphi_{B,est}$. Overall, we see good agreement between $\varphi_{B,avg}$ and $\varphi_{B,est}$.

of extracting the true magnetic field direction. Quantitatively, in 70% of the pixels, $\varphi_{B,est}$ is within 15° of $\varphi_{B,avg}$.

3.4 Discussion

3.4.1 Modeling Radio Emission

Producing mock synchrotron emission, as we do in this chapter, requires both a spectrally resolved CRE population, and the magnetic field strength. This has also been done using other CR transport simulations. Ponnada et al. (2024) produces synchrotron emission based on the simulations presented in Hopkins et al. (2022a), and Werhahn et al. (2021a,b) include synthetic synchrotron radiation along with their other results. Additionally, Chiu et al. (2024) use the method described in Werhahn et al. (2021b) to generate radio synchrotron spectra and polarization for a simulation of an edge-on galaxy.

Modeling of CR transport has also been applied to many extragalactic radio observations (e.g. Mulcahy et al., 2016; Schmidt et al., 2019; Stein et al., 2023; Heesen et al., 2023). These models are generally greatly simplified compared to transport schemes in simulations due to a lack of knowledge about the local ISM properties necessary for more complex transport. The primary CR transport mechanism included in modeling observations is diffusion, generally with a diffusion coefficient that depends only on energy, although some models do also consider advection. These models may also include energetic losses through synchrotron and IC interactions.

We know from our CR simulations that the dominant transport mechanism varies between advection, streaming, and diffusion depending on the ISM phase (Armillotta et al., 2024). Also, the diffusion parameter can vary significantly based on local gas properties. Therefore, simplified models which ignore these mechanisms may not accurately reproduce the underlying CRE distribution. CREs with energies between approximately 100 MeV - 10 GeV are responsible for emission in the GHz range, and we know the CR spectral index varies significantly in this range, as observed directly and reproduced in models (Padovani et al., 2021; Bracco et al., 2024). Therefore, to model radio emission accurately, it is nec-

essary to include an energy-dependent CRE spectral slope, which is not always done when interpreting observations (Padovani et al., 2021).

3.4.2 Equipartition at Different Scales

In both the `R8` and `R8 Arm` models, we find that the equipartition estimate of magnetic field strength is reasonable when considering the full simulation boxes. This is not surprising, as our simulations reproduce solar neighborhood conditions, and the CR and magnetic energy density are locally in equipartition. However, we do find significant disagreement with the equipartition estimate at the resolution scale of our simulations. This is consistent with expectations, as both observational and theoretical work has predicted that equipartition should not hold below $\sim$ 1 kpc (e.g. Stepanov et al., 2014; Seta & Beck, 2019). In our simulations, this disagreement is due to the fact the CR energy density is quite uniform across the x-y plane (due to rapid CR diffusion), while the magnetic field has much more significant variation.

We note that the `R8 Arm` models are not in equipartition if we consider smaller patches of the simulation of the same size as the `R8` model ($\sim$ 1 kpc). This is because equipartition on the box scale is determined by a competition between CR injection by SNe and loss by advection and diffusion (which is relatively independent of box size), while the uniformity of the CRs in the plane of the disk is a consequence of the lack of any background gradients and rapid CR diffusion. Our simulations cannot therefore directly predict the scale below which equipartition breaks down. Large scale variations in the CR energy density are observed as a function of galactic radius. It is likely this large-scale spatial gradient that determines the scale below which equipartition breaks down in Milky Way-like galaxies.

3.4.3 Accuracy of Alternative Estimates

In this chapter, we presented three alternative methods which might be used instead of equipartition between CR and magnetic energy density to estimate the magnetic field

strength in galaxies. These methods are particularly important for inferring small-scale magnetic field structure from synchrotron observations, where we have shown the traditional equipartition estimate breaks down. All three estimates amount to the same modification to the original equipartition estimate, i.e. that the CR energy density is constant on small scales. In each case, $B_\perp = AI_\nu^{\frac{1}{\alpha+1}}$, and the primary difference is in how the constant A is determined.

If we knew the scale over which equipartition between magnetic and CR energy density holds, then we would have an implementable observational model for estimating magnetic field strength from radio observations. We could take the CR energy density to be a constant value using any of the three alternative estimators we proposed in Section 3.4.3. From our simulation results, however, we clearly cannot constrain this length scale, as we find the CR energy density to be constant on the simulation box scale independent of the size of the box. One could plausibly average over a length scale (ℓ) comparable to the local radius in a galactic disk. To determine the appropriate averaging scale, however, we would need to use results from global models of CR transport.

In all the extragalactic magnetic field measurements considered here, there is uncertainty in the overall normalization of the predicted magnetic field strength compared to the true value. While all three methods have similar scaling between $B_{\rm pred}$ and $B_{\rm avg}$, they differ in magnitude by approximately a factor of two. These estimates, as well as the original equipartition estimate, rely on multiple free parameters to set the magnitude of the predicted magnetic field. For example, all estimates are a function K_0 (the ratios of CR proton energy to electron energy) and ℓ_z (the vertical length scale for emission), which are defined by observational measurements, but are not necessarily fixed values across all environments. In our alternative estimates, we introduce further uncertainty through our approximations of the yield which we determine by fitting simulation results. Furthermore, introducing additional observations adds to the uncertainty of the final estimate, although this is not

likely to be the dominant source of error. Therefore, we cannot conclude if one alternative estimate would perform significantly better when applied to real observations.

Additionally, our tests in this work are based on simulations representing only one environment, i.e. conditions similar to the solar neighborhood. Therefore, these results should not be extrapolated to galaxies with significantly different conditions compared to Milky Way-like spirals until we expand our numerical experiments to simulations spanning a wider range of environments. We will consider one alternative environment in Chapter 4.

3.5 Conclusions

Our simulations include a spectrally resolved CRE distribution along with realistic small-scale magnetic field structure, allowing us to produce synthetic synchrotron emission. We find that the spatial structure of the synchrotron emission is dominated by the magnetic field distribution, but the CR spectrum determines the radio spectral index. We compare the directly observable CRE spectrum to that which can be extracted from radio observations and find the two to be consistent. This supports the observational method of indirectly determining the CR spectrum from radio observations.

Almost all measurements of magnetic field strength in extragalactic sources rely on the equipartition estimate (see Tabatabaei et al., 2008; Heesen et al., 2009; Soida et al., 2011; Mora & Krause, 2013; Mulcahy et al., 2016; Mora-Partiarroyo et al., 2019; Stein et al., 2023, for just a few examples). In our simulations, we find that this assumption produces accurate estimates of the magnetic field strength at large scales. However, as higher-resolution radio observations become possible with next generation telescopes, there may be a push to apply the equipartition estimate at smaller scales. As theorized in other work (see e.g. Stepanov et al., 2014; Seta & Beck, 2019), we find that the equipartition assumption between magnetic and CR energy densities does not hold below kpc scales. We propose alternative estimators of

the CR energy density, which we find to improve the estimate of the magnetic field strength at small scales over the equipartition assumption.

Chapter 4

Inner Galaxy Model

4.1 Introduction

So far, we have only modeled CR transport in TIGRESS simulations representative of solar neighborhood conditions. We now consider an environment with different characteristics to better understand how CR transport and spectral evolution may change. To do so, we post-process snapshots of the TIGRESS `R2` model approximating conditions in the inner galaxy at a galactic radius of 2 kpc. This model has higher gas density, velocity, and magnetic field strength compared to the `R8` model, which we expect to affect the relative impact of the CR transport and energetic loss mechanisms resulting in a different final CR distribution and spectrum.

In Section 4.2 we describe the updates to the CR transport scheme necessary for post-processing the inner galaxy environment. We present analysis of the post-processed models in Section 4.3 reproducing many of the results included in Chapter 2 and Chapter 3. We compare our results both to observations and other models of CR transport in Section 4.4, and summarize our results in Section 4.5.

4.2 Methods

The R2 model has much higher surface density and star formation rate than the R8 model, with an average $\Sigma_{\rm gas} \approx 74\ M_\odot\ {\rm pc}^{-2}$ and $\Sigma_{\rm SFR} \approx 1.1\ M_\odot\ {\rm kpc}^{-2}\ {\rm yr}^{-1}$ compared to $\Sigma_{\rm gas} \approx 11\ M_\odot\ {\rm pc}^{-2}$ and $\Sigma_{\rm SFR} \approx 0.0051\ M_\odot\ {\rm kpc}^{-2}\ {\rm yr}^{-1}$ in the R8 model (Kim et al., 2020). The simulation box is also smaller, with $L_x = L_y = 512$ pc and $L_z = 3584$ pc and a resolution of $\Delta x = 4$ pc. The transport of a single CR fluid representing 1 GeV protons in the R2 model was previously modeled by Armillotta et al. (2022) and further analysis of this environment will be included in Hix et al. (in prep).

To account for the change in environment, we must make a few minor modifications to the CR transport scheme described in Chapter 2. All of the CR transport and energetic loss mechanisms are determined self-consistently based on local gas and CR properties except for the IC losses, which we set with a fixed estimate of the radiation energy density. As the radiation field described in Section 2.C is scaled to match solar neighborhood values, we must make a different approximation for the inner galaxy environment. This estimate is described in detail in Section 4.A. Additionally, we consider only one definition of the perpendicular scattering coefficient, $\sigma_\perp = 10 \times \sigma_\parallel$, and use only the fiducial injection spectrum with slope $s = -2.3$.

As described in Chapter 2, we freeze the background gas and post-process the snapshots with the CR transport scheme until the CR distribution reaches a steady state. Unlike for the R8 models, however, we do not include the additional MHD relaxation step. In the R8 model, we did not see a significant change in the CRE spectrum before and after MHD relaxation. In the R2 model, the advection velocity is considerably higher than in R8 ($\sim$60 compared to $\sim$15 km/s). Without ongoing input of SN energy, it is not be possible to maintain a realistic advection speed during even a short relaxation step. This would affect other MHD properties as well as CR transport and the resulting measured spectrum. Therefore, we omit the relaxation step for this model. Although the spatial distribution of the CREs in the R8 models changed after MHD relaxation, this difference did not qualitatively affect our

conclusions about the CRE spectrum or comparisons to observations. Therefore, we can still learn about CR transport in the inner galaxy environment without this additional step.

Using the slightly altered method, we post-process six snapshots from the R2 simulation between the times of $30-80$ Myr. Separately, we analyze three snapshots between $100-120$ Myr. These snapshots are separated because there is a significant drop in $\Sigma_{\rm SFR}$ in the original TIGRESS model between $80-100$ Myr by a factor of ~ 5. Therefore, the IC losses are much larger in the six early-time snapshots compared to the latter three, and the resulting CRE spectra are significantly different between the two times. In the following sections we analyze the six high-$\Sigma_{\rm SFR}$ snapshots but present some of the results for the later time snapshots in Section 4.B.

4.3 Results

We present analysis of the R2 post-processed simulations to produce results analogous to those presented in Chapter 2 for the R8 models. Additionally, we produce synthetic synchrotron emission as in Chapter 3 to test the traditional equipartition estimate of magnetic fields in this new environment.

4.3.1 CR Distribution

First, we show vertical ($y = 0$) and horizontal ($z = 0$) slices through the $t = 30$ Myr snapshot of the R2 model in Figure 4.1 including MHD (n_H, T, $|\mathbf{v}|$, $|\mathbf{v}_{\rm A,i}|$, $|\mathbf{B}|$) and CR ($e_{\rm c}$, $|\mathbf{F}_c|$, $\sigma_{\parallel}$) variables for the lowest momentum CRE bin ($p \sim 2$ GeV/c). In the first panel, we plot the star particles over the background n_H slice. We see that there is a high density of these particles, and all are limited to within approximately $|z| < 100$ pc.

Compared to the solar neighborhood environment, the gas in the R2 model is denser, hotter, and the magnetic fields are stronger, with $|\mathbf{B}|$ reaching values greater than 100 μG. The magnitude of the gas velocity, $|\mathbf{v}|$, is between 100-1000 km/s in most of the simulation

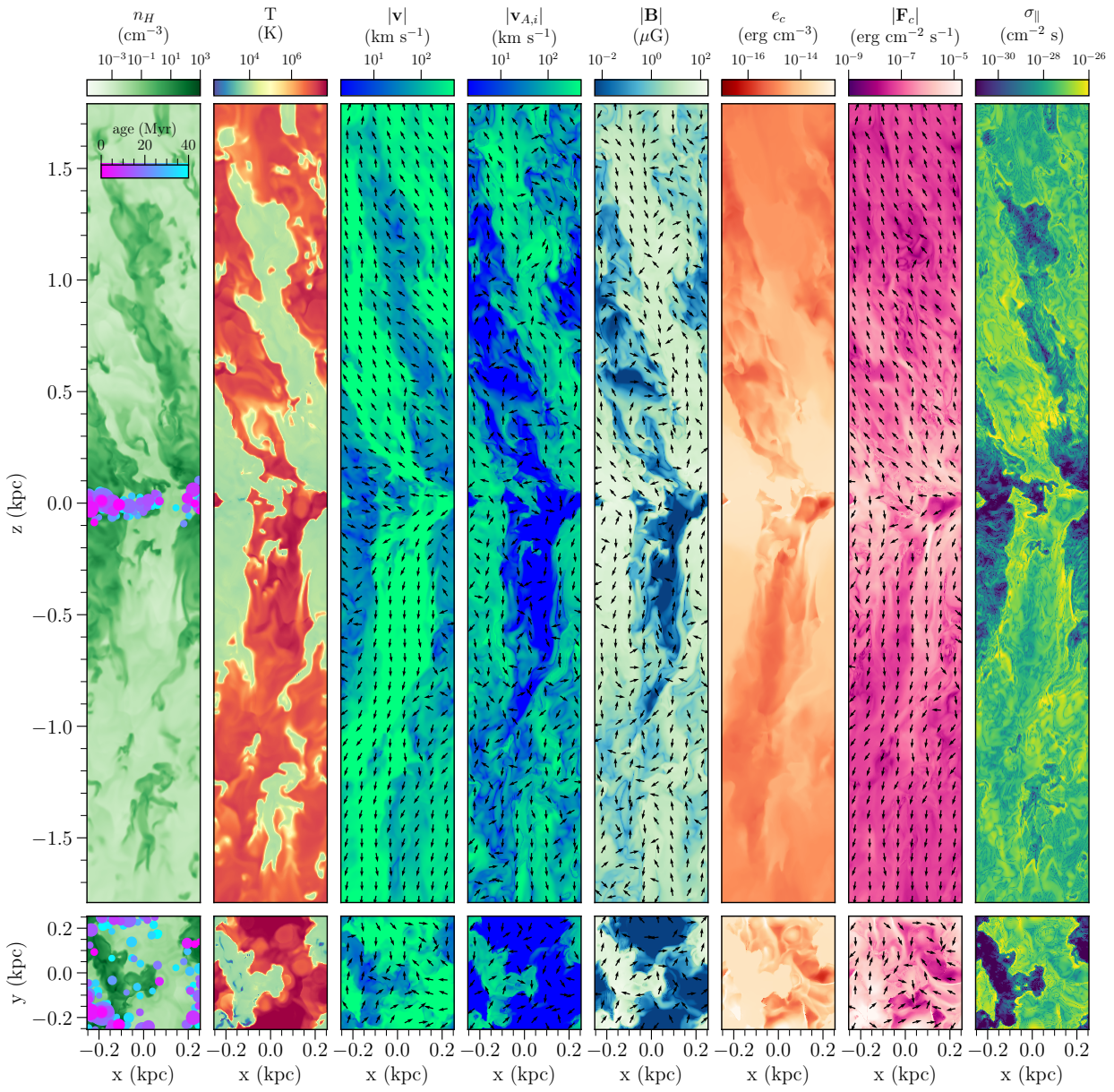

Figure 4.1: Vertical (through $y = 0$) and horizontal (through $z = 0$) slices of MHD and CR variables from the `R2` snapshot at $t = 30$ Myr. From left to right, the first five slices show number density of hydrogen (n_H), temperature (T), magnitude of the gas velocity ($|\mathbf{v}|$), magnitude of the ion Alfvén velocity ($|\mathbf{v}_{\rm A,i}|$), and magnitude of the magnetic field ($|\mathbf{B}|$). The final three slices show energy density (e_c), flux magnitude ($|\mathbf{F}_c|$), and scattering coefficient ($\sigma_\parallel$) of CREs with momentum $p \sim 2$ GeV/c. The arrows overlaid on the slices of gas velocity, Alfvén speed, magnetic field, and flux magnitude indicate the projected directions of the gas velocity, CR streaming velocity, magnetic field, and CR flux respectively.

box, and is significantly larger than the streaming velocity, $|\mathbf{v}_{\rm A,i}|$, in the hot, low-density outflows which make up much of the gas. The CR flux, $\mathbf{F}_c$, is almost entirely aligned with the gas velocity in these regions, showing that advection dominates the CR transport. Only in the warm/cold, high-density gas is $|\mathbf{v}_{\rm A,i}|$ larger than $|\mathbf{v}|$. These regions also have smaller values of $\sigma_{\|}$, suggesting that diffusion and streaming are important transport mechanisms compared to advection.

Considering the horizontal midplane slice, we can clearly see two distinct gas regimes. In the high-density warm/cold gas, the magnetic field, and therefore the streaming velocity, is large while the gas velocity is comparatively low. Within these regions, the CRs are highly diffusive and $e_{\rm c}$ is nearly constant. On the other hand, in the hot, low-density gas the magnetic field is smaller by more than four orders of magnitude and the streaming velocity is correspondingly small. The CR transport is dominated by advection leading to more variation in $e_{\rm c}$. Although this phase separation is also clear in the `R8` model, the differences between the two regimes are not as extreme.

The CR energy density is generally smoother than the gas density, particularly in the densest gas. However, there is more structure in $e_{\rm c}$ in the `R2` model compared to the `R8` model (Figure 2.1). If we were able to include the MHD relaxation step after the initial post-processing, the CR energy density distribution would be significantly smoother as the magnetic field and velocity at inerfaces would reorient, allowing CRs are able to escape from the warm, dense gas.

In Figure 4.2, we present vertical profiles of the horizontally-averaged CRE spectral flux (j_e) within each momentum bin. For all five of the momentum bins, there is a noticeable peak in the CRE spectrum at $z \sim 0$, generally corresponding to the CR injection region. If we allow the MHD variables to evolve, even for a very short time, the peaks in the CRE profiles are reduced as CRs escape from dense gas.

The `R2` CRE profiles show decreasing scale height with CR momentum, unlike in the `R8` model which had increasing CRE scale height at higher momenta (Figure 2.4). The lowest

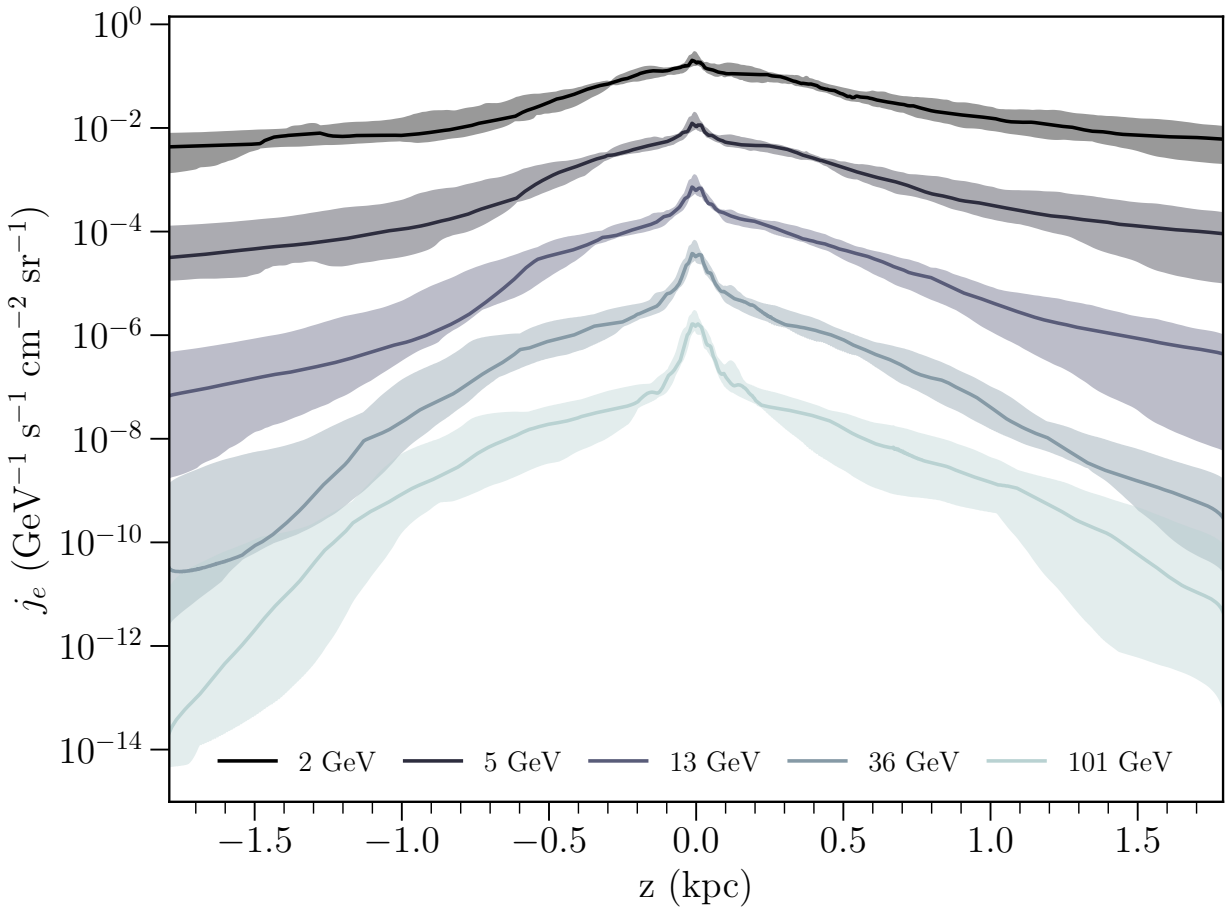

Figure 4.2: Horizontally and temporally averaged vertical profiles of the CRE spectrum, j_e, in each momentum bin labeled by the value of *pc*. The shaded area covers the 16th and 84th percentiles from temporal variations while the central line represents the median value.

energy CREs here have a much flatter vertical distribution compared to the highest energy CREs. Therefore, the `R2` models have a steeper, rather than shallower, CRE spectrum as a function of height above the midplane. This result is consistent with direct observations of edge-on galaxies which find the radio spectral index to steepen with distance from the midplane (e.g. Stein et al., 2023).

4.3.2 CR Transport

In Figure 4.3, we show the value of the CR mean free path, $\ell = 1/(c\sigma_{\|})$ and $\sigma_{\|}$ for the `R2` model compared to the `R8` model. As in Figure 2.2, these values are presented for three of

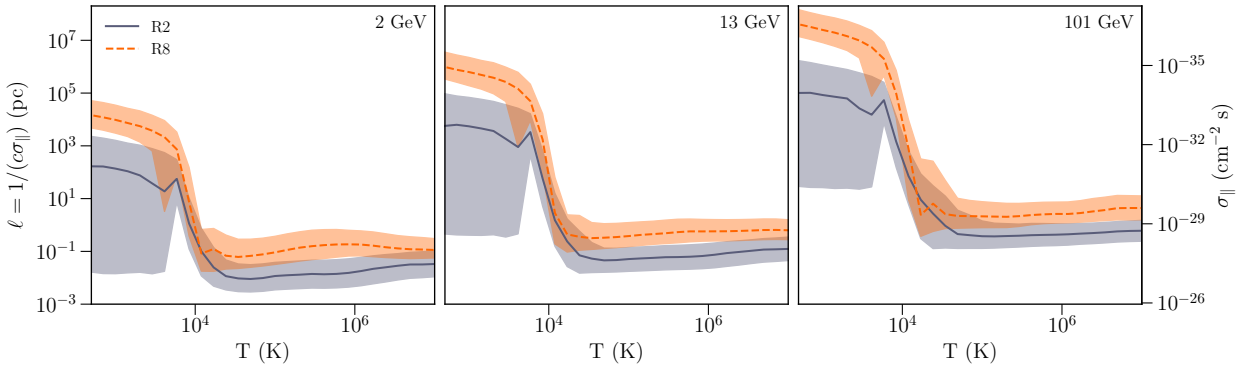

Figure 4.3: CR mean free path, $\ell = 1/(c\sigma_\parallel)$ and $\sigma_\parallel$ as a function of gas temperature, T. The lines represent the median value across all snapshots, while the shaded regions represent the 16th-84th percentiles. Each panel represents a different CR momentum bin, $pc = 2$, 13, and 101 GeV. In each bin, we include the distribution of ℓ and $\sigma_\parallel$ for both the `R2` (gray, solid lines) and `R8` (orange, dashed lines) models.

the CR momentum bins as a function of the gas temperature, T. For both of the simulated environments, the dominant damping mechanism at low temperatures is IN while at high temperatures it is NLL and there is a change in the median $\sigma_\parallel$ by more than four orders of magnitude between the two regimes. In the `R2` model, however, there is significantly more variance in the value of $\sigma_\parallel$ at low temperatures, as there is very little cold gas in the post-processed snapshots.

The scattering coefficient in the inner galaxy model is nearly two orders of magnitude larger in the warm/cold (high density) gas, and one order of magnitude larger in the hot (low density) gas, compared to the solar neighborhood model (see also Armillotta et al. (2022) for a comparison of the mean free path as a function of density in the `R2` and `R8` models). Therefore, the CRs in the `R2` model behave less diffusively overall, although the diffusion rate is still high at low temperatures, especially for the higher energy CREs.

The `R2` model has higher density, magnetic field strength, and radiation field (correlated with star formation rate) compared to the solar neighborhood model. Therefore, all of the CRE energetic loss mechanisms (described in detail in Section 2.C) are more significant. The IC losses in particular are much larger, as the radiation field in the `R2` model is greater by a factor of ~ 200 averaged across the post-processed snapshots when compared to the `R8` model.

We show the horizontally and temporally averaged vertical profiles of $[dE/dt]_j$ in Figure 4.4. The IC losses dominate at all CRE energies and throughout the entire simulation region due to the greater radiation field. As in the solar neighborhood model, the synchrotron, ionization, and bremsstrahlung losses have similar magnitudes in lowest momentum bin, but as energy increases the synchrotron losses become more dominant.

We calculate the CR loss timescale as defined in Equation 2.36 and present this value in Figure 4.5 compared to both the transport and the diffusion times, defined in Equation 2.37 and Equation 2.38 respectively. The loss timescale is minimized at $z = 0$ where the energetic loss rate is greatest. Similarly, the local diffusion time is minimized in the midplane where there is the most gas with low values of $\sigma_{\parallel}$. The transport time has a peak at the midplane but is relatively constant in magnitude across all z. In the `R8` model, there is a clear region of warm gas in the midplane where gas velocity is low, and diffusion dominates the CR transport (Figure 2.1). In the `R2` model, however, there is not as clear of a separation, and there are hot outflows originating even from the midplane (Figure 4.1). Therefore, the relative contributions of advection, streaming, and diffusion to the overall CR transport are more consistent across all z.

Unlike in the `R8` model (see Figure 2.6), the loss timescale in Figure 4.5 is comparable to the transport time scale at the midplane for the lowest energy CREs, and is shorter than the transport time for almost all z in the three highest CRE momentum bins. This is primarily due to the greater IC losses. Because the loss timescale is much shorter, we would expect the steepening of the CRE spectrum in these post-processed snapshots to be primarily due to energetic losses rather than energy-dependent transport. Additionally, because IC losses dominate at all energies, we would expect the change in the CRE slope to be relatively constant with CRE energy rather than varying as a function of energy, which would be the case if different loss mechanisms dominated at different energies.

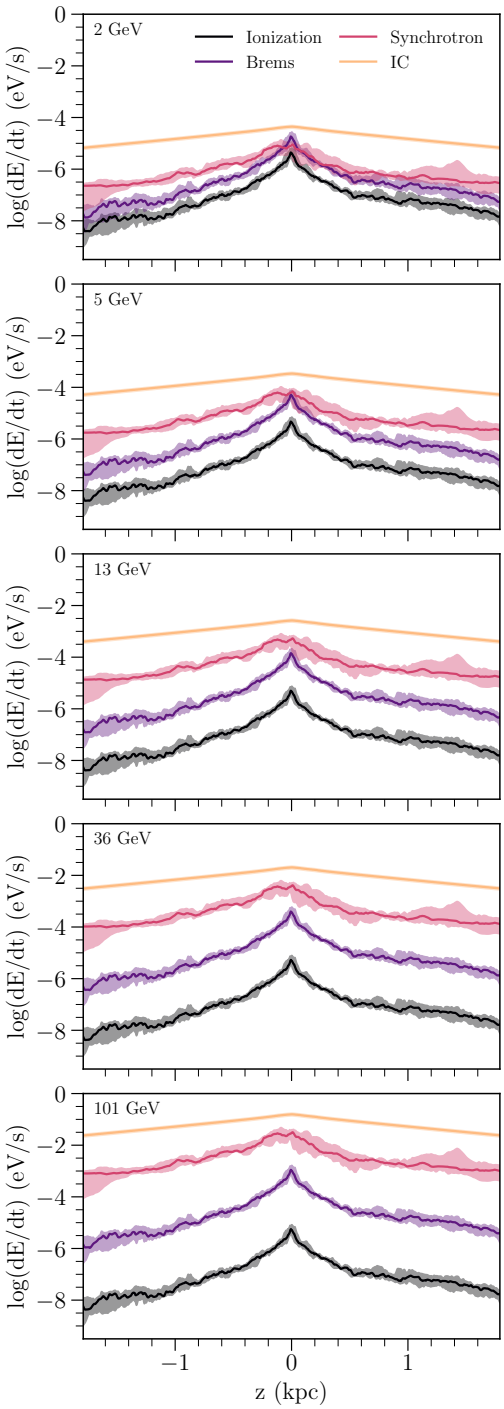

Figure 4.4: Horizontally and temporally averaged vertical profiles of CRE energy loss rates dE/dt. Different colors represent different loss mechanisms: ionization (black), bremsstrahlung (purple), synchrotron (magenta), and IC (light orange). Each panel shows results for CREs within a different momentum bin. At each z, the solid lines represent the median value of the horizontally averaged $\langle dE/dt \rangle$ evaluated across all snapshot times. The shaded regions cover the 16th-84th percentiles.

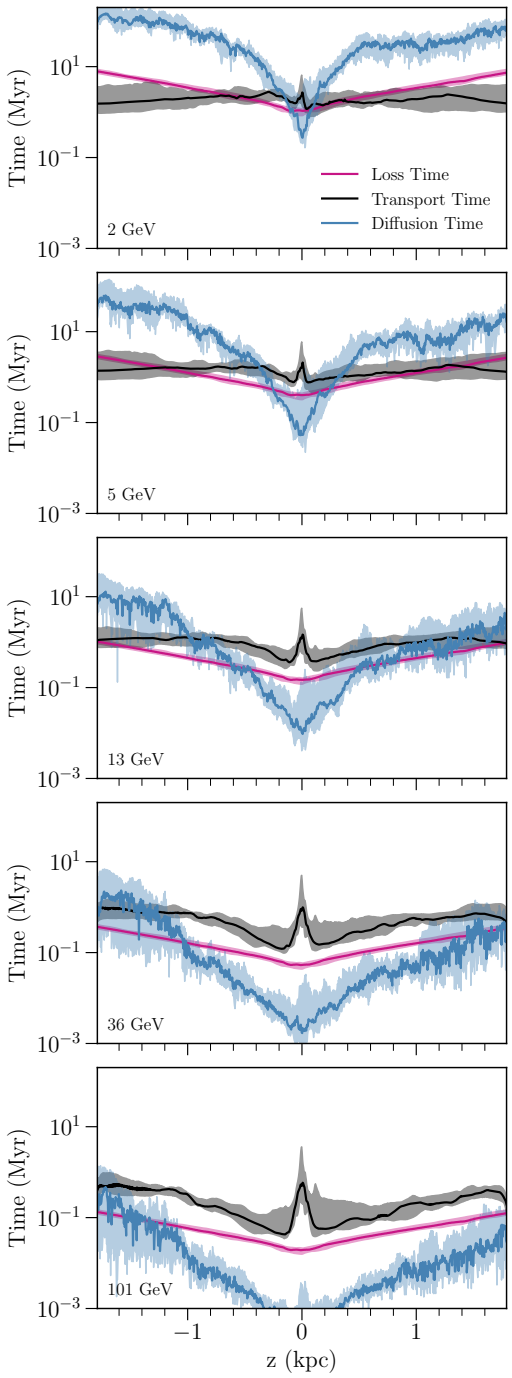

Figure 4.5: Horizontally and temporally averaged vertical profiles of the timescale for energy loss (magenta) in comparison to the global transport (black) and diffusion (blue). These timescales are defined in Equation 2.36, Equation 2.37, and Equation 2.38, respectively. Each panel presents results for CREs within a given momentum bin. At each z, the solid line represents the median value of the horizontally averaged $\langle t \rangle$ evaluated across all snapshots. The shaded regions show the 16-84th percentile values across all snapshots.

4.3.3 CR Spectrum

We present the simulated CRE and CR proton spectra (Equation 2.35) in Figure 4.6 limited to gas with $T < 3 \times 10^4$ K and $|z| < 150$ pc. The CRE spectra steepen as a function of height (Figure 4.2), so if were to include a wider range of z, we would see a steeper average spectrum with greater variation within each momentum bin. Our results do not change significantly, however, if we include $|z| < 300$ pc as we did with the `R8` simulations. We select only the warm/cold gas to remove the injection regions. Raising the temperature limit increases the variation in the final spectrum, and makes the final spectrum slightly less steep, but does not significantly change the results.

We fit both spectra with a power-law distribution and find the evolved CRE spectrum to be much steeper than the directly observed value in the solar neighborhood, with a best fit spectral index of -3.5. This is roughly consistent with the analytic prediction in an environment with dominant IC losses. If CRs are injected with a spectral distribution $f(E) \propto E^{\gamma}$, and are subject only to energetic losses with $dE/dt \propto E^2$, the steady-state CR spectrum would be $f(E) \propto E^{\gamma-1}$.

The CR protons, unlike the electrons, have approximately the same spectral index as in the solar neighborhood with a power-law slope of -2.65 (see Figure 2.13). Because the steepening of the CR proton spectrum is determined primarily by energy-dependent diffusion, rather than energetic losses, we would not expect the proton spectrum to change significantly in the `R2` environment compared to the `R8` model.

In addition to the steeper spectrum, we also see a change in the proton to electron ratio in this model compared to the solar neighborhood environment. The CR proton spectra are similar in the `R2` and `R8` models, as in both cases energetic losses are negligible. The CREs, however, have much higher energetic losses in the `R2` environment, resulting in a much greater change in magnitude between the input and midplane-region spectra. Direct observations in the solar neighborhood find the CR proton to electron ratio to be roughly 100 between 1-10 GeV (e.g. Zweibel, 2013). In our `R8` simulations, the ratio of j_p/j_e across

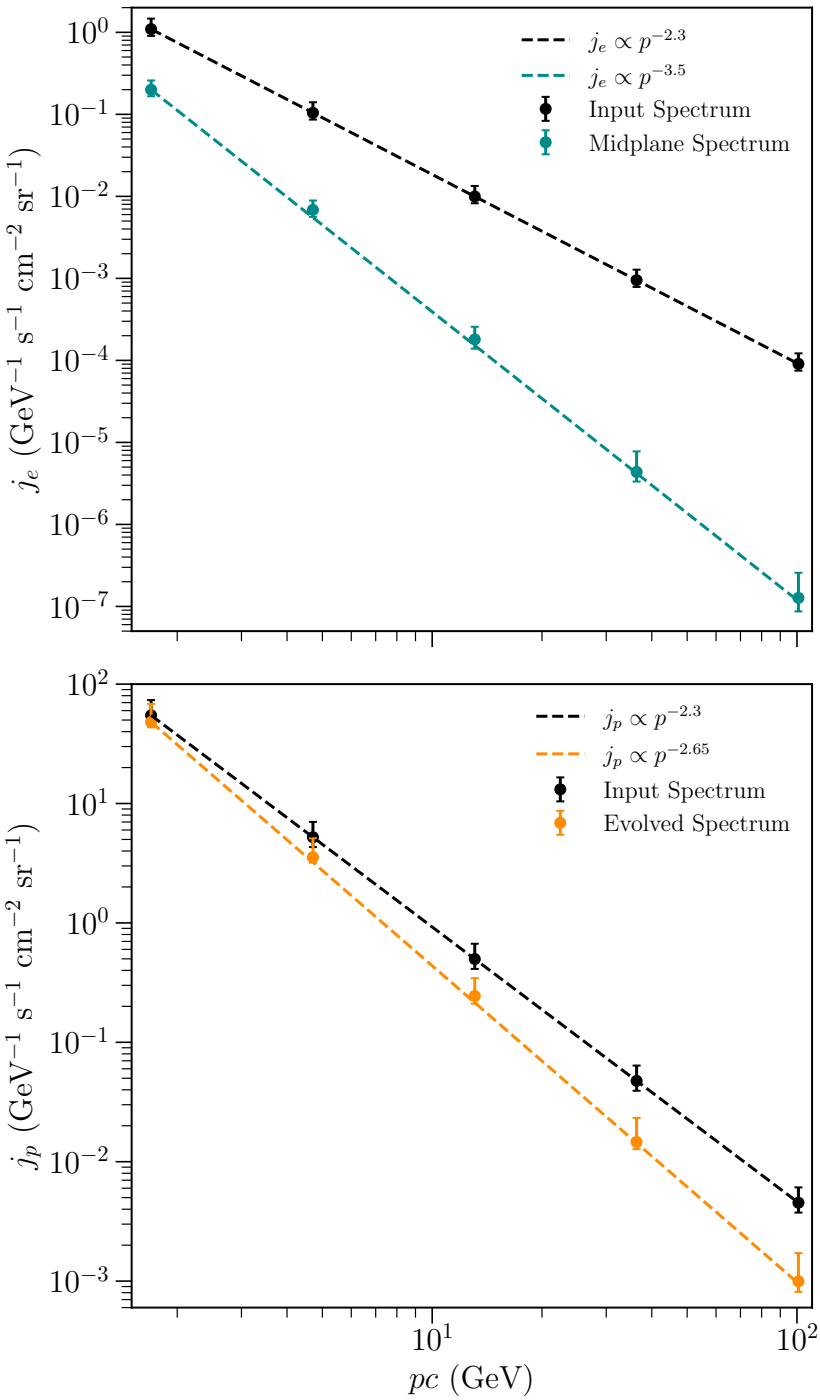

Figure 4.6: Spatially and temporally averaged CR spectra in the midplane warm gas ($T < 3 \times 10^4$ K, $|z| < 150$ pc). The upper and lower panels show the electron and proton spectra respectively. The points represent the median value across space and time, while the error bars show the 16th-84th percentiles. The black points represent the input spectrum with a fixed power-law slope of $s = -2.3$. The blue and orange points represent the measured CRE and CR proton midplane-region spectra. The colored dashed lines show the best fit power laws to the median measured spectra with $j_e \propto p^{-3.5}$ and $j_p \propto p^{-2.65}$.

the five momentum bins varies from $\sim 60 - 400$ (Figure 2.7 and Figure 2.13). In Figure 4.6, this ratio varies from ~ 240 in the lowest momentum bin to ~ 7800 in the highest.

We show the power-law slopes between consecutive momentum bins (Equation 2.39) of the CR proton and electron spectra in Figure 4.7 as a function of CR momentum. As a comparison, in the upper CRE panel we also include the models based on direct solar neighborhood observations from Orlando (2018) and Padovani et al. (2018). The CRE slope in the `R2` model is much steeper than the local observations, and is approximately constant with energy, consistent with CR evolution dominated by IC losses. The lowest energy CRE bin has a slightly shallower slope, where the energetic loss timescale is longer than the transport time (Figure 4.5). The CR proton slope is roughly constant and is very similar to the `R8` value (Figure 2.14).

4.3.4 Synchrotron Emission and Equipartition Estimate

We produce synthetic maps of synchrotron emission following the method described in Section 3.2.2, now using the `R2` snapshots. While before we could produce radio emission across a wide range of observed frequency bands, from 1.5-45 GHz, with these models we are limited to only the higher frequencies. The energy of CREs responsible for synchrotron emission at a given frequency is proportional to $B^{-0.5}$ (Equation 3.21). Because the magnetic field strength in the `R2` models is significantly larger than in `R8`, simulating synchrotron emission in the same frequency bands would require modeling the CRE spectrum below 1 GeV. This is not feasible in our current CR transport scheme. The diffusion rate of the CREs is dependent on the scattering rate determined primarily by the CR protons. However, the approximations we have made of non-interacting, relativistic CR fluids do not hold below ~ 1 GeV for CR protons.

Rather than modeling lower energy CREs, we instead simulate higher frequency emission at 33 and 45 GHz. We found that our analysis in Chapter 3 was insensitive qualitatively to the choice of frequency, so we do not expect this limitation to affect our results. Realistically,

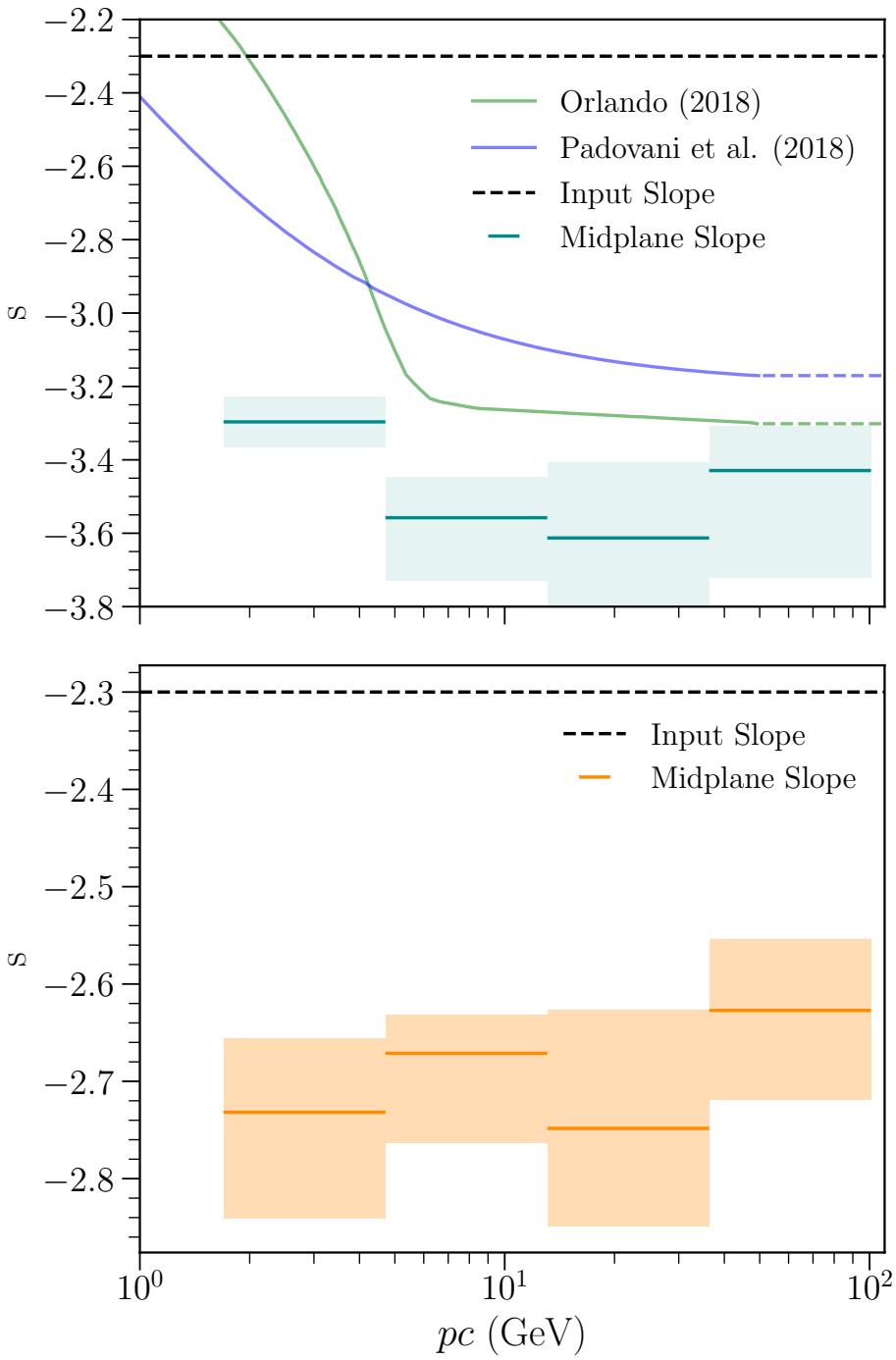

Figure 4.7: Power-law slope of the CR spectra (Figure 4.6) as a function of CR momentum. The upper and lower panels represent the electrons and protons respectively. The slope is calculated across neighboring bins as in Equation 2.39. The solid horizontal lines represent the median value of the slope across all cells with $|z| < 150$ pc and $T < 3 \times 10^4$ from all snapshots. The shaded region shows the 16th-84th percentiles. The green and purple lines are reproduced from Padovani et al. (2021) as in Figure 2.8. The black dashed line represents the input slope.

higher frequency observations would have greater contamination by free-free emission making it more difficult to extract the underlying CRE spectrum and estimate the magnetic field strength, but we do not consider the thermal emission here.

We present mock synchrotron emission at 33 GHz for one R2 snapshot at $t = 30$ Myr in Figure 4.8. Along with this synchrotron emission, we include the vertically mass-averaged values of the total CR energy density and the magnetic field strength determined as in Chapter 3. Finally, we also include the equipartition magnetic field strength as calculated using the traditional equipartition estimate.

To determine the equipartition magnetic field strength, we first use Equation 3.19 as described in Beck & Krause (2005) and summarized in Chapter 3. For the R8 model in Chapter 3, we set the length scale of synchrotron emission $\ell_z = 1$ kpc. For the R2 model, however, the scale height of synchrotron emission is smaller, and we estimate $\ell_z = 300$ pc.

The value of K_0 should also differ in Equation 3.19 for the R2 model compared to R8. In Figure 4.6, we find the proton to electron ratio to be much larger than the assumed $K_0 = 100$ when considering the simulated R2 spectra. Beck & Krause (2005) point out that this ratio would be expected to vary in the case of strong synchrotron and IC losses, and suggest that Equation 3.19 should only be used for CR energies, and radio frequencies, where these losses are not dominant. In the R2 model, we are clearly in the regime with significant IC losses, so the model assumptions fail and Beck & Krause (2005) predict that Equation 3.19 will underestimate the true magnetic field. Even if the model assumptions fail, however, it is still useful to test the traditional equipartition estimate using the generally accepted value of $K_0 = 100$ because it is commonly applied to synchrotron observations in all environments.

In Figure 4.8, we see that the CR energy density is far smoother than the magnetic field, although there is more variation in $e_{\mathrm{c,avg}}$ in the R2 model compared to the R8 model. The CR energy density varies by about a factor of 10 across the simulation box compared to only a factor of 1.5 in the R8 model. Much of the area, however, has near constant $e_{\mathrm{c,avg}}$ with

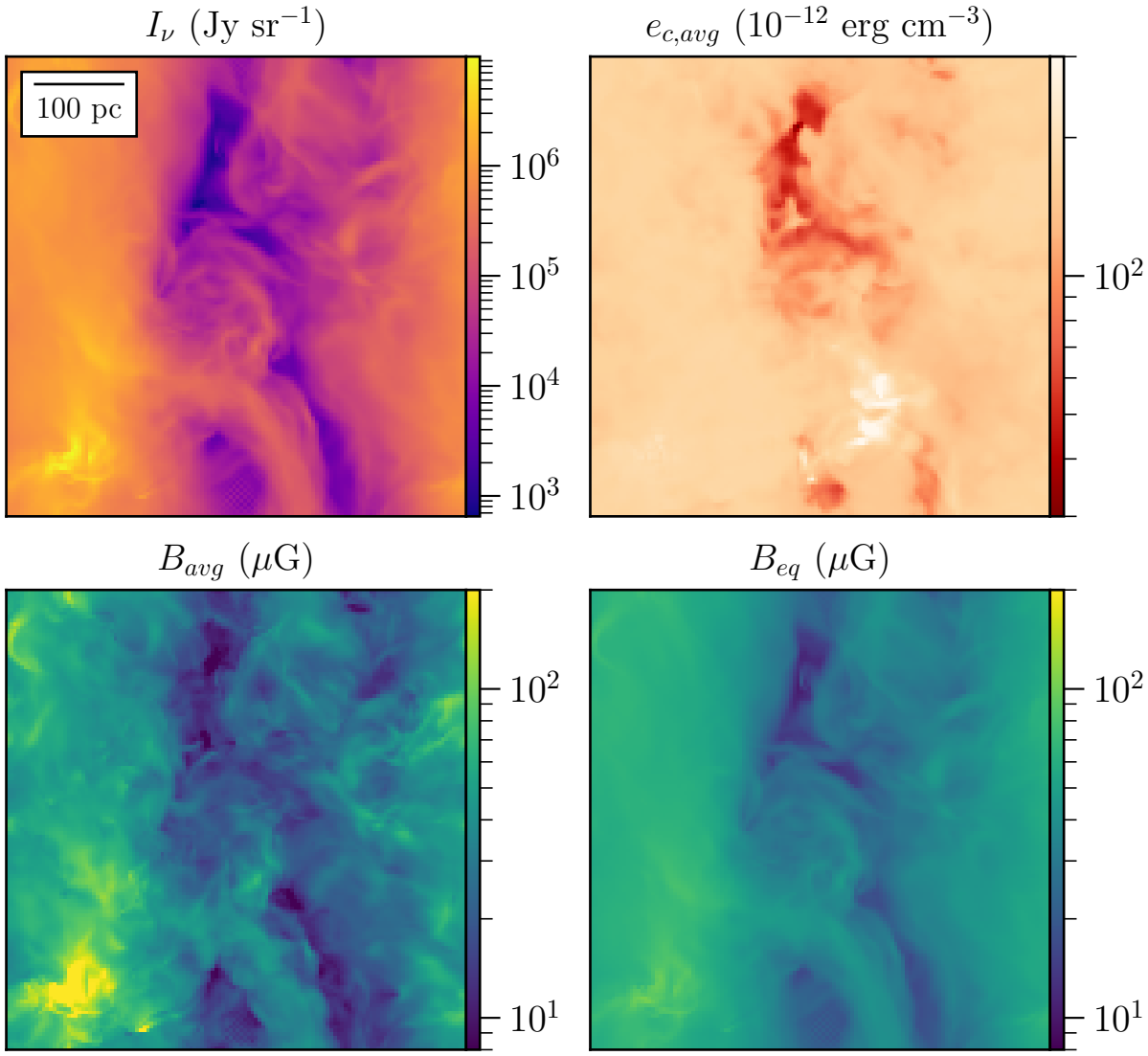

Figure 4.8: Vertically integrated and mass-averaged quantities from the $t = 30$ Myr snapshot of the `R2` model. From left to right, the four panels show synchrotron intensity (I_ν) at 33 GHz (Equation 3.8), the total mass-weighted average CR electron energy density ($e_{c,\mathrm{avg}}$), the mass-weighted average magnetic field strength (B_{avg}), and the equipartition estimate of the magnetic field strength (B_{eq}) as determined by Equation 3.19.

only the central region having lower values. This difference could be due to the lack of the MHD relaxation step.

The mass-averaged magnetic field strength varies by around a factor of 20 across the simulation region while the estimated equipartition magnetic field has much less variation. We compare these two values pixel by pixel across all snapshots in Figure 4.9 in a two-dimensional histogram. The best-fit power law to this distribution is given in a purple line, and we find that $B_{\rm eq} \propto B_{\rm avg}^{0.43}$. If the two values were in perfect agreement, they would follow the one-to-one relationship shown in the black dashed line. In Figure 4.6, we found that the CRE spectral index is approximately -3.5. Therefore, we would expect $B_{\rm eq} \propto B^{(\alpha+1)/(\alpha+3)} \propto B^{0.5}$ following the same reasoning as in Chapter 3. Despite this scaling between $B_{\rm eq}$ and $B_{\rm avg}$, the overall magnitudes of the two values are remarkably similar. $B_{\rm eq}$ is within a factor of two of $B_{\rm avg}$ for 92% of the pixels.

Along with the pixel-by-pixel distribution, we also include the simulation box-averaged values of $B_{\rm eq}$ compared to $B_{\rm avg}$ for each snapshot as red points. Although the magnitudes of $B_{\rm eq}$ and $B_{\rm avg}$ are still very similar, there is a clear scaling between the two values with approximately the same relationship as the pixel-by-pixel distribution. This was not true for the `R8` or `R8 Arm` models presented in Chapter 3.

We additionally test the three alternative equipartition estimates which approximate e_c as a constant value determined by the average equipartition magnetic energy density, a value proportional to $\Sigma_{\rm SFR}$, or as a fraction of the ISM weight. These are defined in Equation 3.29, Equation 3.34, and Equation 3.39 respectively. For these estimations, we use the same fits for $\Upsilon_{\rm c}$ and $\Upsilon_{\rm tot}$ as given in Chapter 3. We present the predicted magnetic field compared to the true value in each of these cases in Figure 4.10.

As with the `R8` models, estimating e_c using a constant value improves the scaling of the predicted magnetic field compared to the true value over the traditional equipartition estimate. This scaling is similar in all of the alternative estimates with $B_{\rm pred} \propto B_{\rm avg}^{0.65-0.71}$. The relative magnitudes of the three estimates vary, however. The average estimate using

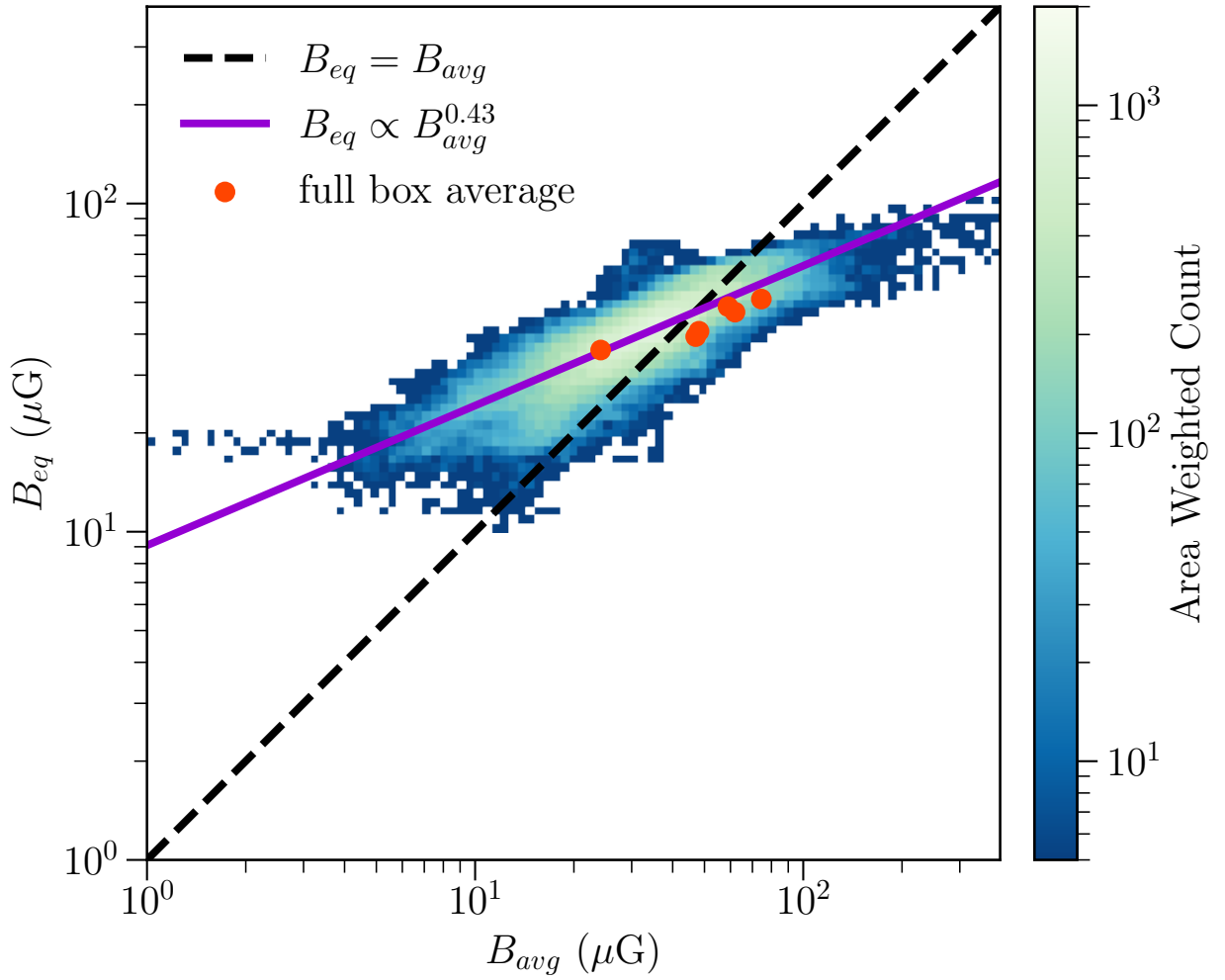

Figure 4.9: Th distribution shown in the blue color scale represents a two-dimensional histogram of the equipartition magnetic field strength, $B_{\rm eq}$, compared to the simulated, mass-averaged magnetic field strength, $B_{\rm avg}$. This distribution includes each pixel across six `R2` model snapshots. The best fit power law to this distribution is included as a purple line with $B_{\rm eq} \propto B_{\rm avg}^{0.43}$. The black, dashed line represents $B_{\rm eq} = B_{\rm avg}$. The red points represent the values of $B_{\rm eq}$ and $B_{\rm avg}$ averaged over each simulation snapshot individually representing a scale of about 0.5 kpc.

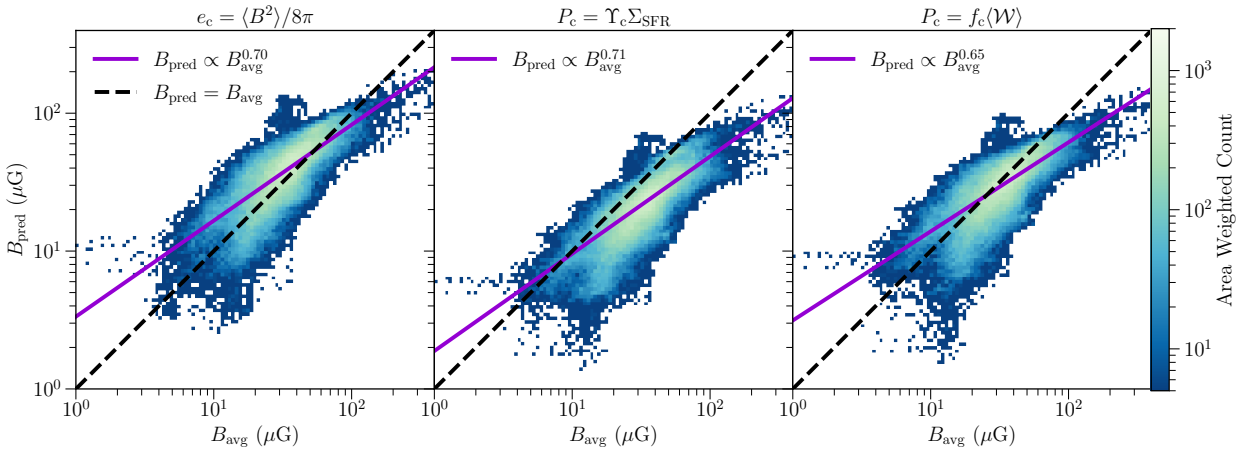

Figure 4.10: Each panel shows a two-dimensional histogram comparing one prediction of the magnetic field strength to the simulated, mass-averaged value. These distributions include all pixels across six `R2` snapshots. The left panel estimates the magnetic field using Equation 3.29 where the total CR energy density is assumed to be a constant value determined by the average value of the equipartition field (Equation 3.19). The middle panel estimates the CR pressure as a fraction of the total ISM pressure as a function of Σ_{SFR}. The right panel estimates the CR energy density as a fraction of the total ISM weight (Equation 3.39). In all three panels, the black, dashed line shows $B_{pred} = B_{avg}$ and the purple line shows the best-fit power law to the distribution.

Equation 3.29 is nearly identical to the true value, whereas Equation 3.34 and Equation 3.39 underestimate the true magnetic field strength by a factor of $\sim$1.7 and $\sim$1.3 respectively. If we had used the typical length scale of synchrotron emission, $\ell_z = 1$ kpc, instead of $\ell_z = 300$ pc, the estimates would be reduced by a factor of 1.4 for Equation 3.29 or 1.8 for Equation 3.34 and Equation 3.39, representing a more significant underestimation of the true magnetic field strength. As with the `R8` model, it would be useful to calibrate these alternative estimates with a global model while also considering the possible variations in both ℓ_z and K_0.

4.4 Discussion

4.4.1 Comparison to Observations

The measured CRE spectrum in the midplane regions of the simulation is significantly different in the `R2` model compared to the `R8` model. Rather than having a spectral slope which steepens as a function of energy, the CRE spectrum in the `R2` model has an approximately constant power-law slope with $s \approx -3.5$ due to the dominant IC losses. This result does not appear to be consistent with direct observations, however. In studies of both edge-on and face-on galaxies, the synchrotron spectral index, which is interpreted as the CR spectral slope, is found to be shallower at smaller galactic radii (e.g. Fletcher et al., 2011; Mulcahy et al., 2014; Stein et al., 2023).

One possible explanation for this discrepancy is that the measurements of the synchrotron spectrum are done using two fixed frequency bands. At fixed frequency, the CRs primarily responsible for the synchrotron emission have energy $E \propto B^{-0.5}$ (Beck & Krause, 2005). Therefore, if magnetic field were to increase, as we would expect moving towards the galactic center, then observations at a given frequency would probe lower energy CREs. The `R2` model has magnetic fields as strong as 100 μG. For synchrotron observations at 144 MHz and 1.5 GHz (common frequency bands for observations of this type), this would correspond to CRE energies of 0.3-1 GeV. Our simulated CREs do not extend to these energies, but direct observations show that the CRE spectrum can be significantly shallower at lower energies (e.g. Padovani et al., 2021). At lower energies (< 1 GeV), CRs have a larger scattering rate and diffusion is expected to be low. In this case, there would not be spectral steepening from differential diffusivity, and the only steepening would be due to energetic losses.

The proton spectrum in Figure 4.6 is well modeled by a single power-law with $s \approx -2.65$ (Figure 4.6). This is slightly steeper compared to the proton spectrum in the `R8` model, with $\Delta s \sim 0.08$ when comparing the best-fit power-law slope. However, the variation in the slopes calculated between consecutive energy bins is large (see Figure 2.14 and Figure 4.7).

The simulated CR proton spectrum is consistent with the spectrum derived from gamma-ray observations of the Milky Way, which find a spectral index of $\sim -2.6 \pm 0.05$ at a radius of 2 kpc (see Figure 8 in Acero et al., 2016).

4.4.2 Comparison to Other Models

Both Hopkins et al. (2022a) and Werhahn et al. (2021b) also consider the CR spectral slope as a function of radius. As these works use global models of CR transport in full galaxy simulations, they find the radial dependence of the spectral index by averaging over rings of fixed radius. We discussed the details of CR transport in these models in Section 2.4.

Hopkins et al. (2022a) find both the CR proton and electron spectra as a function of radius considering particles with energy between $\sim 0.01-10$ GeV, and note that the CRE spectrum steepens moving to smaller galactic radii. As in our results, they find that the increasing energetic losses closer to the galactic center steepen the CRE spectrum. Although the proton spectrum in our model is slightly steeper in the `R2` model compared to the `R8` model, Hopkins et al. (2022a) find that the proton spectrum is shallower at smaller galactic radii. They point out that CR protons, unlike electrons, have the lowest energetic loss rate at ~ 1 GeV, and the energetic losses increase towards both higher and lower CR energy. The exact energy at which the losses are minimized depends on local gas conditions (e.g. Padovani et al., 2020). Hopkins et al. (2022a) find that the increasing energetic losses towards lower energy results in a shallower CR proton spectral slope. The change in the slope between the galactic radii of 2 and 8 kpc is small, however, and the uncertainties are large both in the simulations and observations. Therefore, it is difficult to draw significant conclusions about the radial dependence of the proton spectrum.

Werhahn et al. (2021b) also see very little difference in the CR proton spectral slope considering the two radii we model. Additionally, they note that in the inner galaxy, the CRE spectral evolution is dominated by radiative losses, while on the outskirts diffusion is dominant. Therefore, they similarly find the CRE spectrum to steepen at smaller galactic

radii. Unlike our results, however, Werhahn et al. (2021b) do not find a significant difference in the spectral index between galactic radii of 2 and 8 kpc. Instead they find the CRE spectrum to be dominated by radiative losses below $\sim$ 15 kpc. There are many possible explanations for this discrepancy. First, our simulation and CR transport method differs from that in Werhahn et al. (2021b), as discussed in Section 2.4. Additionally, they find the spectral index by averaging over a larger altitude, extending to $z \sim 0.7$ kpc.

Another explanation may be the way the radiation field is determined. Werhahn et al. (2021b) include both CMB and IR radiation where the IR energy density in each cell is the sum of the flux arriving from every other cell, and the IR luminosity in each cell is proportional to the local SFR. This is different from our method, where we estimate a single radiation profile for each environment. As the IC losses are the primary cause of spectral steepening in our `R2` model, we would expect a change in the radiation field to result in a different final spectrum. In Section 4.B we consider the `R2` snapshots with lower $\Sigma_{\rm SFR}$ and find an evolved spectral slope that is more consistent with the `R8` model. Without knowing precisely what radiation field Werhahn et al. (2021b) use, however, we cannot say if this is a feasible explanation of the difference in the CRE spectral slope.

4.5 Summary

We use the CR transport scheme presented in Chapter 2 to post-process the `R2` TIGRESS simulation. This environment has more extreme conditions with greater density, gas velocity, and magnetic field leading to greater energetic losses for the CREs. The evolved CRE spectrum is much steeper than in the `R8` model due to the faster energetic loss rates, with an approximately constant power-law slope. The proton spectrum, which steepens due to energy-dependent transport, does not change significantly from the `R8` model.

Although the equipartition estimate of magnetic field strength presented in Beck & Krause (2005) is not designed to extend to environments with such strong magnetic fields

considering the CRE energies and synchrotron frequencies we model, it still gives a good estimate of the magnetic field strength in the `R2` simulations. We are limited, however, by the smaller `R2` box size.

4.A Inner Galaxy Radiation Field

As in Section 2.C, we must approximate the total radiation energy density, w, as it is not determined self-consistently in the code. Again, this is a combination of UV and optical starlight, IR radiation from dust absorption and reemission, and background CMB. The CMB has a constant $w_{CMB} \approx 4.2 \times 10^{-13}$ erg/cm^3 (Draine, 2011).

For the `R8` model, we used TIGRESS-NCR simulations (Kim et al., 2023a) with adaptive ray tracing to estimate the UV emission. Although there are no NCR models which correspond to exactly the same conditions as the `R2` simulations we post-process in this chapter, there are similar models. We use the TIGRESS-NCR model most like the `R2` model (`S150-Om100q0-Z1.0`, Kim et al. (2024)), and take the horizontally and time-averaged, vertical profile of w_{UV}.

As in the previous model, we estimate the midplane optical emission by using the ISRF described in Kim et al. (2023b) to determine the ratio between UV and optical radiation. Unlike in the solar neighborhood model, we account for the fact that the optical radiation should have a larger scale height compared to the UV radiation as it has a lower dust absorption cross section. To do so, we first fit the UV radiation profile within 500 pc of the midplane with an exponential function

$$w_{UV}(z) = w_{UV,0} e^{-|z|/H_{UV}} \tag{4.1}$$

where $H_{UV} \approx 125$ pc is the scale height of the UV radiation energy density and $w_{UV,0}$ is the midplane UV radiation energy density. We then approximate the optical radiation scale

height as

$$H_{opt} \approx H_{UV} \frac{\sigma_{dust,UV}}{\sigma_{dust,opt}} \approx 3H_{UV} \tag{4.2}$$

where $\sigma_{dust,UV}$ and $\sigma_{dust,opt}$ are the dust absorption cross sections of UV and optical radiation (Kim et al., 2023b). The optical radiation then takes the same form as Equation 4.1 substituting for the scale height and the normalization.

In Section 2.C, we had the benefit of local observations of the IR energy density to normalize our estimate of the radiation energy density relative to the optical and UV emission. For our inner galaxy model, we must make a rough approximation of the IR field. As before, we approximate

$$w_{\rm IR}(z) = \frac{1}{4\pi c} \iiint \frac{L_{IR}(x,y,z')dxdydz'}{x^2+y^2+(z-z')^2} \tag{4.3}$$

where now we integrate over a 1 kpc patch in the x-y plane. L is the IR luminosity density at any point given by

$$L(x,y,z) = Ae^{-|z|/H_{IR}} \tag{4.4}$$

We approximate $H_{IR} = H_{opt}$ assuming that the absorption of optical radiation produces the majority of the IR emission, and that any absorbed radiation is immediately reemitted. The normalization factor, A, is fixed such that

$$\int L_{IR}(x,y,z)dz = \Sigma_{IR} = (1-e^{-\tau_{opt}})\Sigma_{opt} + (1-e^{-\tau_{UV}})\Sigma_{UV} \approx 2.3\Sigma_{UV} \tag{4.5}$$

where Σ_X represents the radiation surface density of wavelength range X, and τ is the optical depth of the radiation to dust absorption. These values can be estimated directly from the NCR models. Once we have the final approximation of the radiation field, we rescale w to the SFR of each post-processed TIGRESS snapshot relative to the average SFR of the NCR model.

4.B Low $\Sigma_{\rm SFR}$ Snapshots

4.B.1 Energetic Losses

In Figure 4.11 and Figure 4.12 we present the energetic loss rates and the CR timescales respectively for the three low-$\Sigma_{\rm SFR}$ snapshots of the `R2` model discussed in Section 4.2. From Figure 4.11 we can see that the IC losses are smaller in magnitude compared to the profiles in Figure 4.4, and in the lowest energy bin, the IC losses are comparable to the other loss mechanisms in the midplane. This is similar to the result for the `R8` model shown in Figure 2.5. As with all of the previous results, however, the IC losses are larger at all energies in the extraplanar region due to the larger scale height of the radiation energy density compared to the magnetic field or gas density.

The smaller IC losses correspond to longer loss timescales, as we can see in Figure 4.12 where we compare the loss, transport, and diffusion timescales for the low-$\Sigma_{\rm SFR}$ models. The loss timescale is longer than the transport time at all z in the lowest energy CRE bin. As CRE energy increases, the losses become more significant, but the loss timescale is only shorter than the transport time in the two highest energy bins. Therefore, we would predict the CRE spectral evolution to be more similar to the `R8` model in these snapshots, where both energetic losses and energy-dependent transport are important.

4.B.2 Spectrum

In Figure 4.13, we show the injected and measured midplane CRE spectra for the low-$\Sigma_{\rm SFR}$ `R2` snapshots. By fitting the evolved spectrum with a single power-law, we find that the spectral index steepens from the injected value of $s = -2.3$ to $s \approx -3.2$. The measured slope is shallower than the high-$\Sigma_{\rm SFR}$ models, which have a best-fit final slope of $s \approx -3.5$ (Figure 4.6). Although we do not include the CR proton spectrum here, we find that the spectral index does not change significantly from the value in the high-$\Sigma_{\rm SFR}$ models. This

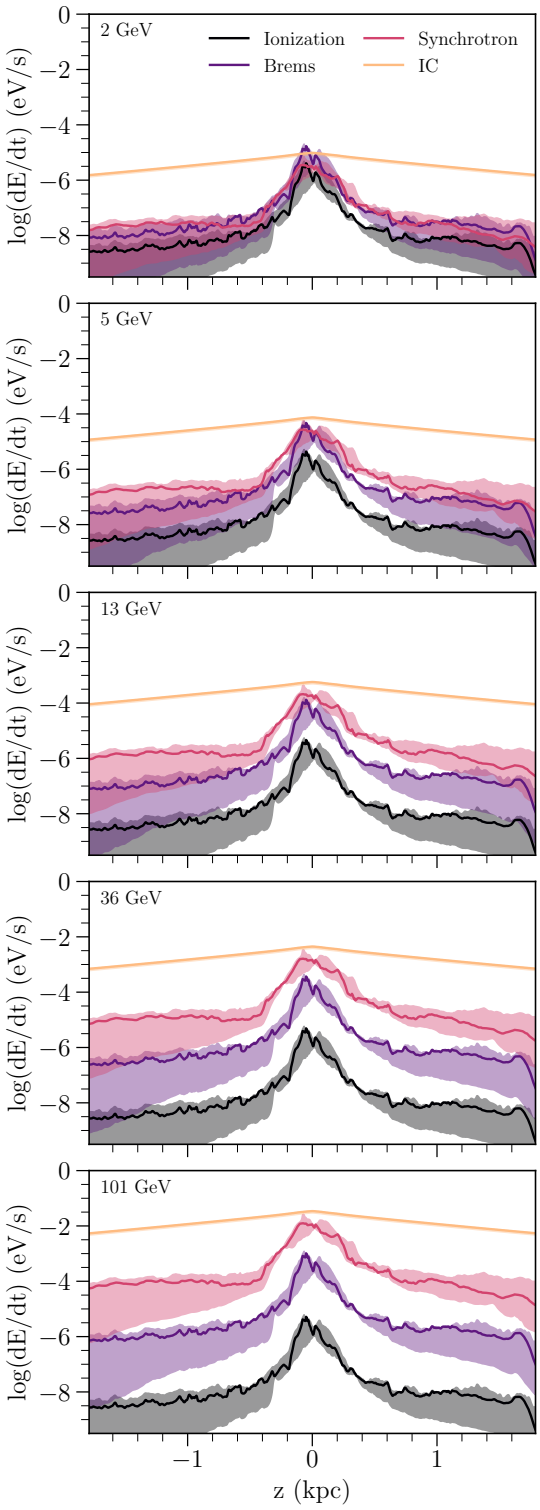

Figure 4.11: Same as Figure 4.4 but for the low-$\Sigma_{\rm SFR}$ R2 snapshots.

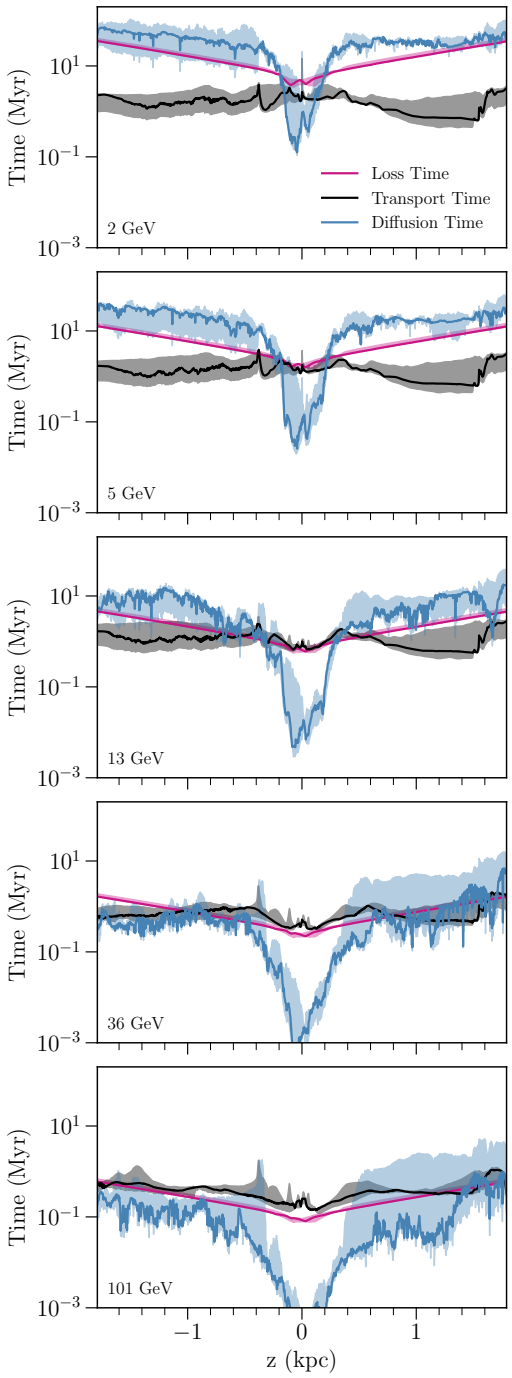

Figure 4.12: Same as Figure 4.5 but for the low-$\Sigma_{\rm SFR}$ R2 snapshots.

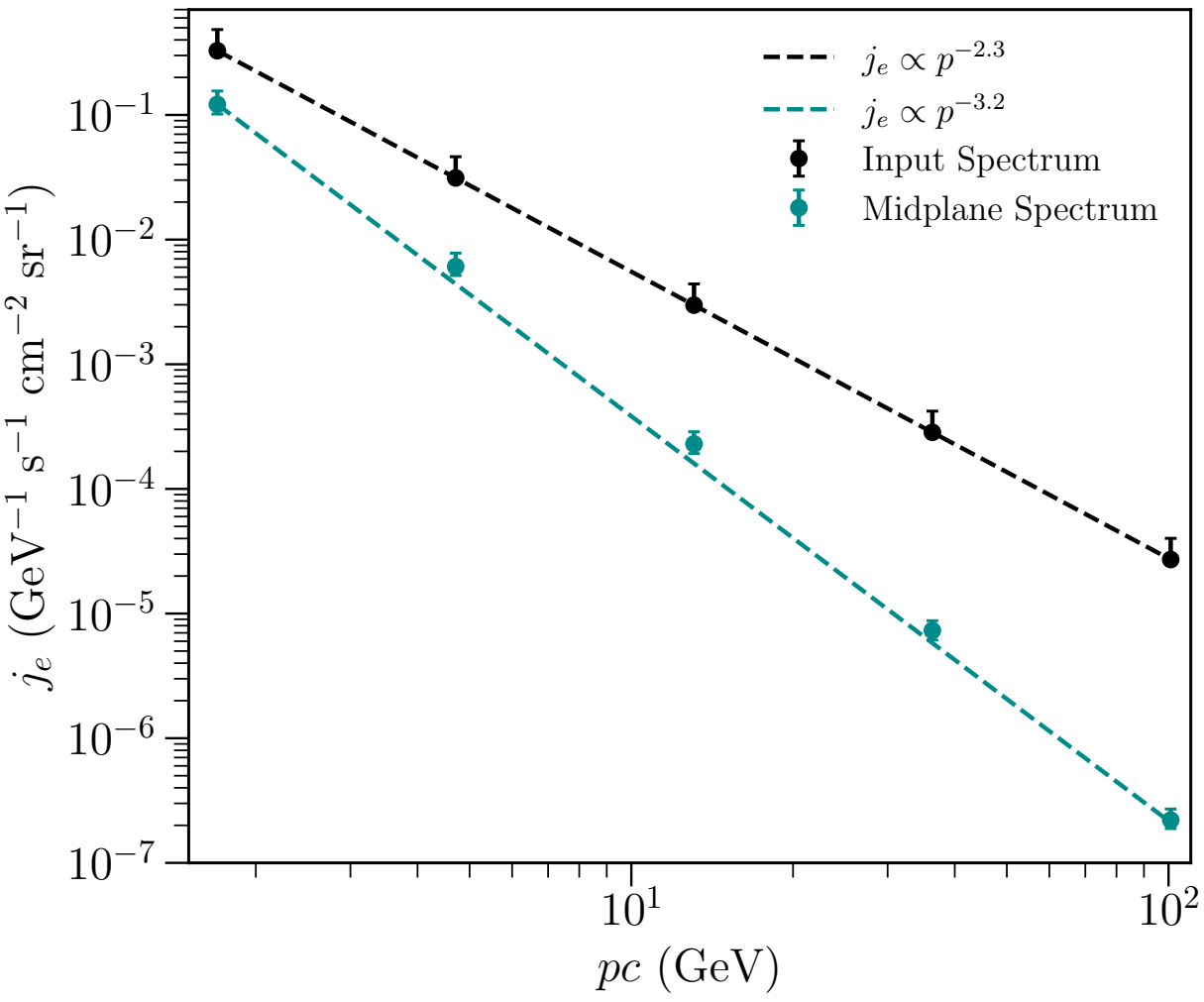

Figure 4.13: Same as the upper panel of Figure 4.6 but for the low-$\Sigma_{\rm SFR}$ `R2` snapshots. The best fit power law to to the median measured CRE spectrum has $j_e \propto p^{-3.2}$.

is to be expected as the energetic losses are not important for the CR proton spectral steepening.

In Figure 4.14, we show the CR spectral slope as a function of energy. Unlike in Figure 4.7, where the slope is relatively constant due to the dominant IC losses, here we see energy-dependent spectral steepening. The behavior of the CRE spectral slope is similar to the result based on modeling of direct observations in the solar neighborhood presented in Orlando (2018). Although the slope is steeper overall compared to the values shown in Figure 2.8 for the `R8` model, we can still see a clear cooling break.

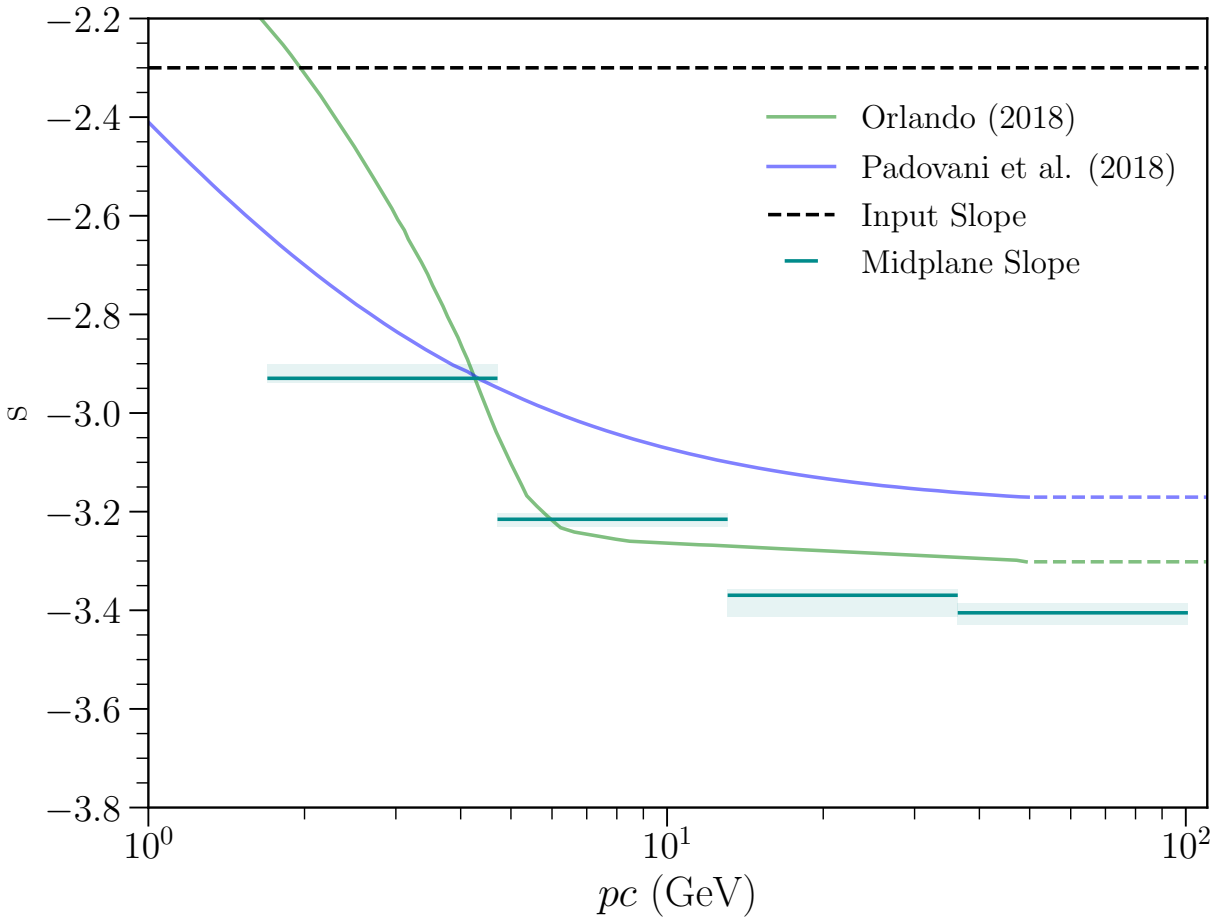

Figure 4.14: Same as the upper panel of Figure 4.7 but for the low-$\Sigma_{\rm SFR}$ `R2` snapshots.

From these results, we can see that the magnitude of IC losses, and therefore the radiation energy density, is extremely important in determining the final CRE spectrum. If the radiation field is large enough to produce dominant IC losses, and the loss timescale is shorter than the CR transport time, the CRE spectral slope has constant steepening as a function of energy. This is the case in the majority of our `R2` snapshots. On the other hand, if the IC losses are not dominant, as in the low $\Sigma_{\rm SFR}$ snapshots, the evolved spectrum is more similar to the locally observed values. Therefore, it is of great interest to self-consistently model the local radiation field to accurately model the evolution of the CRE spectrum.

Chapter 5

Conclusions and Future Work

In this thesis, we have presented a scheme to model the transport and spectral evolution of CREs, and have applied this method by post-processing simulations of the multiphase ISM. We make use of the highly accurate TIGRESS simulations to model realistic spatial transport of CRs based on local gas and CR properties. Although we must simplify the spectral evolution by dividing the CRs into independent energy bins, and are limited to post-processing simulations without including the CR back-reaction on the gas, we still produce CR spectra that are consistent with direct observations in the solar neighborhood. The limitations in our model, however, provide many opportunities for future improvements to the method and further analysis.

To evolve the CR spectra more accurately, it will be necessary to model the interaction between our simulated CR fluids, allowing for the transfer of energy due to adiabatic and collisional losses. While in this analysis we were limited to the midplane where adiabatic losses were small, adding self-consistent energy transfer between the CR fluids will enable the study of the CR spectrum in the extraplanar region where adiabatic losses are much more significant. Additionally, when modeling CRs above 1 GeV we were able to ignore the transfer of CRs from higher to lower energy bins due to collisional and radiative losses because the spectrum was steep enough that this effect was negligible. To model lower energy

CRs, it will be necessary to include the effect of collisional losses self-consistently. A scheme for modeling interacting CR fluids will be presented in Armillotta and Ostriker (in prep.).

Another significant improvement to the CR modeling will be to include CR transport in simulations with live MHD, thereby allowing the CRs to directly affect the gas. In the next-generation TIGRESS models, a single CR fluid representing 1 GeV CR protons will be evolved along with the MHD variables. This will not only allow us to better understand how CRs affect the multiphase ISM, but also improve our understanding of the CR spatial distribution. Due to the large computational expense of modeling multiple CR fluids, simulating the CR spectral evolution will still be limited to post-processing. This analysis, however, will be more accurate when the initial TIGRESS simulations include ISM structure modified by CR feedback. Additionally, if the radiation fields are modeled along with the MHD variables, the IC losses can be determined self-consistently without relying on a fixed model. This will also result in a more accurate determination of the ionization state of the gas, improving the calculation of the scattering coefficient and collisional losses.

In the current model, we assume that NLL is always the dominant source of damping in the hot ISM. This is not necessarily true, as both turbulent (e.g. Farmer & Goldreich, 2004) and linear Landau (e.g. Wiener et al., 2018) damping may also be important. Adding additional damping processes would modify the scattering coefficients and therefore change the transport in the hot gas. In the future, it will be useful to consider these additional damping mechanisms.

Even with our current, simplified model of CR transport, we still produced useful comparisons to observations. First, we found that the CRE spectrum can be recovered accurately from synchrotron observations. Additionally, if the radio observations cover a wide enough range of frequencies, we can also recover the CRE spectral steepening. The magnetic field direction can be determined well by polarized radio emission. Furthermore, we found that the traditional equipartition formulation of magnetic fields gives a good estimate of the true magnetic field strength on the scale of the simulation box in multiple galactic environments.

This method can also be improved on small scales by bringing in additional observations under the assumption of a smooth CR distribution.

Using only the current model, we can produce additional observables, such as synthetic gamma-ray emission, by considering the CR proton spectrum. Further comparisons to observations will be possible after improving the CR transport method. With more realistic modeling including the CR back-reaction on MHD, we can consider the vertical variation in the CR spectrum rather than focusing on the midplane. For example, we can produce mock synchrotron observations to be compared to observations of edge-on galaxies, as opposed to the current work in which we were limited to face-on observations. With a more realistic ISM structure and ionization state, we can produce more accurate radio emission maps including both synchrotron and free-free emission. This will provide a good test of how contamination by thermal emission affects our conclusions about the CRE spectrum and magnetic field. Extending the work to TIGRESS simulations beyond the solar neighborhood and inner galaxy models will allow for a global calibration of the techniques used to estimate the magnetic field strength, and a better understanding of CR transport in all environments.

Bibliography

Acero, F., Ackermann, M., Ajello, M., et al. 2016, Development of the Model of Galactic Interstellar Emission for Standard Point-source Analysis of Fermi Large Area Telescope Data, ApJS, 223, 26, doi: 10.3847/0067-0049/223/2/26

Aguilar, M., Alberti, G., Alpat, B., et al. 2013, First Result from the Alpha Magnetic Spectrometer on the International Space Station: Precision Measurement of the Positron Fraction in Primary Cosmic Rays of 0.5–350 GeV, Phys. Rev. Lett., 110, 141102, doi: 10.1103/PhysRevLett.110.141102

Aguilar, M., Aisa, D., Alvino, A., et al. 2014, Electron and Positron Fluxes in Primary Cosmic Rays Measured with the Alpha Magnetic Spectrometer on the International Space Station, Phys. Rev. Lett., 113, 121102, doi: 10.1103/PhysRevLett.113.121102

Aguilar, M., Aisa, D., Alpat, B., et al. 2015, Precision Measurement of the Proton Flux in Primary Cosmic Rays from Rigidity 1 GV to 1.8 TV with the Alpha Magnetic Spectrometer on the International Space Station, Phys. Rev. Lett., 114, 171103, doi: 10.1103/PhysRevLett.114.171103

Armillotta, L., Ostriker, E. C., & Jiang, Y.-F. 2021, Cosmic-Ray Transport in Simulations of Star-forming Galactic Disks, ApJ, 922, 11, doi: 10.3847/1538-4357/ac1db2

Armillotta, L., Ostriker, E. C., & Jiang, Y.-F. 2022, Cosmic-Ray Transport in Varying Galactic Environments, ApJ, 929, 170, doi: 10.3847/1538-4357/ac5fa9

Armillotta, L., Ostriker, E. C., Kim, C.-G., & Jiang, Y.-F. 2024, Cosmic-Ray Acceleration of Galactic Outflows in Multiphase Gas, ApJ, 964, 99, doi: 10.3847/1538-4357/ad1e5c

Armillotta, L., Ostriker, E. C., & Linzer, N. B. 2025, Energy-Dependent Transport of Cosmic Rays in the Multiphase, Dynamic Interstellar Medium, arXiv e-prints, arXiv:2507.00120, doi: 10.48550/arXiv.2507.00120

Axford, W. I., Leer, E., & Skadron, G. 1977, in International Cosmic Ray Conference, Vol. 11, International Cosmic Ray Conference, 132

Bai, X.-N., Ostriker, E. C., Plotnikov, I., & Stone, J. M. 2019, Magnetohydrodynamic Particle-in-cell Simulations of the Cosmic-Ray Streaming Instability: Linear Growth and Quasi-linear Evolution, ApJ, 876, 60, doi: 10.3847/1538-4357/ab1648

Beck, R. 2016, Magnetic fields in spiral galaxies, A&A Rev., 24, 4, doi: 10.1007/s00159-015-0084-4

Beck, R., & Krause, M. 2005, Revised equipartition and minimum energy formula for magnetic field strength estimates from radio synchrotron observations, Astronomische Nachrichten, 326, 414, doi: 10.1002/asna.200510366

Becquerel, H. 1896, Sur les radiations émises par phosphorescence, Comptes rendus de 1'Academie des Sciences, Paris, 122, 420

Bell, A. R. 1978a, The acceleration of cosmic rays in shock fronts - I., MNRAS, 182, 147, doi: 10.1093/mnras/182.2.147

Bell, A. R. 1978b, The acceleration of cosmic rays in shock fronts - II., MNRAS, 182, 443, doi: 10.1093/mnras/182.3.443

Blandford, R. D., & Ostriker, J. P. 1978, Particle acceleration by astrophysical shocks., ApJ, 221, L29, doi: 10.1086/182658

Blasi, P. 2013, The origin of galactic cosmic rays, A&A Rev., 21, 70, doi: 10.1007/s00159-013-0070-7

Blasi, P., Amato, E., & Serpico, P. D. 2012, Spectral Breaks as a Signature of Cosmic Ray Induced Turbulence in the Galaxy, Phys. Rev. Lett., 109, 061101, doi: 10.1103/PhysRevLett.109.061101

Böss, L. M., Steinwandel, U. P., Dolag, K., & Lesch, H. 2023, CRESCENDO: an on-the-fly Fokker-Planck solver for spectral cosmic rays in cosmological simulations, MNRAS, 519, 548, doi: 10.1093/mnras/stac3584

Bracco, A., Padovani, M., & Galli, D. 2024, A new analytical model of the cosmic-ray energy flux for Galactic diffuse radio emission, A&A, 686, A52, doi: 10.1051/0004-6361/202449625

Braun, R., Bourke, T., Green, J. A., Keane, E., & Wagg, J. 2015, in Advancing Astrophysics with the Square Kilometre Array (AASKA14), 174, doi: 10.22323/1.215.0174

Bustard, C., & Zweibel, E. G. 2021, Cosmic-Ray Transport, Energy Loss, and Influence in the Multiphase Interstellar Medium, ApJ, 913, 106, doi: 10.3847/1538-4357/abf64c

Butsky, I. S., Fielding, D. B., Hayward, C. C., et al. 2020, The Impact of Cosmic Rays on Thermal Instability in the Circumgalactic Medium, ApJ, 903, 77, doi: 10.3847/1538-4357/abbad2

Caprioli, D. 2023, Particle Acceleration at Shocks: An Introduction, arXiv. http://arxiv.org/abs/2307.00284

Chan, T. K., Kereš, D., Hopkins, P. F., et al. 2019, Cosmic ray feedback in the FIRE simulations: constraining cosmic ray propagation with GeV γ-ray emission, MNRAS, 488, 3716, doi: 10.1093/mnras/stz1895

Chandran, B. D. G. 2000, Confinement and Isotropization of Galactic Cosmic Rays by Molecular-Cloud Magnetic Mirrors When Turbulent Scattering Is Weak, ApJ, 529, 513, doi: 10.1086/308232

Chiu, H. H. S., Ruszkowski, M., Thomas, T., Werhahn, M., & Pfrommer, C. 2024, Simulating Radio Synchrotron Morphology, Spectra, and Polarization of Cosmic Ray Driven Galactic Winds, ApJ, 976, 136, doi: 10.3847/1538-4357/ad84e9

Clay, J. 1927, Proc. Roy. Acad, Amsterdam, 30, 1115

Compton, A. H. 1936, Recent Developments in Cosmic Rays, Review of Scientific Instruments, 7, 71, doi: 10.1063/1.1752085

Cox, D. P. 2005, The Three-Phase Interstellar Medium Revisited, ARA&A, 43, 337, doi: 10.1146/annurev.astro.43.072103.150615

Crocker, R. M., Krumholz, M. R., & Thompson, T. A. 2021, Cosmic rays across the star-forming galaxy sequence - I. Cosmic ray pressures and calorimetry, MNRAS, 502, 1312, doi: 10.1093/mnras/stab148

Curie, P., Curie, M., & Bémont, G. 1898, Sur une nouvelle substance fortement radioactive, contenue dans la pechblende, Comptes rendus de 1'Academie des Sciences, Paris, 127, 1215

Dacunha, T., Martin-Alvarez, S., Clark, S. E., & Lopez-Rodriguez, E. 2025, The Fallibility of Equipartition Magnetic Field Strengths from Synchrotron Emission Using Synthetically Observed Galaxies, ApJ, 980, 197, doi: 10.3847/1538-4357/adab72

De Angelis, A. 2010, Domenico Pacini, uncredited pioneer of the discovery of cosmic rays, La Rivista del Nuovo Cimento, 33, 713

Draine, B. T. 2011, Physics of the Interstellar and Intergalactic Medium, Princeton Series in Astrophysics (Princeton N.J.: Princeton University Press)

Elmegreen, B. G., & Scalo, J. 2004, Interstellar Turbulence I: Observations and Processes, ARA&A, 42, 211, doi: 10.1146/annurev.astro.41.011802.094859

Evoli, C., Blasi, P., Amato, E., & Aloisio, R. 2020a, Signature of Energy Losses on the Cosmic Ray Electron Spectrum, Phys. Rev. Lett., 125, 051101, doi: 10.1103/PhysRevLett.125.051101

Evoli, C., Blasi, P., Morlino, G., & Aloisio, R. 2018, Origin of the Cosmic Ray Galactic Halo Driven by Advected Turbulence and Self-Generated Waves, Phys. Rev. Lett., 121, 021102, doi: 10.1103/PhysRevLett.121.021102

Evoli, C., Gaggero, D., Grasso, D., & Maccione, L. 2008, Cosmic ray nuclei, antiprotons and gamma rays in the galaxy: a new diffusionmodel, J. Cosmology Astropart. Phys., 2008, 018, doi: 10.1088/1475-7516/2008/10/018

Evoli, C., Gaggero, D., Vittino, A., et al. 2017, Cosmic-ray propagation with DRAGON2: I. numerical solver and astrophysical ingredients, J. Cosmology Astropart. Phys., 2017, 015, doi: 10.1088/1475-7516/2017/02/015

Evoli, C., Morlino, G., Blasi, P., & Aloisio, R. 2020b, AMS-02 beryllium data and its implication for cosmic ray transport, Phys. Rev. D, 101, 023013, doi: 10.1103/PhysRevD.101.023013

Farmer, A. J., & Goldreich, P. 2004, Wave Damping by Magnetohydrodynamic Turbulence and Its Effect on Cosmic-Ray Propagation in the Interstellar Medium, ApJ, 604, 671, doi: 10.1086/382040

Fermi, E. 1949, On the Origin of the Cosmic Radiation, Physical Review, 75, 1169, doi: 10.1103/PhysRev.75.1169

Ferrière, K. M. 2001, The interstellar environment of our galaxy, Reviews of Modern Physics, 73, 1031, doi: 10.1103/RevModPhys.73.1031

Fletcher, A., Beck, R., Shukurov, A., Berkhuijsen, E. M., & Horellou, C. 2011, Magnetic fields and spiral arms in the galaxy M51, MNRAS, 412, 2396, doi: 10.1111/j.1365-2966.2010.18065.x

Friedlander, M. 2012, A century of cosmic rays, Nature, 483, 400, doi: 10.1038/483400a

Gabici, S. 2022, Low-energy cosmic rays: regulators of the dense interstellar medium, A&A Rev., 30, 4, doi: 10.1007/s00159-022-00141-2

Girichidis, P., Pfrommer, C., Hanasz, M., & Naab, T. 2020, Spectrally resolved cosmic ray hydrodynamics - I. Spectral scheme, MNRAS, 491, 993, doi: 10.1093/mnras/stz2961

Girichidis, P., Pfrommer, C., Pakmor, R., & Springel, V. 2022, Spectrally resolved cosmic rays – II. Momentum-dependent cosmic ray diffusion drives powerful galactic winds, MNRAS, 510, 3917, doi: 10.1093/mnras/stab3462

Girichidis, P., Werhahn, M., Pfrommer, C., Pakmor, R., & Springel, V. 2024, Spectrally resolved cosmic rays - III. Dynamical impact and properties of the circumgalactic medium, MNRAS, 527, 10897, doi: 10.1093/mnras/stad3628

Gong, M., Ostriker, E. C., & Kim, C.-G. 2018, The X $_{CO}$ Conversion Factor from Galactic Multiphase ISM Simulations, ApJ, 858, 16, doi: 10.3847/1538-4357/aab9af

Gould, R. 1972, Energy loss of a relativistic ion in a plasma, Physica, 58, 379

Govoni, F., & Feretti, L. 2004, Magnetic Fields in Clusters of Galaxies, International Journal of Modern Physics D, 13, 1549, doi: 10.1142/S0218271804005080

Grenier, I. A., Black, J. H., & Strong, A. W. 2015, The Nine Lives of Cosmic Rays in Galaxies, ARA&A, 53, 199, doi: 10.1146/annurev-astro-082214-122457

Han, J. 2017, Observing Interstellar and Intergalactic Magnetic Fields, ARA&A, 55, 111, doi: 10.1146/annurev-astro-091916-055221

Hanasz, M., Strong, A. W., & Girichidis, P. 2021, Simulations of cosmic ray propagation, Living Reviews in Computational Astrophysics, 7, 2, doi: 10.1007/s41115-021-00011-1

Heesen, V., Beck, R., Krause, M., & Dettmar, R.-J. 2009, Cosmic rays and the magnetic field in the nearby starburst galaxy NGC 253: I. The distribution and transport of cosmic rays, A&A, 494, 563, doi: 10.1051/0004-6361:200810543

Heesen, V., De Gasperin, F., Schulz, S., et al. 2023, Diffusion of cosmic-ray electrons in M 51 observed with LOFAR at 54 MHz, A&A, 672, A21, doi: 10.1051/0004-6361/202245223

Heiles, C., & Crutcher, R. 2005, Magnetic Fields in Diffuse HI and Molecular Clouds (Berlin, Heidelberg: Springer Berlin Heidelberg), 137–182, doi: 10.1007/3540313966_7

Hess, V. 2018, On the Observations of the Penetrating Radiation during Seven Balloon Flights, arXiv e-prints, arXiv:1808.02927, doi: 10.48550/arXiv.1808.02927

Hess, V. F. 1912, Über Beobachtungen der durchdringenden Strahlung bei sieben Freiballonfahrten, Z. Phys., 13, 1084

Hopkins, P. F., Butsky, I. S., Panopoulou, G. V., et al. 2022a, First predicted cosmic ray spectra, primary-to-secondary ratios, and ionization rates from MHD galaxy formation simulations, MNRAS, 516, 3470, doi: 10.1093/mnras/stac1791

Hopkins, P. F., Squire, J., Butsky, I. S., & Ji, S. 2022b, Standard self-confinement and extrinsic turbulence models for cosmic ray transport are fundamentally incompatible with observations, MNRAS, 517, 5413, doi: 10.1093/mnras/stac2909

Hopkins, P. F., Chan, T. K., Garrison-Kimmel, S., et al. 2020, But what about...: cosmic rays, magnetic fields, conduction, and viscosity in galaxy formation, MNRAS, 492, 3465, doi: 10.1093/mnras/stz3321

Indriolo, N., Geballe, T. R., Oka, T., & McCall, B. J. 2007, H^+_3 in Diffuse Interstellar Clouds: A Tracer for the Cosmic-Ray Ionization Rate, ApJ, 671, 1736, doi: 10.1086/523036

Jiang, Y.-F., & Oh, S. P. 2018, A New Numerical Scheme for Cosmic-Ray Transport, ApJ, 854, 5, doi: 10.3847/1538-4357/aaa6ce

Kado-Fong, E., Kim, J.-G., Ostriker, E. C., & Kim, C.-G. 2020, Diffuse Ionized Gas in Simulations of Multiphase, Star-forming Galactic Disks, ApJ, 897, 143, doi: 10.3847/1538-4357/ab9abd

Kim, C.-G., Kim, J.-G., Gong, M., & Ostriker, E. C. 2023a, Introducing TIGRESS-NCR. I. Coregulation of the Multiphase Interstellar Medium and Star Formation Rates, ApJ, 946, 3, doi: 10.3847/1538-4357/acbd3a

Kim, C.-G., & Ostriker, E. C. 2017, Three-phase Interstellar Medium in Galaxies Resolving Evolution with Star Formation and Supernova Feedback (TIGRESS): Algorithms, Fiducial Model, and Convergence, ApJ, 846, 133, doi: 10.3847/1538-4357/aa8599

Kim, C.-G., Ostriker, E. C., Somerville, R. S., et al. 2020, First Results from SMAUG: Characterization of Multiphase Galactic Outflows from a Suite of Local Star-forming Galactic Disk Simulations, ApJ, 900, 61, doi: 10.3847/1538-4357/aba962

Kim, C.-G., Ostriker, E. C., Kim, J.-G., et al. 2024, Metallicity Dependence of Pressure-regulated Feedback-modulated Star Formation in the TIGRESS-NCR Simulation Suite, ApJ, 972, 67, doi: 10.3847/1538-4357/ad59ab

Kim, J.-G., Gong, M., Kim, C.-G., & Ostriker, E. C. 2023b, Photochemistry and Heating/Cooling of the Multiphase Interstellar Medium with UV Radiative Transfer for Magnetohydrodynamic Simulations, ApJS, 264, 10, doi: 10.3847/1538-4365/ac9b1d

Kim, W.-T., Kim, C.-G., & Ostriker, E. C. 2020, Local Simulations of Spiral Galaxies with the TIGRESS Framework. I. Star Formation and Arm Spurs/Feathers, ApJ, 898, 35, doi: 10.3847/1538-4357/ab9b87

Kissmann, R. 2014, PICARD: A novel code for the Galactic Cosmic Ray propagation problem, Astroparticle Physics, 55, 37, doi: 10.1016/j.astropartphys.2014.02.002

Krakau, S., & Schlickeiser, R. 2015, PION PRODUCTION MOMENTUM LOSS OF COSMIC RAY HADRONS, ApJ, 802, 114, doi: 10.1088/0004-637X/802/2/114

Krumholz, M. R., Crocker, R. M., & Sampson, M. L. 2022, Cosmic ray interstellar propagation tool using Itô Calculus (CRIPTIC): software for simultaneous calculation of cosmic ray transport and observational signatures, MNRAS, 517, 1355, doi: 10.1093/mnras/stac2712

Kulsrud, R., & Pearce, W. P. 1969, The Effect of Wave-Particle Interactions on the Propagation of Cosmic Rays, ApJ, 156, 445, doi: 10.1086/149981

Kulsrud, R. M. 2005, Plasma Physics for Astrophysics, Princeton Series in Astrophysics (Princeton, N.J.: Princeton University Press)

Leitherer, C., Schaerer, D., Goldader, J. D., et al. 1999, Starburst99: Synthesis Models for Galaxies with Active Star Formation, ApJS, 123, 3, doi: 10.1086/313233

Linzer, N. B., Armillotta, L., Ostriker, E. C., & Quataert, E. 2025, Modeling Cosmic Ray Electron Spectra and Synchrotron Emission in the Multiphase ISM, arXiv e-prints, arXiv:2507.00142, doi: 10.48550/arXiv.2507.00142

Maccione, L., Evoli, C., Gaggero, D., & Grasso, D. 2011, DRAGON: Galactic Cosmic Ray Diffusion Code,, Astrophysics Source Code Library, record ascl:1106.011

Maurin, D., Donato, F., Taillet, R., & Salati, P. 2001, Cosmic rays below z= 30 in a diffusion model: new constraints on propagation parameters, ApJ, 555, 585, doi: 10.1086/321496

McDaniel, A., Jeltema, T., & Profumo, S. 2019, Exploring a cosmic-ray origin of the multiwavelength emission in M31, Phys. Rev. D, 100, 023014, doi: 10.1103/PhysRevD.100.023014

McKinnon, M., Beasley, A., Murphy, E., et al. 2019, in BAAS, Vol. 51, 81

Miniati, F., Jones, T., Kang, H., & Ryu, D. 2001, Cosmic-ray electrons in groups and clusters of galaxies: Primary and secondary populations from a numerical cosmological simulation, ApJ, 562, 233, doi: 10.1086/323434

Mora, S. C., & Krause, M. 2013, Magnetic field structure and halo in NGC 4631, A&A, 560, A42, doi: 10.1051/0004-6361/201321043

Mora-Partiarroyo, S. C., Krause, M., Basu, A., et al. 2019, CHANG-ES: XIV. Cosmic-ray propagation and magnetic field strengths in the radio halo of NGC 4631, A&A, 632, A10, doi: 10.1051/0004-6361/201834571

Moskalenko, I. V., & Strong, A. 1998, Production and propagation of cosmic-ray positrons and electrons, ApJ, 493, 694, doi: 10.1086/305152

Mulcahy, D. D., Fletcher, A., Beck, R., Mitra, D., & Scaife, A. M. M. 2016, Modelling the cosmic ray electron propagation in M 51, A&A, 592, A123, doi: 10.1051/0004-6361/201628446

Mulcahy, D. D., Horneffer, A., Beck, R., et al. 2014, The nature of the low-frequency emission of M 51. First observations of a nearby galaxy with LOFAR, A&A, 568, A74, doi: 10.1051/0004-6361/201424187

Neronov, A., Malyshev, D., & Semikoz, D. V. 2017, Cosmic-ray spectrum in the local Galaxy, A&A, 606, A22, doi: 10.1051/0004-6361/201731149

Ogrodnik, M. A., Hanasz, M., & Wóltański, D. 2021, Implementation of Cosmic Ray Energy Spectrum (CRESP) Algorithm in PIERNIK MHD Code. I. Spectrally Resolved Propagation of Cosmic Ray Electrons on Eulerian Grids, ApJS, 253, 18, doi: 10.3847/1538-4365/abd16f

Orlando, E. 2018, Imprints of cosmic rays in multifrequency observations of the interstellar emission, MNRAS, 475, 2724, doi: 10.1093/mnras/stx3280

Ostriker, E. C., & Kim, C.-G. 2022, Pressure-regulated, Feedback-modulated Star Formation in Disk Galaxies, ApJ, 936, 137, doi: 10.3847/1538-4357/ac7de2

Ostriker, E. C., & Kim, C.-G. 2022, Pressure-regulated, Feedback-modulated Star Formation in Disk Galaxies, ApJ, 936, 137, doi: 10.3847/1538-4357/ac7de2

Padovani, M., Bracco, A., Jelić, V., Galli, D., & Bellomi, E. 2021, Spectral index of synchrotron emission: insights from the diffuse and magnetised interstellar medium, A&A, 651, A116, doi: 10.1051/0004-6361/202140799

Padovani, M., Ivlev, A. V., Galli, D., & Caselli, P. 2018, Cosmic-ray ionisation in circumstellar discs, A&A, 614, A111, doi: 10.1051/0004-6361/201732202

Padovani, M., Ivlev, A. V., Galli, D., et al. 2020, Impact of Low-Energy Cosmic Rays on StarFormation, Space Sci. Rev., 216, 29, doi: 10.1007/s11214-020-00654-1

Pfrommer, C., Pakmor, R., Schaal, K., Simpson, C. M., & Springel, V. 2017, Simulating cosmic ray physics on a moving mesh, MNRAS, 465, 4500, doi: 10.1093/mnras/stw2941

Ponnada, S. B., Panopoulou, G. V., Butsky, I. S., et al. 2024, Synchrotron emission on FIRE: equipartition estimators of magnetic fields in simulated galaxies with spectrally resolved cosmic rays, MNRAS, 527, 11707, doi: 10.1093/mnras/stad3978

Putze, A., Derome, L., & Maurin, D. 2010, A markov chain monte carlo technique to sample transport and source parameters of galactic cosmic rays-ii. results for the diffusion model combining b/c and radioactive nuclei, A&A, 516, A66, doi: 10.1051/0004-6361/201014010

Recchia, S. 2020, Cosmic ray driven galactic winds, International Journal of Modern Physics D, 29, 2030006, doi: 10.1142/S0218271820300062

Redfield, S., & Linsky, J. L. 2004, The Structure of the Local Interstellar Medium. III. Temperature and Turbulence, ApJ, 613, 1004, doi: 10.1086/423311

Robishaw, T., Quataert, E., & Heiles, C. 2008, Extragalactic Zeeman Detections in OH Megamasers, ApJ, 680, 981, doi: 10.1086/588031

Rossi, B. 1964, Cosmic Rays (New York: McGraw-Hill)

Ruszkowski, M., & Pfrommer, C. 2023, Cosmic ray feedback in galaxies and galaxy clusters, A&A Rev., 31, 4, doi: 10.1007/s00159-023-00149-2

Sampson, M. L., Beattie, J. R., Krumholz, M. R., et al. 2023, Turbulent diffusion of streaming cosmic rays in compressible, partially ionized plasma, MNRAS, 519, 1503, doi: 10.1093/mnras/stac3207

Schlickeiser, R. 2002, Cosmic Ray Astrophysics, Astronomy and Astrophysics Library (Berlin, Heidelberg: Springer Berlin Heidelberg), doi: 10.1007/978-3-662-04814-6

Schmidt, P., Krause, M., Heesen, V., et al. 2019, CHANG-ES: XVI. An in-depth view of the cosmic-ray transport in the edge-on spiral galaxies NGC 891 and NGC 4565, A&A, 632, A12, doi: 10.1051/0004-6361/201834995

Seta, A., & Beck, R. 2019, Revisiting the Equipartition Assumption in Star-Forming Galaxies, Galaxies, 7, 45, doi: 10.3390/galaxies7020045

Shu, F. H. 1991, The Physics of Astrophysics Volume I: Radiation (University Science Books)

Sike, B., Thomas, T., Ruszkowski, M., Pfrommer, C., & Weber, M. 2024, Cosmic Ray-Driven Galactic Winds with Resolved ISM and Ion-Neutral Damping, arXiv e-prints, arXiv:2410.06988, doi: 10.48550/arXiv.2410.06988

Soida, M., Krause, M., Dettmar, R.-J., & Urbanik, M. 2011, The large scale magnetic field structure of the spiral galaxy NGC 5775, A&A, 531, A127, doi: 10.1051/0004-6361/200810763

Stein, M., Heesen, V., Dettmar, R.-J., et al. 2023, CHANG-ES: XXVI. Insights into cosmic-ray transport from radio halos in edge-on galaxies, A&A, 670, A158, doi: 10.1051/0004-6361/202243906

Stepanov, R., Shukurov, A., Fletcher, A., et al. 2014, An observational test for correlations between cosmic rays and magnetic fields, MNRAS, 437, 2201, doi: 10.1093/mnras/stt2044

Stone, E. C., Cummings, A. C., Heikkila, B. C., & Lal, N. 2019, Cosmic ray measurements from Voyager 2 as it crossed into interstellar space, Nature Astronomy, 3, 1013, doi: 10.1038/s41550-019-0928-3

Stone, J. M., & Gardiner, T. A. 2010, Implementation of the Shearing Box Approximation in Athena, ApJS, 189, 142, doi: 10.1088/0067-0049/189/1/142

Stone, J. M., Gardiner, T. A., Teuben, P., Hawley, J. F., & Simon, J. B. 2008, Athena: A New Code for Astrophysical MHD, ApJS, 178, 137, doi: 10.1086/588755

Stone, J. M., Tomida, K., White, C. J., & Felker, K. G. 2020, The Athena++ Adaptive Mesh Refinement Framework: Design and Magnetohydrodynamic Solvers, ApJS, 249, 4, doi: 10.3847/1538-4365/ab929b

Strong, A. W., & Moskalenko, I. V. 1998, Propagation of cosmic-ray nucleons in the galaxy, ApJ, 509, 212, doi: 10.1086/306470

Sutherland, R. S., & Dopita, M. A. 1993, Cooling functions for low-density astrophysical plasmas, ApJS, 88, 253, doi: 10.1086/191823

Tabatabaei, F. S., Krause, M., Fletcher, A., & Beck, R. 2008, High-resolution radio continuum survey of M 33: III. Magnetic fields, A&A, 490, 1005, doi: 10.1051/0004-6361:200810590

Thomas, T., Pfrommer, C., & Pakmor, R. 2024, Why are thermally- and cosmic ray-driven galactic winds fundamentally different?, arXiv e-prints, arXiv:2405.13121, doi: 10.48550/arXiv.2405.13121

Torres, D. F. 2004, Theoretical Modeling of the Diffuse Emission of Gamma Rays from Extreme Regions of Star Formation: The Case of ARP 220, ApJ, 617, 966, doi: 10.1086/425415

Vaidya, B., Mignone, A., Bodo, G., Rossi, P., & Massaglia, S. 2018, A particle module for the PLUTO code. II. hybrid framework for modeling nonthermal emission from relativistic magnetized flows, ApJ, 865, 144, doi: 10.3847/1538-4357/aadd17

Wentzel, D. G. 1974, Cosmic-ray propagation in the Galaxy: collective effects., ARA&A, 12, 71, doi: 10.1146/annurev.aa.12.090174.000443

Werhahn, M., Pfrommer, C., & Girichidis, P. 2021a, Cosmic rays and non-thermal emission in simulated galaxies – III. Probing cosmic-ray calorimetry with radio spectra and the FIR–radio correlation, MNRAS, 508, 4072, doi: 10.1093/mnras/stab2535

Werhahn, M., Pfrommer, C., Girichidis, P., Puchwein, E., & Pakmor, R. 2021b, Cosmic rays and non-thermal emission in simulated galaxies - I. Electron and proton spectra compared to Voyager-1 data, MNRAS, 505, 3273, doi: 10.1093/mnras/stab1324

Wiener, J., Zweibel, E. G., & Oh, S. P. 2018, High β effects on cosmic ray streaming in galaxy clusters, MNRAS, 473, 3095, doi: 10.1093/mnras/stx2603

Winner, G., Pfrommer, C., Girichidis, P., & Pakmor, R. 2019, Evolution of cosmic ray electron spectra in magnetohydrodynamical simulations, MNRAS, 488, 2235, doi: 10.1093/mnras/stz1792

Winner, G., Pfrommer, C., Girichidis, P., Werhahn, M., & Pais, M. 2020, Evolution and observational signatures of the cosmic ray electron spectrum in SN 1006, MNRAS, 499, 2785, doi: 10.1093/mnras/staa2989

Yan, H., & Lazarian, A. 2002, Scattering of Cosmic Rays by Magnetohydrodynamic Interstellar Turbulence, Phys. Rev. Lett., 89, 281102, doi: 10.1103/PhysRevLett.89.281102

Yang, H. Y. K., & Ruszkowski, M. 2017, The Spatially Uniform Spectrum of the Fermi Bubbles: The Leptonic Active Galactic Nucleus Jet Scenario, ApJ, 850, 2, doi: 10.3847/1538-4357/aa9434

Zari, E., Frankel, N., & Rix, H.-W. 2023, Did the Milky Way just light up? The recent star formation history of the Galactic disc, A&A, 669, A10, doi: 10.1051/0004-6361/202244194

Zweibel, E. G. 2013, The microphysics and macrophysics of cosmic rays, Physics of Plasmas, 20, 055501, doi: 10.1063/1.4807033

Zweibel, E. G. 2017, The basis for cosmic ray feedback: Written on the wind, Physics of Plasmas, 24, 055402, doi: 10.1063/1.4984017